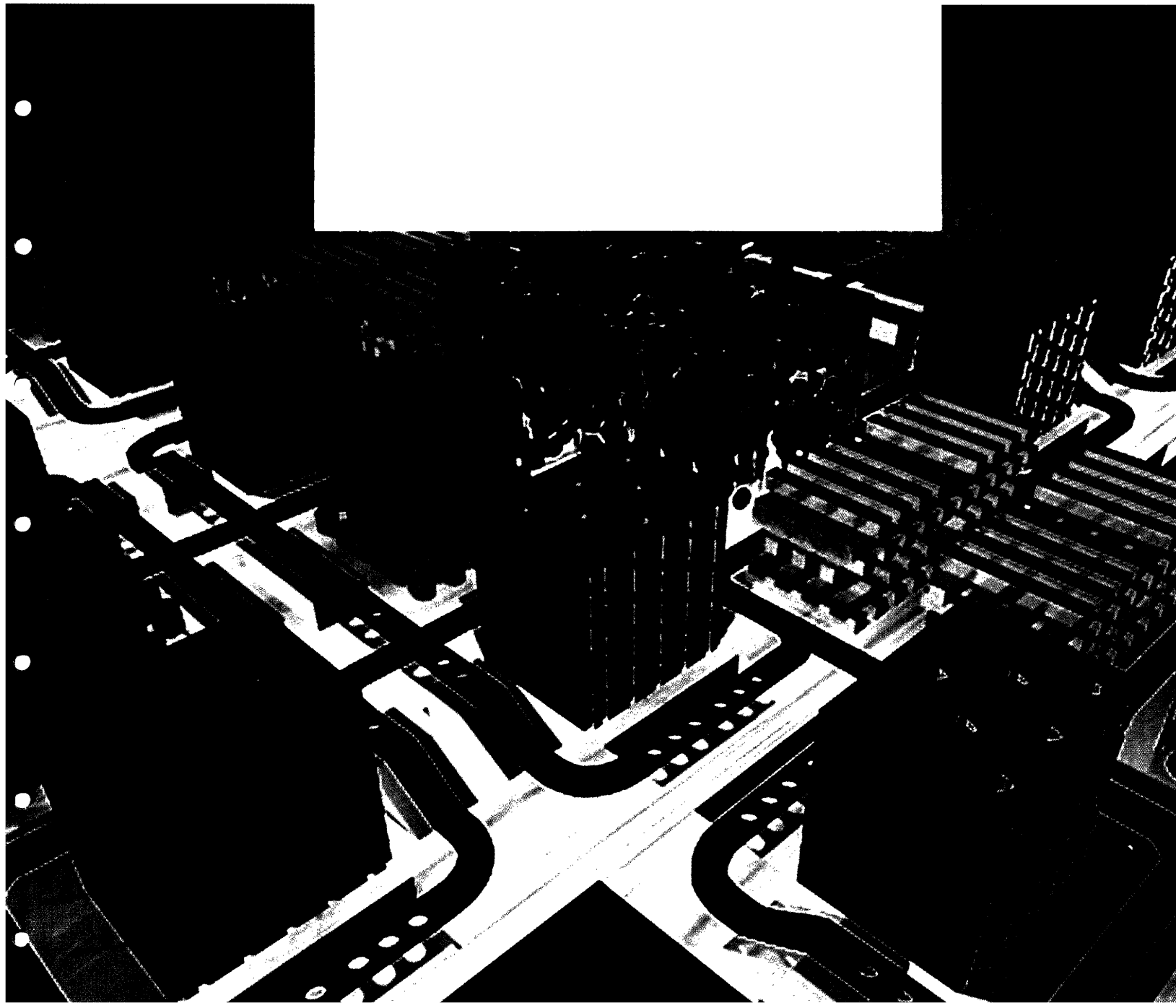


MASSACHUSETTS INSTITUTE OF TECHNOLOGY  
*The* RESEARCH LABORATORY *of* ELECTRONICS



**Analog VLSI Circuits for Inertial Sensory  
Systems**

**By: Maziar Tavakoli Dastjerdi**

**RLE Technical Report No. 651**

**June 2001**

**Analog VLSI Circuits for Inertial Sensory Systems**

**By: Maziar Tavakoli Dastjerdi**

**RLE Technical Report No. 651**

**June 2001**

# Analog VLSI Circuits for Inertial Sensory Systems

by

Maziar Tavakoli Dastjerdi

B.S., Electrical Engineering (1998)  
Sharif University of Technology

Submitted to the Department of Electrical Engineering and Computer  
Science in Partial Fulfillment of the Requirements for the Degree of


Master of Science in Electrical Engineering

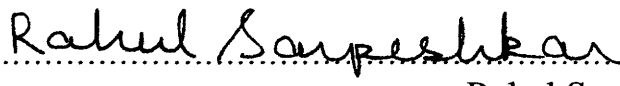
at the

Massachusetts Institute of Technology

June 2001

© 2001 Massachusetts Institute of Technology  
All rights reserved

Signature of Author..........  
Department of Electrical Engineering and Computer Science  
May 10, 2001

Certified by..........  
Rahul Sarpeshkar  
Assistant Professor of Electrical Engineering  
Thesis Supervisor

Accepted by.....  
Arthur C. Smith  
Chairman, Committee on Graduate Students  
Department of Electrical Engineering and Computer Science

# Analog VLSI Circuits for Inertial Sensory Systems

by

Maziar Tavakoli Dastjerdi

Submitted to the Department of Electrical Engineering and Computer Science on May 10, 2001 in Partial Fulfillment of the Requirements for the Degree of Master of Science in Electrical Engineering

## **ABSTRACT**

Vibration sensors are needed in a variety of applications, such as geophysical sensing, machinery vibration and failure prediction, tracking of vehicles, underwater pressure gradient detection, microphones, and in robotic applications. Low noise electronics is critical for creating a high-sensitivity vibration sensor, especially in low proof mass MEMS designs.

We have designed, fabricated, and tested an ultra low noise analog VLSI circuit with feedback adaptation for use as the electronic portion of a MEMS vibration sensor. The electronics performs novel multiplicative feedback offset compensation to improve the performance of demodulator building blocks used in traditional low noise sensing electronics. The design is robust to parasitics and flicker noise. Experimental noise measurements show that the sensing electronics is capable of detecting  $2.5 \times 10^{-3}$  angstrom of displacement, about one order of magnitude more sensitive than electronics in state-of-the-art commercial sensors.

Thesis Supervisor: Rahul Sarpeshkar

Title: Assistant Professor of Electrical Engineering

# TABLE OF CONTENTS

1. INTRODUCTION.....	4
2. VIBRATION SENSOR.....	12
2.1. BASIC FUNCTION.....	12
2.1.1. LOCK-IN TECHNIQUE.....	13
2.1.2. ELECTROSTATIC FORCE-FEEDBACK.....	15
2.2. DEMODULATOR OFFSET COMPENSATION.....	16
2.2.1. SIGNAL AND NOISE ANALYSIS OF THE OFFSET- COMPENSATED DEMODULATOR BLOCK.....	28
2.3. VIBRATION SENSOR PARASITICS INSENSITIVITY.....	36
2.3.1. SIGNAL AND NOISE ANALYSIS OF THE FRONT-END BANDPASS AMPLIFIER.....	38
2.4. SIGNAL AND NOISE ANALYSIS OF THE WHOLE NEWLY DESIGNED VIBRATION SENSOR.....	47
2.5. FABRICATION OF THE VIBRATION SENSOR.....	58
2.6. EXPERIMENTAL RESULTS OF THE VIBRATION SENSOR.....	59
2.6.1. THE OFFSET-COMPENSATED DEMODULATOR.....	59
2.6.2. VIBRATION SENSOR PARASITICS INSENSITIVITY.....	61
2.6.3. VIBRATION SENSOR TOTAL NOISE.....	64
3. REFERENCES.....	67

# 1. INTRODUCTION

For centuries, humans have tried to build machines that mimic the behavior of animals and people. Biological systems have had millions of years to evolve very efficient solutions for problems that they care about in their environment. Their sensory systems often work as well as they possibly can; therefore, they are regarded as a paradigm for efficient computation. They can perform real time complex sensory data processing, in a small volume, and with very low power. For example, the eye can detect a few photons, the ear's detection threshold is near the limit set by thermal noise, cave beetles sense mK changes in temperature, flies perform sophisticated obstacle avoidance and navigation with a few hundred thousand neurons and a few mW of power. However, it is important to notice that instead of doing a blind mimicry, we should take an inspiration from biology that is combined with thought and practicality for it to be of any use. This inspiration must combine a through knowledge of traditional engineering with an insightful understanding of what may be good ideas in biology. Biological computation, in general, is distributed, nonlinear, adaptive, and hybrid (analog and digital). On the other hand, engineering could be even more efficient than biology at certain things, e.g. digital arithmetic. We should also exploit these advantages.

With the advent of cheap and powerful digital computers, the dream of building biologically inspired machines is beginning to turn into reality. However, computers still have great difficulties in making use of the type of visual information that we use every minute of our waking lives with such ease. We can rapidly identify a familiar face, we can navigate on a bike down a narrow garden path and we can hit a tennis ball approaching us at high speeds. One reason for this discrepancy is that extracting information from images is computationally very expensive (a digital rendition of one second long, uncompressed NTSC video amounts to about 22MByte of data). Processing, storing and shipping such vast data streams are what make machine vision difficult.

Another problem is the dearth of sensors and algorithms that make use of multiple, independent pieces of sensory information. Because of the different physical origins of the sensory information and the differing noise properties of visual, auditory or olfactory information, such fusion of information is expected to render any system to be much more robust in a real physical environment.

A perfect example of such a robust system is exhibited in one of the most humble creatures of all, the common house fly. Flies represent an existence proof of a robust, low-resolution (less than 100 by 100 photoreceptors per eye), small, low-power system capable of navigating through unstructured environments during rapid flight. The fly has a brain the size of a grain of rice ( $0.31 \text{ mm}^3$  with about 350,000 neurons in the house fly); however, it performs miraculous real-time optomotor behaviors that machines can't emulate. Flies use two sensory systems to achieve stable and directed flight: the visual system and the halteres. The visual system consists of two compound eyes and also large portions of the fly's brain ( $3/4$  of all neurons in the case of the house fly) are dedicated to processing visual motion information. Motion is computed by correlating the input of one

photoreceptor with the delayed input from a neighboring photoreceptor. It has been shown that fly motion detectors use the phase lag in a first-order lowpass filter to achieve the delay, and use nonlinear multiplication to implement correlation. Motion information is known to underlie many important behaviors in the fly including estimating self-rotation and self-translation, orienting towards small rapidly-moving objects, and estimating time-to-contact for safe landings. Some motion-related tasks like extending the legs for landing can be executed less than 70msec after stimulus presentation. The halteres are knobs suspended at the end of thin stiff stalks located behind the wings. They act as mechanosensors and are capable of detecting small perturbations in the stalk's trajectory caused by forces on the end knob. Signals of the nerves from the halteres system are used to stabilize the body during flight and to stabilize the head during turns. If the halteres are removed from a fly, it spins to the ground, incapable of stable flight. It seems that flies primarily use visual input for stabilization during slow gradual rotations, while halteres input dominates behavior during rapid movements.

Motivated by such instances, research at university laboratories over the last decade has focused on understanding the biological circuits and principles underlying visually-controlled behaviors in some creatures like flies. Fortunately at the same time, silicon circuit fabrication technology has improved dramatically in terms of complexity of circuits that can be fabricated with ease on a single chip.

The fly's visual system provides inspiration for designing artificial visual motion systems. Instead of using high-spatial-resolution CCD cameras from which it is very computationally expensive to extract motion information in real time, we may build a lower-resolution photoreceptor array in which the transduction and processing are integrated to generate the motion information. Functionally, such vision chips can be thought of as combining the functionality of a video camera with that of a digital computer running some dedicated motion-detection algorithm. However, the computational architecture underlying both systems differs radically. Biological systems and biologically inspired systems use massively parallel, analog, non-clocked, collective processing rather than the conventional numerical and symbolic processing paradigms of artificial intelligence and machine vision. In today's almost exclusively all-digital computing environment, the first reflex of a system engineer is to sample and discretize the incoming signal as soon as possible. However, since image brightness is continuous in time and amplitude, it is unnecessary to introduce artifacts by these operations. Rather, it is better to exploit the physics of conductances, capacitances and the nonlinearities inherent in transistors to implement operations that are expensive in the digital domain. Integrating such analog circuits with arrays of photoreceptors can result in silicon vision chips with a performance that would require hundreds of MFLOPS if done on a digital computer, but all within a 1 cm<sup>2</sup> silicon package and often with less than a mW of power.

Expressed in a different manner, image sensors can be classified into two broad categories on the basis of their purpose. Cameras are meant to acquire images for replication at another place or time for the benefit of human observers; visual sensors are meant to extract information about a visual scene for purposes such as robot navigation. In the second category, it is preferable to incorporate visual data processing as early as



possible in the signal flow to reduce the cost of transmitting and processing the tremendous amount of redundant raw image data delivered by an array of photoreceptors. Consistent with this requirement, a number of visual sensing integrated circuits incorporating some amount of processing within each pixel have been described in the literature, many of which are inspired to some degree by biological neural structures. It is clear that good photoreceptors are important components of all these visual sensors.

On the other hand, it is necessary to mention that a drawback of adding substantial local processing into every pixel is that it leads to a steep increase in total silicon area compared to the area devoted to photodetection and hence, a reduction of the total number of pixels that can be integrated on an affordable chip. The resulting loss in spatial sampling rate is a handicap of existing visual sensors, in comparison to traditional approaches of machine vision combining a camera (with a fill factor close to 100%) with external processing hardware. This loss in spatial resolution is not critical for many applications. However at the same time, although increasingly better spatial resolution can be attained with constantly shrinking chip line widths, some other efforts are also being made to enhance this resolution with the help of other methods. We will explain one of them in the following.

A novel principle for the acquisition of visual information is emerging, which extends the effective resolution of a pixel array far beyond the limit imposed by pixel spacing [1]. Instead of measuring the distribution of light intensity at fixed locations, continuous small-amplitude oscillatory movements are applied to the imaging system. As a result of such movements, spatial variations of light intensity in the image turn into temporal fluctuations of light intensity at every photoreceptor. For instance, sweeping a photoreceptor over a thin spatial feature - such as a power cable in an outdoor scene - can produce a detectable impulse of photocurrent even if this feature is much thinner than the pixel spacing. This means that the information capacity of each pixel is improved. The effective spatial resolution of the sensor is then limited by the focusing optics and pixel temporal bandwidth. Knowing the pattern of movements applied to the system, local spatial features can be retrieved from the temporal waveform detected by each photoreceptor. These waveforms can be processed locally in such a way that pixels transmit only higher-level feature information off the chip. Each pixel acts as a high-resolution local feature detector. This is called a vibrating visual sensor. One of its intended applications is robotics navigation.

It is interesting to point out that visual sensors found in some living organisms appear to rely on a related principle. Jumping spiders acquire visual data by sweeping an essentially linear retina back and forth perpendicularly to its larger dimension, while slowly rotating the retina in its own plane. These spiders are capable of complex visual prey/mate discrimination and route finding tasks using two scanning retinas containing only about 800 photoreceptors each. Scanning has been reported in flies as well, which inspired researchers to build a scanning visual sensor for flight control using off-the-shelf components. Humans also rely on tiny periodic vibrations of the retinas to prevent the retinal image from fading.

Let's present a quantitative estimation of the resolution enhancement, provided by vibrations. Let's first consider the case of a 1D image,  $I(x)$ , of an unchanging visual scene focused onto the surface of a visual sensor. If this image is shifting at a velocity  $v$  over the sensor as a consequence of mechanical vibrations occurring at some point in the optical path, a single photoreceptor will detect a light intensity  $I_{pix}(t) = I(x_0 + v \times t)$ , where  $x_0$  depends on the location of the photoreceptor on the sensor. The spatial distribution of light intensity within the image is transformed into a temporal signal. Assuming a constant scanning velocity  $v$ , the spectrum of the temporal signal is related to the spatial spectrum of the image by linear scaling of the frequency axis:

$$f_T = v \cdot f_s \quad (1.1)$$

where  $f_T$  designates temporal frequency and  $f_s$  denotes spatial frequency in the image plane. If the photoreceptor has a temporal bandwidth of  $f_{T \max}$ , the spatial cutoff frequency for a scanning pixel will be  $f_{s \max} = f_{T \max} / v$ . The spatial bandwidth of a non-scanning image sensor is entirely dependent on the spacing  $\Delta x$  of its photoreceptors and equals  $1/(2\Delta x)$ . Therefore, scanning can improve the spatial resolution provided that:

$$\frac{f_{T \max}}{v} > \frac{1}{2\Delta x} \quad (1.2)$$

In the case of a 2D image subject to mechanical vibrations along both axes, each photoreceptor acquires visual information along a curvilinear path determined by image movements. Continuous image data is collected along the scanning path with a resolution determined by the same analysis as in the 1D case. The areas of the image inside the circular paths are not scanned. An image feature such as a line segment can be detected if it is long enough to cross the scanning path of at least one photoreceptor, even if it is much thinner than pixel spacing. It has been described in [1] that even if the visual scene and its illumination conditions do not remain constant, this method is still effective.

To quantitatively sense the resolution enhancement obtained in a typical vibrating visual sensor, assume that the scanning frequency is 100Hz with a photoreceptor bandwidth of 1kHz. Photoreceptor spacing is  $70 \mu m$ , and the scanning path is circular with a diameter equal to pixel spacing. Using these parameters, it can be shown that the effective spatial resolution ( $2\Delta x$ ) in the image plane along the scanning path is  $22 \mu m$ . Consequently, the effective resolution has been improved by a factor of almost 6.

Hardware implementation of a vibrating visual sensor requires building a mechanical and optical device to shift an image along some scanning path, while keeping it in focus. There are two different constructions to solve this problem. The first way to induce the mechanical vibrations consists of spinning a tilted mirror in front of the focusing lens (see figure 1.1(a)) to provide periodic constant-velocity scanning along a circular path, which produces periodic intensity fluctuations. This method is called circular scanning. The mirror must be mounted on the axis of a motor, which should be tilted at an angle of

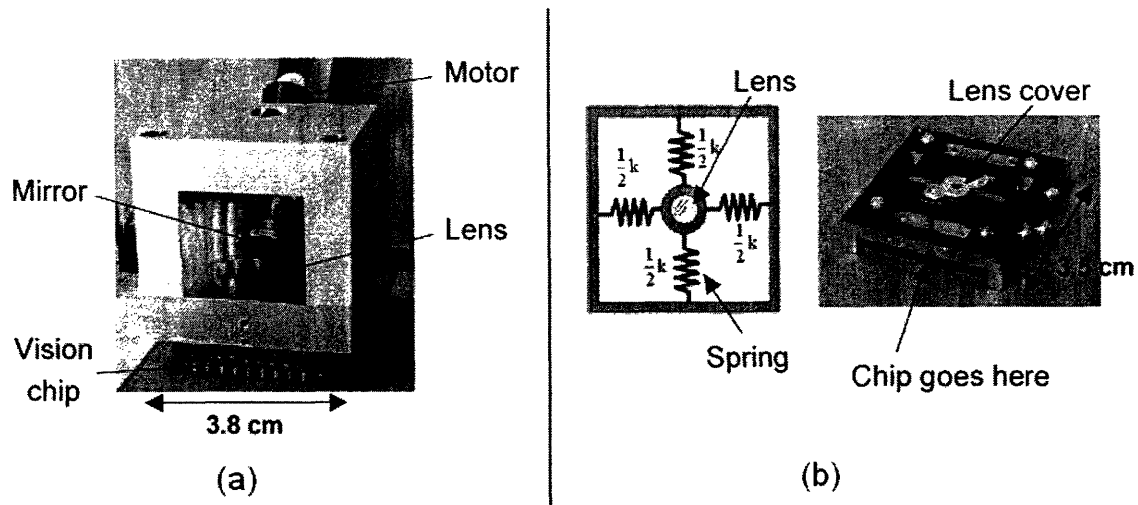


**Figure 1.1: (a) Photograph of mechanical device producing circular scanning, (b) drawing and photograph of mechanical device producing scanning powered by environmental vibrations amplified near a chosen resonant frequency (random scanning).**

about  $45^\circ$  with respect to the optical axis of the lens. If the mirror is not exactly perpendicular to the motor axis but tilted by a small angle  $\varepsilon$ , rotation of the motor will cause the reflective surface to wobble, thereby causing the image to travel a circular path with a radius of  $2\varepsilon$  in viewing angle. The spinning mirror device is easy to build and provides accurate control over the scanning path. Therefore, it is most appropriate for laboratory experiments. For practical applications where space and power consumption are an issue, the solution is to capture inherently available vibrations of the environment. In this case, an alternative device has been designed where an irregular scanning pattern is caused by displacements of the lens. In this device, the lens is mounted on springs (see figure 1.1(b)) allowing lateral X-Y displacements, but maintaining constant spacing between the lens and the chip. If the system is mounted onto a vibrating platform such as a vehicle driving on a rough surface, the mechanical energy available in the vicinity of the resonance frequency of the lens/spring system will cause scanning movements. To be effective, the amplitude of these movements must be on the order of pixel spacing on the chip, e.g. a few tens of microns. The shape of the scanning path will depend on the relative magnitudes and phases of vibrations applied to the X and the Y axes, and on the resonance frequency matching between the axes. This scheme is named random scanning. As the scanning path will vary over time depending on the naturally-occurring environmental vibratory conditions, extra sensors are necessary to monitor the position of the lens and then, we use this information in the interpretation of the output generated by the visual sensing chip. This is the point where the need for inertial and vibration sensors arises. They serve to detect the scanning path. Output of a single pixel can be combined with signals from these inertial sensors to identify and localize local image features.

A vibration sensor can be thought of as a very high-sensitivity accelerometer with a very low noise floor over a required bandwidth. In addition to the above-mentioned specific application in a vibrating visual sensor, the need exists for high-sensitivity low-noise vibration sensors for various other applications, such as geophysical sensing, machinery

vibration and failure prediction, tracking and identification of vehicles or personnel, intrusion detectors, and underwater pressure gradient detection.

Integrated circuits play an important role in the process of gathering and processing information. In many more traditional cases, however, the actual sensing element is not part of the integrated circuit, but fabricated in a different technology using substantially different tools and materials. As a result, the cost of sensors often exceeds that of the information processing, and determines other important parameters such as physical size, packaging, reliability, or power consumption. In contrast, these days there exist the more recent micromachined sensors. These kinds of sensors can offer size and weight advantages over traditional ones.

There are two different types of micromachining: bulk and surface. Bulk micromachining is generally more expensive than surface micromachining. Surface micromachining has enabled the cofabrication of thin-film micromechanical structures and CMOS integrated circuits. Over the past 15 years, it has become established as a versatile solution for a wide variety of sensing problems, especially for inertial sensing ones. Only a few additional processing steps compatible with standard fabrication techniques and materials are required to cofabricate mechanical sensing elements and the associated electronic interface circuits. Mechanical structures fabricated in surface micromachining technologies consist of deposited thin-film of polysilicon, aluminum, silicon nitride, and other materials. The negligible fatigue and lack of memory of polysilicon make it the material of choice for the fabrication of high-performance micromechanical sensors. The minimum role of electronics in such sensors is the signal detection and conditioning, and noise reduction. By bringing the sense element onto the integrated circuit, surface micromachining leverages the experience and sophisticated processes of IC manufacturing and brings about all the customary advantages of IC solutions: batch fabrication, high yield, small size, low power, low cost, and improved functionality and reliability.

Generally, for sensing physical quantities such as acceleration, vibration, angular rate, or pressure, a mechanical sense element converts the unknown quantity into a displacement that is then detected and converted to an electrical signal. This displacement can be measured by several means, such as tunneling, piezo-resistive, optical, and capacitive. Tunneling sensors have a low noise floor, but due to the small allowable displacement at the tip, they require a very stiff feedback loop, which reduces the useful bandwidth and dynamic range. Piezo-resistive strain gauges are used widely in sensors because of the simple interfacing to off-chip electronic circuits. Position sensors that measure the capacitance between a conducting polysilicon proof mass and a fixed electrode, on the other hand, require no additional processing, can be extremely low noise and sensitive, and compatible with CMOS electronics, as we said before. Their dual function as a displacement sensor and an electrostatic actuator, and also their negligible temperature coefficient are other important advantages of the capacitive sensor readout. Considering the small sense capacitances in this method (a few hundreds of femtofarads typically), the low parasitics that are characteristics of monolithic integration are the key to maximize the performance in this technique.

This thesis concentrates on a present-day capacitive vibration sensor, and the various improvements we have incorporated into its design to enhance its performance. The basic function and the block configuration of a current vibration sensor, along with a couple of schemes employed in its design (such as lock-in technique, electrostatic force-feedback, and adaptation) will be all explained and illustrated in the next chapter. Then one at a time, we will introduce our own new (mostly electronic) modifications designed to ameliorate the vibrating sensing function. We will demonstrate the obtained improvement associated with each modification with the help of careful analysis, simulation, and experiment.

Briefly, these improved features include:

- Automatic Offset Compensation: As we will show in the next chapter, demodulator is a major building block of the vibration sensor. Device mismatches or different input DC levels to this block may produce DC offset in it. Since the demodulator is an inherently balanced circuit, this offset can degrade its performance. Although it is possible to nullify this offset by manual adjustment, it is best to develop a mechanism to make this offset compensation automatic. Therefore, we will add an offset compensator to implement a multiplicative nonlinear feedback pathway to automatically cancel this offset. To be more specific, in the presence of an offset in the demodulator, the resulting high frequency signal at the demodulator's output will be sensed by the offset compensator, demodulated back to baseband by this compensator, low-pass filtered to extract the offset information, and fed back to demodulator's negative input to slowly adapt and nullify this offset. This results in robust operation, reduces flicker noise, improves sensitivity, and obviates the need for frequent manual adjustment of the drifting offset.
- Insensitivity to Parasitics: As we previously pointed out, since the vibration sensing capacitances are small and comparable to typical parasitics in the sensor, one of the important drawbacks of the current scheme is the attenuation of the signal level at the sensor output in the presence of parasitics on this sensitive node. In order for our circuit to be inherently insensitive to parasitics that may exist between the sensor output (sense node) and substrate, a bandpass amplifier will be placed in our new design to perform the first stage of our signal conditioning. This amplifier will be used in a closed-loop configuration with a designed high loop gain. Thus, the inherent properties of feedback will ensure that even the presence of large parasitics will not degrade the performance much.
- Ultra-Low-Noise Design: The most important characteristic of a vibration sensor is its sensitivity, which is evaluated by its minimum detectable displacement. This requires that the sensor have a very low noise floor. Thus, the circuit implementations will be carefully designed based on this fact, a thorough noise analysis of the whole sensor will be executed, and schemes to further lower the noise level will be discussed.

The outline of this thesis is as follows: In section 2.1, we will explain the basic function and configuration of a present-day capacitive vibration sensor, along with the schemes employed in its design. In section 2.2, we will discuss how to develop an offset compensator to automatically nullify the offset of our demodulator. Then, the signal and noise analysis of the whole offset-compensated demodulator will be carried out. Section 2.3 concentrates on the design and analysis of the first stage (front-end) bandpass amplifier, which will give our sensor immunity against parasitics. Then in section 2.4, we will consider the entire new vibration sensor and analyze its signal and noise performance as a whole. After that, the minimum detectable displacement of the whole vibration sensor will be obtained. Section 2.5 will show how we VLSI fabricated our designed vibration sensor. Finally in section 2.6, we will present the various experimental results we obtained from our fabricated vibration sensor.

## 2. VIBRATION SENSOR

As previously mentioned, a vibration sensor is essential in a variety of applications, such as implementation of a vibrating visual sensor where it yields important inertial information for sensing self-motion. The output of a single pixel can be combined with signals from this sensor to identify and localize image features. The basic function of a vibration sensor, as its name implies, is to sense vibrations and transduce them to electrical signals. Naturally, the primary goal of such a circuit should be sensing as small mechanical vibrations as possible.

### 2.1 BASIC FUNCTION

Figure 2.1 shows the basic core of a differential capacitive vibration sensor. It consists of two capacitors labeled  $C_{s1}$  and  $C_{s2}$ , which are the vibration sensing capacitances. They are matched to be as near to each other in value as possible. The capacitors share a moving middle plate that forms the sense node and have one separate static plate each.  $C_p$  is the parasitic capacitance that may exist between the sense node and substrate on a chip. When there is no vibration, the moving plate is exactly in the middle, so  $C_{s1}$  and  $C_{s2}$  are exactly equal and the voltage signal at the sense node ( $V_x$ ) is zero. However, when vibrations are present they perturb the middle plate and cause mismatch between the two capacitors. These oscillations in plate position produce fluctuations in the voltage signal at the sense node.

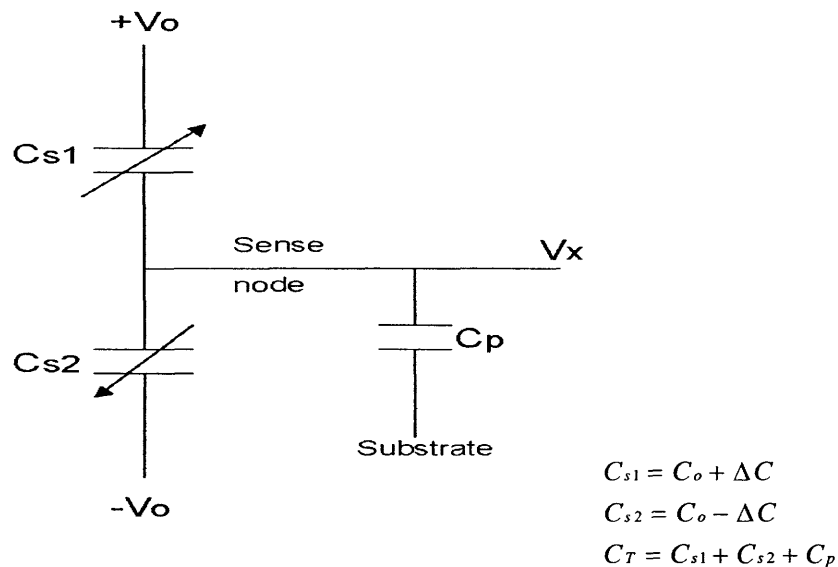


Figure 2.1: Basic core of a differential capacitive vibration sensor

The signal of interest to us is  $V_x$ , which is calculated below:

$$\Rightarrow V_x = V_o \frac{C_{s1}}{C_{s1} + C_{s2} + C_p} - V_o \frac{C_{s2}}{C_{s1} + C_{s2} + C_p} = V_o \frac{C_{s1} - C_{s2}}{C_{s1} + C_{s2} + C_p} = V_o \frac{2\Delta C}{C_T} \quad (2.1)$$

Assuming for the moment that parasitic capacitance ( $C_p$ ) is zero:

$$C_p = 0 \Rightarrow C_T = 2C_o \Rightarrow V_x = V_o \frac{\Delta C}{C_o} \quad (2.2)$$

Now let's derive  $\Delta C$  in terms of the displacement,  $\Delta x$ , of the middle moving plate:

$$C|_{x=x_o} = C_o = \frac{\epsilon_0 A}{x_o}, \quad x_o : \text{Equilibrium capacitor plate distance of } C_{s1} \text{ and } C_{s2}$$

$$C = \frac{\epsilon_0 A}{x} \Rightarrow \frac{\partial C}{\partial x} \Big|_{x=x_o} = -\frac{\epsilon_0 A}{x_o^2} = -\frac{C_o}{x_o}$$

$$\Rightarrow C_{s1} = \frac{\epsilon_0 A}{x_o - \Delta x} \approx C_o - \left( \frac{\partial C}{\partial x} \Big|_{x=x_o} \right) \times \Delta x = C_o + \frac{C_o}{x_o} \Delta x \Rightarrow \Delta C = \frac{C_o}{x_o} \Delta x \quad (2.3)$$

$$(2.2), (2.3) \Rightarrow V_x = V_o \frac{\Delta x}{x_o} \Rightarrow \frac{V_x}{V_o} = \frac{\Delta x}{x_o}$$

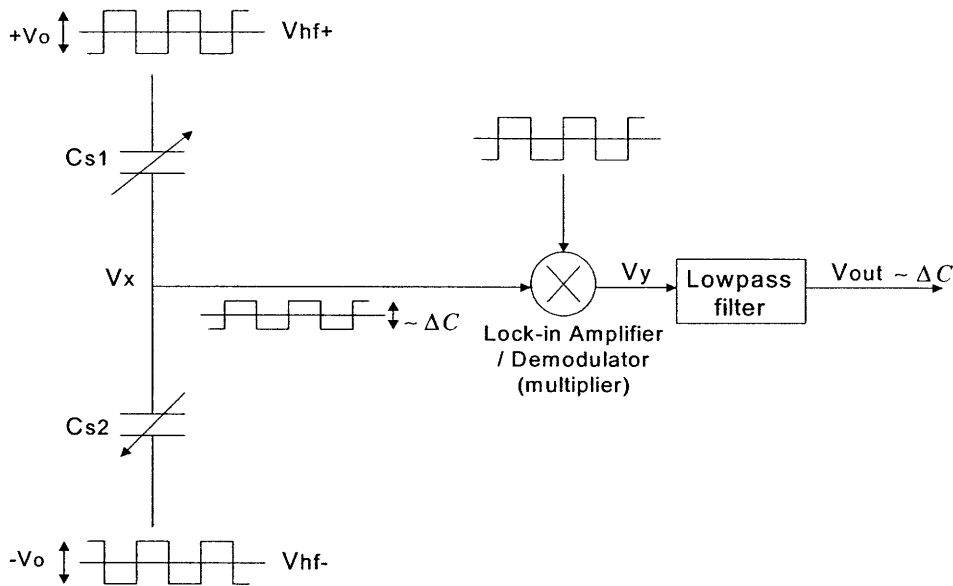
### 2.1.1 LOCK-IN TECHNIQUE

The signal level of the sensor's output in figure 2.1 is relatively low. As an example, a representative set of specifications from a modern vibration sensor is:  $V_o = 1V$ ,  $x_o = 1\mu m$ , and  $\Delta x = 0.01A^\circ$ . Then, the above equation suggests that  $V_x = 1\mu V$ .

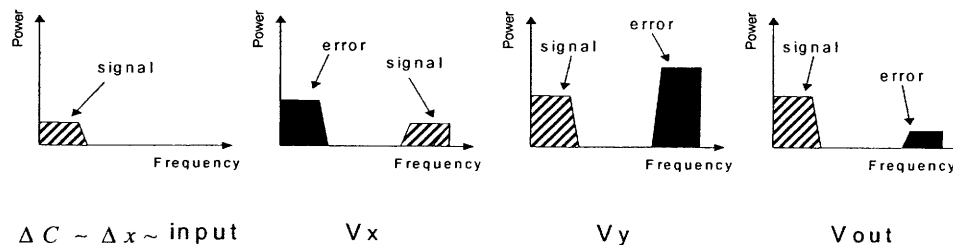
Because of the faint signal levels, sensing is accomplished using a "lock-in technique" (also known as "chopper stabilization"). It is used to attenuate the low-frequency errors and noise. The most important of these unwanted signals is the flicker noise. Moreover, since the sensor output often goes to an amplifier for further signal conditioning, this amplifier's offset and drift can also add some errors. The other sources of errors might be substrate coupling and electromagnetic interface (EMI). The effect of all the above-mentioned errors can be severely attenuated by employing the lock-in technique.

Figure 2.2 depicts the key steps in the lock-in technique. Notice that  $V_o$  is not a constant DC voltage anymore. Instead, we use two antiphase ac carrier modulation signals. Their waveform can be either square-wave or sinusoidal. The modulation frequency is typically between 100kHz to 5MHz. Now, when the input vibration moves the middle plate, we have small fluctuations in the voltage signal at the sense node. In fact, the fluctuations in capacitance simply modulate the carrier signal (like an AM modulation). Thus, the baseband signal spectrum is moved up to around carrier frequency and the spectrums of the signal and low-frequency errors are separated. Figure 2.3 shows the frequency domain interpretation of this technique. As we can see,  $V_x$  consists of a signal component





**Figure 2.2: Lock-in technique employed to sense faint signal levels of sensor output**



**Figure 2.3: Frequency domain interpretation of the lock-in technique**

at high (carrier) frequency and an error component at low frequency. This signal then undergoes a demodulation process. Specifically, it is passed through a lock-in amplifier/demodulator, which is basically a multiplier. It is multiplied by a replica of the carrier signal (except with different amplitude). This process interchanges the location of signal and error spectrums in frequency domain, so now we have a low-frequency signal component and a high frequency error component (see  $V_y$  in figure 2.3). Furthermore, because the demodulator block has usually some gain, both the signal level and error level increase proportionally. The signal of interest is then extracted by lowpass filtering the demodulator's output. This preserves the signal, while the errors and noise are filtered out (See  $V_{out}$  in figure 2.3). Comparing the output signal spectrum with the input signal spectrum in figure 2.3 reveals that we have amplified our baseband signal of interest,

while at the same time all the low-frequency errors and noise have been almost eliminated. Considering the relatively large levels of these errors compared to our vibration signal, in the absence of this technique our signal would have been lost.

### 2.1.2 ELECTROSTATIC FORCE-FEEDBACK

In figure 2.1, we assumed that  $C_{s1}$  and  $C_{s2}$  are perfectly matched. If they are not, an undesirable component will be added to our signal. Let's recalculate  $V_x$  from equation (2.1):

$$\begin{aligned} C_{s1} &= C_{o1} + \Delta C \\ C_{s2} &= C_{o2} - \Delta C \quad , \quad C_{o1} \neq C_{o2} \\ C_T &= C_{s1} + C_{s2} + C_p \end{aligned}$$

$$(2.1) \Rightarrow V_x = V_o \frac{C_{s1} - C_{s2}}{C_{s1} + C_{s2} + C_p} = V_o \frac{2\Delta C}{C_T} + V_o \frac{C_{o1} - C_{o2}}{C_T} \quad (2.4)$$

The first term in equation (2.4) is our signal of interest, while the second term is unwanted. This portion simply adds to our signal. It has the same frequency content as the signal; therefore, it can't be eliminated by using the lock-in technique described above. Expressed in another way, the large gains necessary for amplification of tiny signals also amplify the DC offset due to mismatch of the two vibration sensing capacitors and saturate the circuit. The solution to this problem is to employ "electrostatic force-feedback". An OTA-C (Ordinary Transconductance Amplifier Capacitor) filter senses the circuit's output voltage ( $V_{out}$  in figure 2.2), lowpass filters the demodulated output, and applies a feedback voltage to  $C_{s2}$  that alters its distance from the substrate through the action of an electrostatic force. The electrostatic force-feedback thus adapts  $C_{s2}$  to match  $C_{s1}$  at very low frequencies and attenuates the unwanted DC offset and other low-frequency signals.

The employment of electrostatic force-feedback becomes more evident if we look at figure 2.4, showing the complete block diagram of a present-day vibration sensor. Because the diagram illustrates all the concepts introduced so far in this chapter, we will briefly go through all of its different parts again. The two vibration sensing capacitors, as we said, are  $C_{s1}$  and  $C_{s2}$ . They are capacitively fed with two antiphase ac carrier modulation signals. The coupling capacitors from the signal sources are large enough to be regarded as shorts at the carrier frequency. The demodulation and amplification process is usually performed via a Gilbert multiplier circuit with output load capacitors performing the desired lowpass filtering. The Gilbert multiplier is marked  $\times$  in figure 2.4. The reference input, which multiplies the signal, is a replica of the carrier signal.

The compensating force-feedback OTA-C filter is also clearly seen in the figure. Note that the low-frequency feedback signal is resistively coupled to  $C_{s2}$  while the high-frequency ac carrier signal is capacitively coupled to  $C_{s2}$  such that the two signals do not interfere with each other. Trimming of the  $C_{s1}$  equilibrium gap distance is accomplished

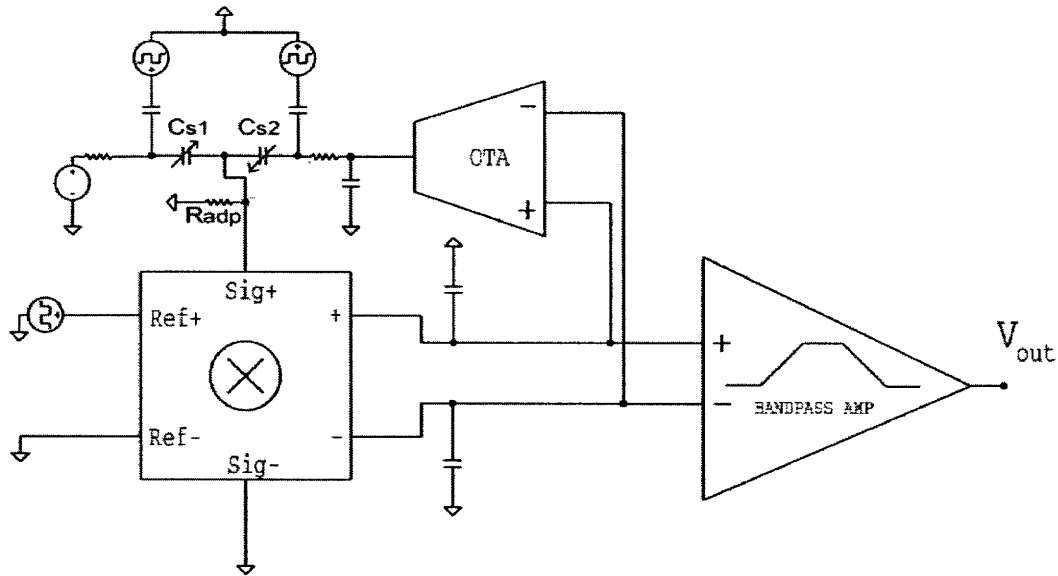


Figure 2.4: Complete block diagram of a present-day capacitive vibration sensor

by connecting its static plate to a resistively coupled DC voltage source that can alter the electrostatic force between the static substrate plate and the moving plate. The flexibility of being able to trim the  $Cs_1$  gap ensures that we are near the perfectly matched condition even without adaptation. The adaptation then serves to attenuate any residual offsets.  $R_{adp}$  in figure 2.4 establishes a DC path from our floating sense node to ground. It is usually implemented by an adaptive element, i.e. a PMOS transistor with its body terminal connected to source and its gate terminal connected to drain. It is basically composed of back-to-back diodes and exhibits an I-V characteristic that is sinh-like. Under DC operation (or under large-signal operation) it may be assumed to be on, while it is off under small-signal ac operation. The last block in figure 2.4 is the bandpass amplifier used as the back end of the circuit. Its pass-band is coincident with the vibration sensing range of interest. It provides more amplification for input vibration signals in the pass-band, and further attenuates any undesirable noise and out-of-band signals.

## 2.2 DEMODULATOR OFFSET COMPENSATION

As we mentioned above, a Gilbert multiplier cell is often used as the demodulator. This cell is a well-known circuit and has been widely used in different applications. It is the basis for most integrated circuit balanced multiplier systems. Thus, it will only be briefly discussed here. Figure 2.5 shows the circuit of a Gilbert multiplier cell. It performs a four-quadrant analog multiplication. It consists of the series connection of an emitter-coupled pair ( $Q_1$ - $Q_2$ ) with two cross-coupled, emitter-coupled pairs ( $Q_3$ - $Q_6$ ). Neglecting base currents and the output resistances of the transistors and the biasing current source, it can be shown ([9]) that:

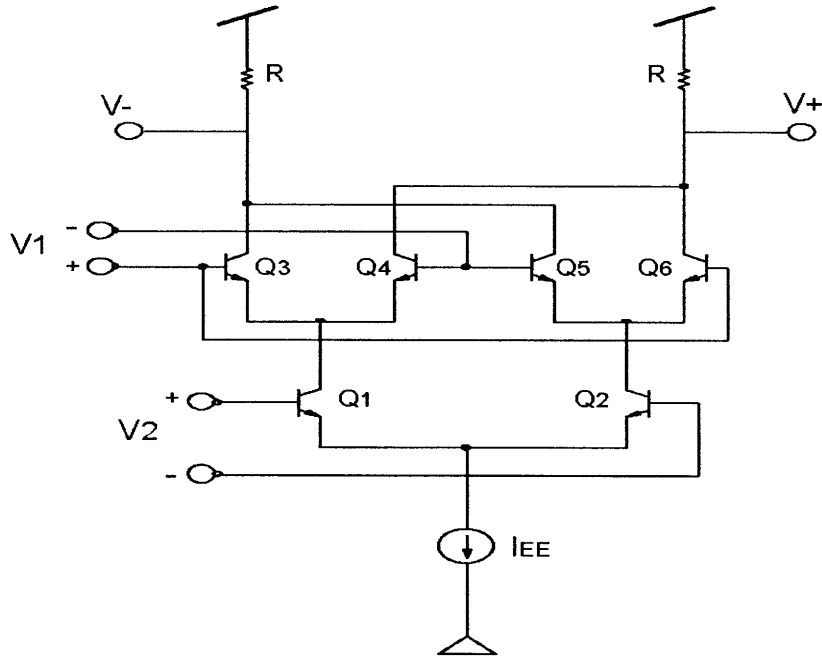


Figure 2.5: Gilbert multiplier cell

$$V_{out} = (V_+) - (V_-) = RI_{EE} \left( \tanh \left( \frac{V_1}{2V_{TH}} \right) \right) \left( \tanh \left( \frac{V_2}{2V_{TH}} \right) \right) \quad (2.5)$$

The hyperbolic-tangent function may be represented by the infinite series:

$$\tanh x = x - \frac{x^3}{3} \dots$$

Assuming that  $x$  is much less than one, the hyperbolic-tangent can then be approximated by:

$$\tanh x \approx x$$

Applying this relation to equation (2.5), we have:

$$V_{out} \approx RI_{EE} \left( \frac{V_1}{2V_{TH}} \right) \left( \frac{V_2}{2V_{TH}} \right) \quad V_1, V_2 \ll V_{TH} \quad (2.6)$$

Thus, for small-amplitude signals, the circuit performs an analog multiplication.

Although most Gilbert multiplier cells depend on the exponential transfer function of bipolar transistors (like the one in figure 2.5), sometimes MOS transistors are also used in the circuit. We will employ one of these multipliers in our sensor in later stages. Hence, it is appropriate to introduce an instance of these kinds of multipliers here. Figure 2.6 shows a MOS-bipolar version of the Gilbert multiplier. The bottom emitter-coupled pair (Q<sub>1</sub>-Q<sub>2</sub>) is implemented by bipolar transistors, while the two cross-coupled, source-

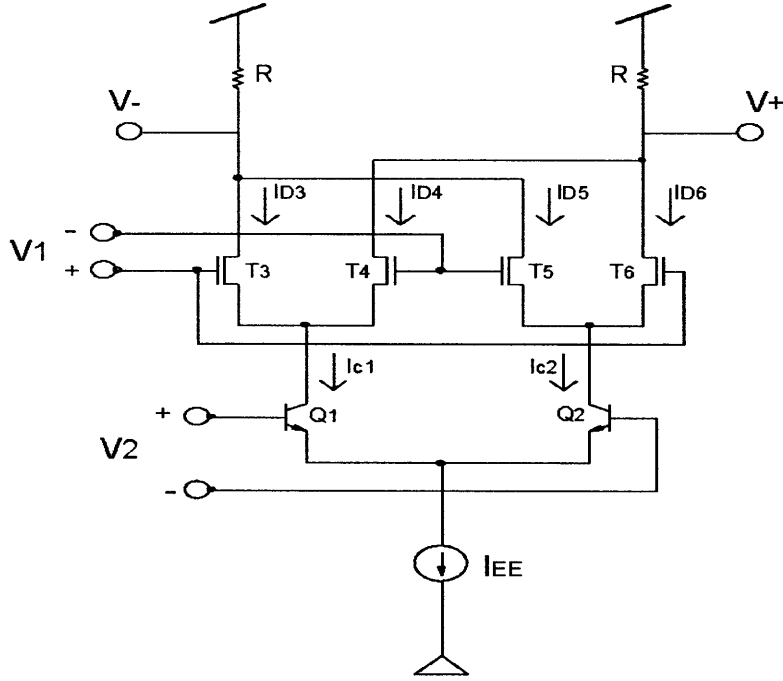


Figure 2.6: A MOS-bipolar version of the Gilbert multiplier cell

coupled pairs (T<sub>3</sub>-T<sub>6</sub>) use NMOS transistors. As the analysis of such a circuit has been rarely done in the literature, a detailed analysis will follow.

If  $V_{c1}$  denotes the voltage of the collector node of Q<sub>1</sub> and  $V_T$  is the threshold voltage of the NMOS transistors while  $V_{TH}$  is the thermal voltage, we can write:

$$I_{D3} + I_{D4} = I_{c1}, \quad K_n = \frac{1}{2} \mu_n C_{ox} \frac{W}{L}$$

$$I_{D3} = K_n (V_{GS3} - V_T)^2 = K_n (V_{1+} - V_{c1} - V_T)^2 \quad (2.7)$$

$$I_{D4} = K_n (V_{GS4} - V_T)^2 = K_n (V_{1-} - V_{c1} - V_T)^2 \Rightarrow \sqrt{\frac{I_{D4}}{K_n}} = V_{1-} - V_{c1} - V_T \Rightarrow V_{c1} + V_T = V_{1-} - \sqrt{\frac{I_{D4}}{K_n}}$$

$$(2.7) \Rightarrow I_{D3} = K_n \left( V_{1+} - V_{1-} + \sqrt{\frac{I_{D4}}{K_n}} \right)^2 = K_n \left( V_1 + \sqrt{\frac{I_{D4}}{K_n}} \right)^2 = K_n \left( V_1^2 + \frac{I_{D4}}{K_n} + 2V_1 \sqrt{\frac{I_{D4}}{K_n}} \right)$$

$$\Rightarrow I_{c1} - I_{D4} = K_n V_1^2 + I_{D4} + 2V_1 \sqrt{K_n I_{D4}} \Rightarrow 2I_{D4} + 2V_1 \sqrt{K_n I_{D4}} + K_n V_1^2 - I_{c1} = 0$$

$$\frac{\sqrt{I_{D4}} = y}{\rightarrow y^2 + V_1 \sqrt{K_n} y + \frac{K_n V_1^2 - I_{c1}}{2} = 0} \Rightarrow y = \frac{-V_1 \sqrt{K_n} + \sqrt{2I_{c1} - K_n V_1^2}}{2}$$

$$I_{D4} = y^2 = \frac{1}{4} \left( K_n V_1^2 + 2I_{c1} - K_n V_1^2 - 2V_1 \sqrt{K_n} \sqrt{2I_{c1} - K_n V_1^2} \right) = \frac{I_{c1}}{2} - \frac{V_1}{2} \sqrt{K_n} \sqrt{2I_{c1} - K_n V_1^2}$$

$$\Rightarrow I_{D3} = I_{c1} - I_{D4} = \frac{I_{c1}}{2} + \frac{V_1}{2} \sqrt{K_n} \sqrt{2I_{c1} - K_n V_1^2}$$

Assuming that  $V_1$  is small:

$$I_{D4} \approx \frac{I_{c1}}{2} - \frac{V_1}{2} \sqrt{2K_n I_{c1}} \quad , \quad I_{D3} \approx \frac{I_{c1}}{2} + \frac{V_1}{2} \sqrt{2K_n I_{c1}}$$

Similarly, we have:

$$I_{D5} \approx \frac{I_{c2}}{2} - \frac{V_1}{2} \sqrt{2K_n I_{c2}} \quad , \quad I_{D6} \approx \frac{I_{c2}}{2} + \frac{V_1}{2} \sqrt{2K_n I_{c2}}$$

$$\Rightarrow V_{out} = (V_+) - (V_-) = R \left[ (I_{D3} + I_{D5}) - (I_{D4} + I_{D6}) \right] = R V_1 \sqrt{2K_n} \left( \sqrt{I_{c1}} - \sqrt{I_{c2}} \right) \quad (2.8)$$

The output current relationship of the bottom bipolar emitter-coupled pair ( $Q_1$ - $Q_2$ ) in figure 2.6 has been already derived in [9]:

$$I_{c1} = \frac{I_{EE}}{1 + \exp\left(-\frac{V_2}{V_{TH}}\right)} \quad , \quad I_{c2} = \frac{I_{EE}}{1 + \exp\left(\frac{V_2}{V_{TH}}\right)}$$

Assuming that  $V_2$  is also small, let's make a couple of approximations:

$$\text{For } x \ll 1: \exp(x) \approx 1+x \Rightarrow \frac{1}{1+\exp(x)} \approx \frac{1}{2+x} = \frac{1}{2} \times \frac{1}{1+\frac{x}{2}} \approx \frac{1}{2} \left(1 - \frac{x}{2}\right) = \frac{1}{2} - \frac{x}{4} \Rightarrow I_{c2} = \frac{I_{EE}}{2} - I_{EE} \frac{V_2}{4V_{TH}}$$

$$\text{And: } \exp(-x) \approx 1-x \Rightarrow \frac{1}{1+\exp(-x)} \approx \frac{1}{2-x} = \frac{1}{2} \times \frac{1}{1-\frac{x}{2}} \approx \frac{1}{2} \left(1 + \frac{x}{2}\right) = \frac{1}{2} + \frac{x}{4} \Rightarrow I_{c1} = \frac{I_{EE}}{2} + I_{EE} \frac{V_2}{4V_{TH}}$$

On the other hand, if  $x \ll 1$ :  $\sqrt{1+x} \approx 1 + \frac{x}{2}$  ,  $\sqrt{1-x} \approx 1 - \frac{x}{2}$  .

$$(2.8) \Rightarrow V_{out} = R V_1 \sqrt{2K_n} \left( \sqrt{I_{c1}} - \sqrt{I_{c2}} \right) \approx R V_1 \sqrt{2K_n} \sqrt{\frac{I_{EE}}{2}} \left[ \sqrt{1 + \frac{V_2}{2V_{TH}}} - \sqrt{1 - \frac{V_2}{2V_{TH}}} \right] \approx$$

$$R V_1 \sqrt{K_n I_{EE}} \left[ \left(1 + \frac{V_2}{4V_{TH}}\right) - \left(1 - \frac{V_2}{4V_{TH}}\right) \right] \Rightarrow V_{out} \approx R \frac{\sqrt{K_n I_{EE}}}{2V_{TH}} V_1 V_2 \quad V_2 \ll V_{TH} \quad (2.9)$$

Consequently, for small-amplitude signals, this MOS-bipolar version of Gilbert cell also performs the required multiplication.

Now let's return to the block diagram of the vibration sensor (figure 2.4). The demodulator is the most important electronic block. It is used as the front end of the entire electronic circuit here.

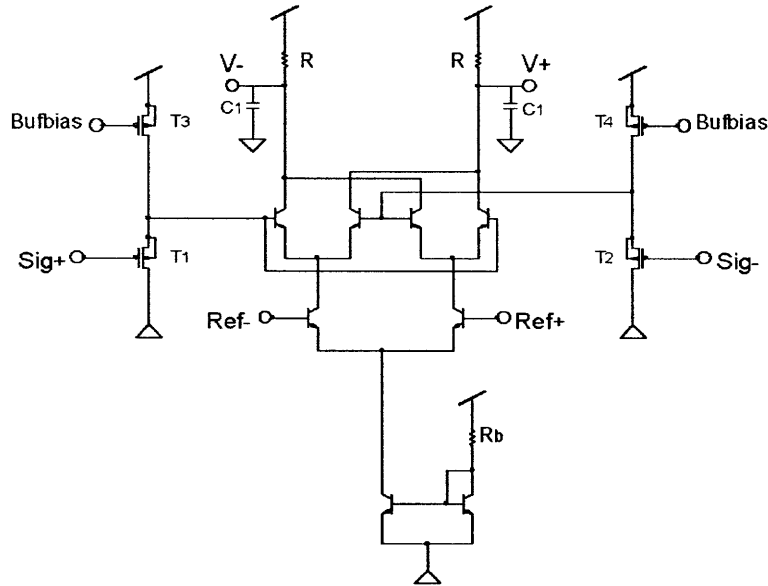


Figure 2.7: Transistor level implementation of the demodulator (multiplier) block used in figure 2.4

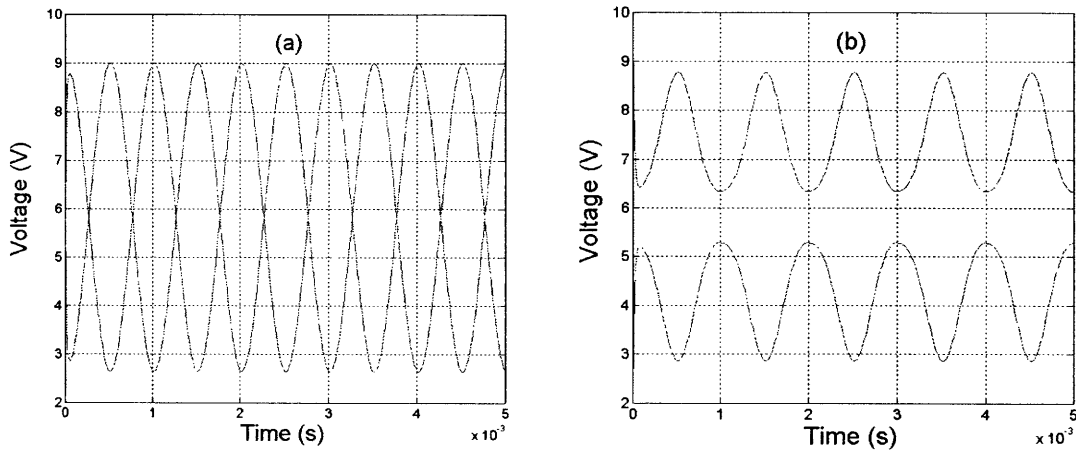


Figure 2.8: Output signal waveforms of the demodulator in figure 2.7, responding to sinusoidal input signals when (a) there is no input DC offset, (b) the Sig and Ref inputs have +100mV and -50mV DC offset, respectively.

Figure 2.7 shows the transistor level circuit of the demodulator block, which is usually employed in the vibration sensor of figure 2.4. Its basic core is a Gilbert multiplier cell, introduced earlier in figure 2.5.  $T_1$  and  $T_2$  serve as the input buffers for the Sig input, while  $T_3$  and  $T_4$  are their bias current sources, respectively. Comparing figure 2.7 with figure 2.5 reveals that the Sig and Ref inputs in figure 2.7 are the same as the  $V_1$  and  $V_2$  inputs in figure 2.5. The simple current mirror at the bottom of figure 2.7 along with the biasing resistor ( $R_b$ ) serves as our current source. The two output capacitances ( $C_1$ ) perform the required lowpass filtering (refer to figure 2.4).

Gilbert multiplier is an inherently balanced circuit, meaning its performance is optimized when there is no DC offset in the circuit. This offset may be produced if the two

multiplier inputs have DC offsets or when device mismatches exist in the cell. The drawback of the offset is that it can make the inputs larger than  $V_{TH}$ , so the approximation  $\tanh x \approx x$  no longer holds; the linear approximation is not valid anymore. For large  $x$ ,  $\tanh x$  is always smaller than  $x$ , thus the effective gain of the circuit is decreased and the non-linearity of the multiplier output is increased. These concepts become more evident by looking at figure 2.8. It shows the SPICE simulated output behavior of the multiplier in figure 2.7. We use a test 501kHz sinusoidal signal as the Sig input and a 500kHz sinusoidal signal as the Ref input, expecting to get a 501-500=1kHz sinusoid at the output. Applying these test inputs, the outputs of the circuit of figure 2.7 ( $V_+$  and  $V_-$ ) when there's no offset in the cell are shown in figure 2.8(a). We can see that the signals are large and complementary differentially encoded versions of each other with the same DC level. Figure 2.8(b) shows the same simulated output signals with intentionally produced offset in the circuit. To be more specific, the Sig and Ref inputs have now +100mV and -50mV DC offset, respectively. It is easy to observe that the DC level of the outputs are now different, the peak-to-peak signal amplitudes have decreased (the signal gain has dropped by more than 50%), and the outputs seem not to be perfect sinusoids any longer. Some non-linearity can be observed.

The noise behavior of the Gilbert multiplier also degrades in the presence of offset. This is important for us, because the total noise level of the whole sensor determines the minimum vibration we can detect; in other words sensitivity is reduced when there is offset in the demodulator. We will talk about this subject in more detail later. Finally, remember that (see figure 2.4) the outputs of the demodulator go to the inputs of the force-feedback OTA and the back-end bandpass amplifier. These blocks often utilize a differential pair as their input stage. Hence, to show their best performance, it is required that the DC levels of their inputs be relatively close to each other. This won't be satisfied if we have offset in the output of the demodulator block.

Considering all the above reasons, our first improvement to the vibration sensor of figure 2.4 will be to provide a mechanism to compensate and cancel the offset of the demodulator block. One non-clever fix is to connect a variable DC voltage source to the Sig. node (see figure 2.4) and manually adjust it to nullify the offset. However, to obviate the need for frequent manual adjustment of the drifting offset, it is best to make this offset compensation automatic.

The first automatic offset compensating solution that comes to mind is to take advantage of the properties of negative feedback. Specifically, we can put an amplifier that senses the demodulator outputs (i.e.  $V_+$  and  $V_-$  in figure 2.7), extracts their DC mismatch (by performing a very slow lowpass filtering), and then apply the amplifier's output as the negative feedback signal to the Sig. node. The idea is to monitor the demodulator outputs, extract their DC level difference as an error, and nullify that by using feedback. Figure 2.9 shows the circuit used to implement this idea. Comparing to figure 2.7, the only new part is the offset-compensating OTA. This OTA is basically composed of an input PMOS differential pair with a current source on top, along with a couple of cascode current mirrors to increase the OTA gain. The reason to use a PMOS input stage is to increase the slew-rate and also lower the flicker noise, which will turn out to be the dominant noise



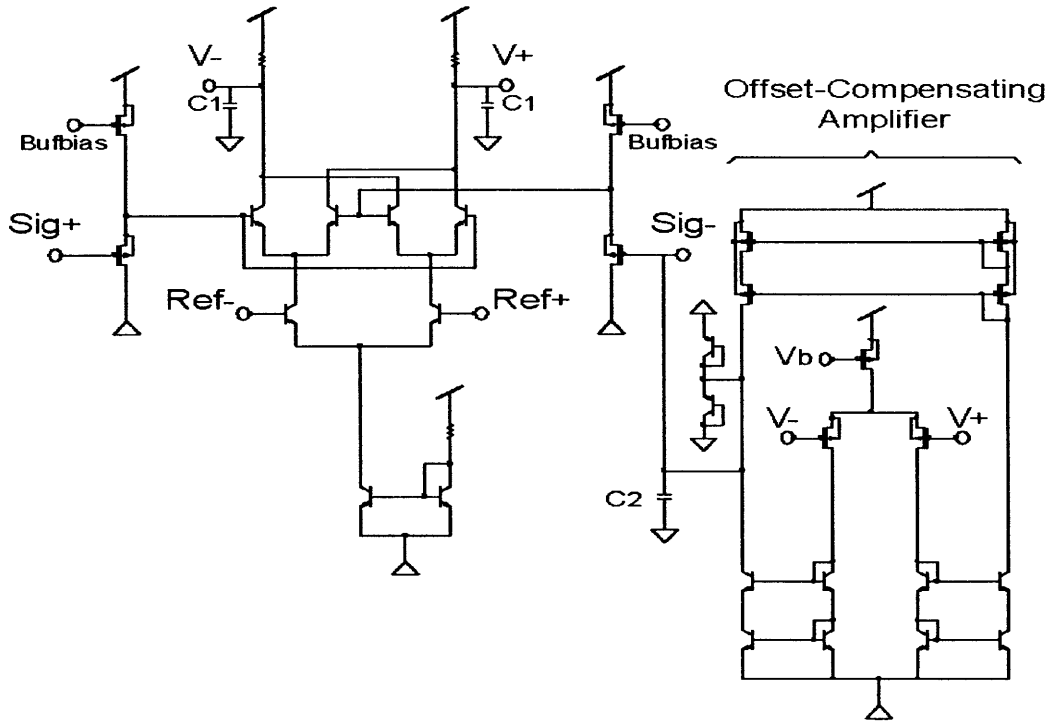


Figure 2.9: Transistor level circuit of the improved demodulator with the offset-compensating amplifier

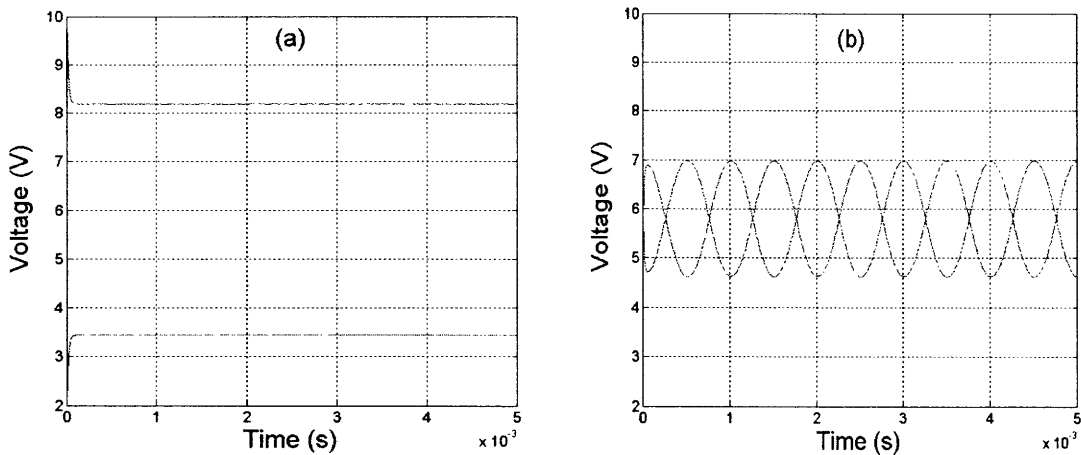


Figure 2.10: Output signal waveforms of the demodulator in figure 2.9, responding to sinusoidal input signals when (a) the Sig and Ref inputs have +100mV and -50mV DC offset, respectively, (b) the Sig and Ref inputs have both +100mV DC offset.

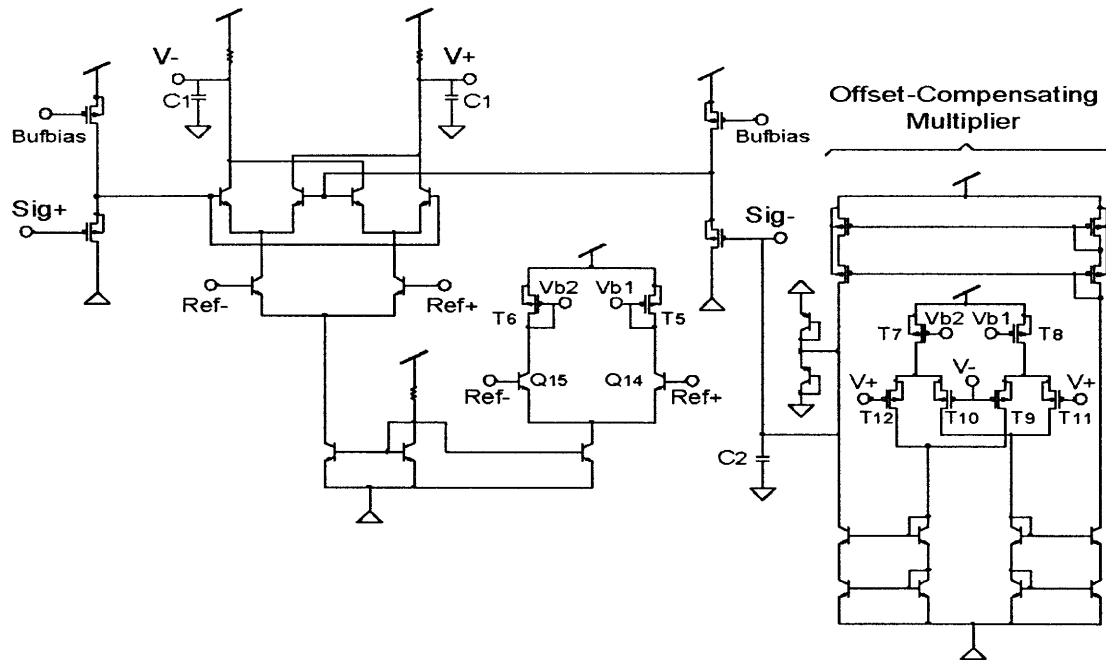
source here. Because  $V_+$  and  $V_-$  are usually biased somewhere halfway between the rails, the use of PMOS does not pose any problem regarding the input range of the offset-compensating amplifier.  $C_2$  is a relatively large capacitor, performing the required slow lowpass filtering to extract the DC information. A pair of back-to-back diodes has been also used at the OTA output node to clamp the feedback signal and limit its excursion.

Figure 2.10(a) shows the output response of the compensated demodulator of figure 2.9 to sinusoidal input signals (with the same characteristics as the test inputs of the circuit of figure 2.7). The DC offset of the Sig and Ref inputs are the same +100mV and -50mV, respectively. Unfortunately, we see that the outputs still have different DC levels despite having the offset compensator in the circuit; and of more concern, the signal gain seems to have become zero!

The reason for such a behavior originates from the fact that we are dealing with a non-linear feedback loop. In other words, the demodulator (that is basically a multiplier) is a non-linear element. Thus, although the feedback loop is designed to have a negative sign, as soon as the second multiplying input (the Ref input) goes negative, the sign flips and the overall feedback loop becomes positive, causing the circuit outputs to blow up! This is the reason for the waveform behavior of figure 2.10(a). To test this hypothesis, we make the DC offset of the Ref input so large that it always possesses a positive value (e.g. if the sinusoid amplitude is 100mV, we also make the DC offset 100mV). We expect to see a normal multiplying behavior from the demodulator, as the feedback loop sign should remain negative at all times. This is observed in figure 2.10(b). The outputs have again the same DC level, and the signal gain has been restored. However, the problem is that as we mentioned in order for our offset compensating feedback loop to operate correctly, we need to intentionally introduce a large offset into our Ref input. We have eliminated the offset in the demodulator output by introducing an offset at the input! Thus, we need to improve our circuit further to get rid of this added offset.

The above discussion ignites another idea: let's not fix the gain sign of our offset-compensating amplifier. Let's sense the sign of our Ref input: if it is positive, we keep the amplifier's sign intact, and if it is negative, we flip the sign of the amplifier so that the loop's sign always remains negative. Exploring the idea further, we discover that we basically need a second multiplication. We can effectively sense the demodulator outputs, multiply them by our Ref input, amplify and lowpass filter the result, and feed it back to the Sig. node of the demodulator. In other words, we have multiplied by our Ref input twice in the loop, so its sign does not matter and the feedback loop remains negative at all times, regardless of the Ref input. Figure 2.11 shows such a circuit. The offset-compensating amplifier of figure 2.9 has now been reconfigured to form a multiplier. Paying more attention to this section shows that we are basically using a folded MOS-bipolar version of the Gilbert multiplier cell, very much alike the one in figure 2.6:  $Q_{14}$  and  $Q_{15}$  in figure 2.11 are the same as  $Q_1$  and  $Q_2$  in figure 2.6,  $T_9$ - $T_{12}$  in figure 2.11 are the four MOS transistors playing the role of  $T_3$ - $T_6$  in figure 2.6, except that here these transistors are PMOS for the reasons expressed previously (one may seek the reason of not using PNP bipolar transistors here instead of PMOS's: PNP's are usually unavailable in most of the ordinary fabrication processes).  $T_5$ ,  $T_8$  and also  $T_6$ ,  $T_7$  are two simple current mirrors to direct (and also lower the level of) the necessary current of the offset-compensating multiplier. The two multiplying signal here are the Ref input and the demodulator outputs ( $V_+$ - $V_-$ ).

Figure 2.12(a) shows the output response of the demodulator of figure 2.11 to sinusoidal input signals (with the same characteristics as used previously). The DC offset of the Sig



**Figure 2.11: Transistor level circuit of the improved demodulator with the offset-compensating multiplier**

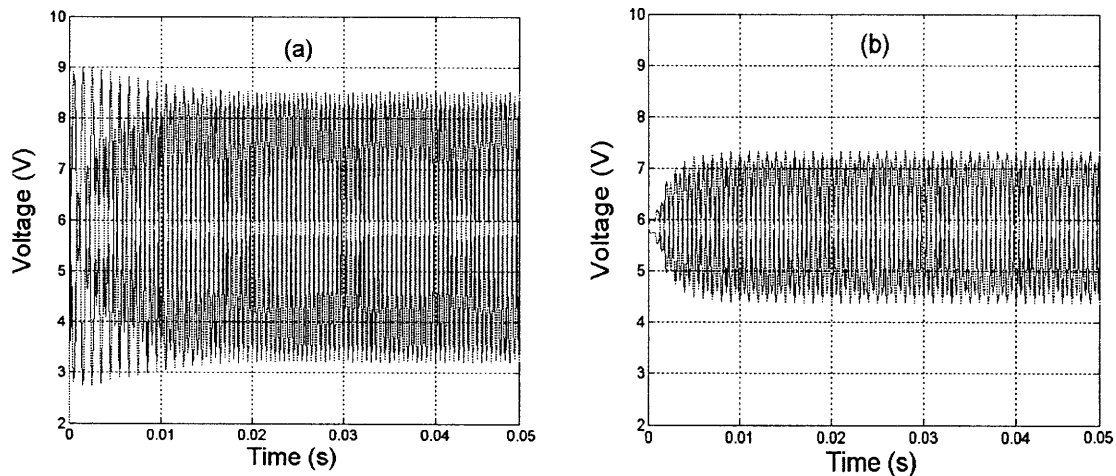


**Figure 2.12: Output signal waveforms of the demodulator in figure 2.11, responding to sinusoidal input signals when (a) the Sig and Ref inputs have +100mV and -50mV DC offset, respectively, (b) the Sig and Ref inputs have -50mV and 0 DC offset, respectively.**

and Ref inputs are still the same +100mV and -50mV, respectively. We see that the outputs ( $V_+$  and  $V_-$ ) approach each other until they reach the same DC level. This implies that the feedback signal (Sig-) slowly approaches the DC offset value of Sig+ (100mV here) to nullify the offset. Hence, even though Ref alternatively becomes both positive and negative, the feedback loop seems to function properly.

However, there still remains a slight problem. To understand it, let's mathematically analyze the loop. Assume that:

$$\text{Ref} = (\text{Ref}_+) - (\text{Ref}_-) = A \sin(\omega_{ref})t + V_{osref}$$

$$\text{Sig}_+ = B \sin(\omega_{ref} + \Delta\omega)t + V_{ossig}$$

We know that demodulator output is the product of Sig and Ref:

$$\begin{aligned} V_{out} = (V_+) - (V_-) = A v_1 \left[ \frac{1}{2} AB \cos(\Delta\omega)t - \frac{1}{2} AB \cos(2\omega_{ref} + \Delta\omega)t + BV_{osref} \sin(\omega_{ref} + \Delta\omega)t + \right. \\ \left. AV_{ossig} \sin(\omega_{ref})t + V_{osref}V_{ossig} \right] \quad (2.10) \end{aligned}$$

$V_{out}$  is lowpass filtered and then multiplied by Ref again to yield the offset-compensating multiplier output (refer to figure 2.11):

$$\begin{aligned} \text{Lowpassed, } V_{out} = (V_+) - (V_-) = A v_1 \left[ \frac{1}{2} AB \cos(\Delta\omega)t + V_{osref}V_{ossig} \right] \\ \text{Sig}_- = A v_2 A v_1 \left[ \frac{1}{4} A^2 B \sin(\omega_{ref} + \Delta\omega)t + \frac{1}{4} A^2 B \sin(\omega_{ref} - \Delta\omega)t + \frac{1}{2} ABV_{osref} \cos(\Delta\omega)t + \right. \\ \left. AV_{osref}V_{ossig} \sin(\omega_{ref})t + V_{osref}^2 V_{ossig} \right] \end{aligned}$$

The ultimate feedback signal is the lowpass filtered version of Sig<sub>-</sub>:

$$\text{Sig}_- = A v_2 A v_1 \left[ \frac{1}{2} ABV_{osref} \cos(\Delta\omega)t + V_{osref}^2 V_{ossig} \right] \quad (2.11)$$

If we have absolutely no offset in our Ref input (i.e.  $V_{osref} = 0$ ), the feedback signal in equation (2.11) will become zero. It will have no information about the DC offset of the Sig input whatsoever, that we are trying to compensate. The offset information is lost! Thus, in this case despite the fact that the demodulator output might contain no DC offset (because one of the two multiplying inputs (i.e. the Ref input) has no DC content), the problem is that the feedback signal (i.e. Sig<sub>-</sub>) does not follow Sig<sub>+</sub> and the feedback is basically not functioning. Actually the feedback loop is dead! Figure 2.12(b) shows the response of the demodulator of figure 2.11 to sinusoidal input signals. The Ref input has no DC offset at all, while the Sig input has -50mV of offset. The output waveforms may seem to be almost as expected, but observing the feedback signal (not shown in this figure) reveals that it is not trying to follow and lock on the input signal. We need to modify the circuit so that even with  $V_{osref} = 0$ , the feedback loop is still active.

To solve this problem, let's not lowpass filter the demodulator output. Then, the offset-compensating multiplier effectively multiplies this unfiltered  $V_{out}$  (the one in equation (2.10)) by Ref. The ultimate feedback signal is then the lowpass filtered version of the result, as before. Calculating the new resulting feedback signal, we get:

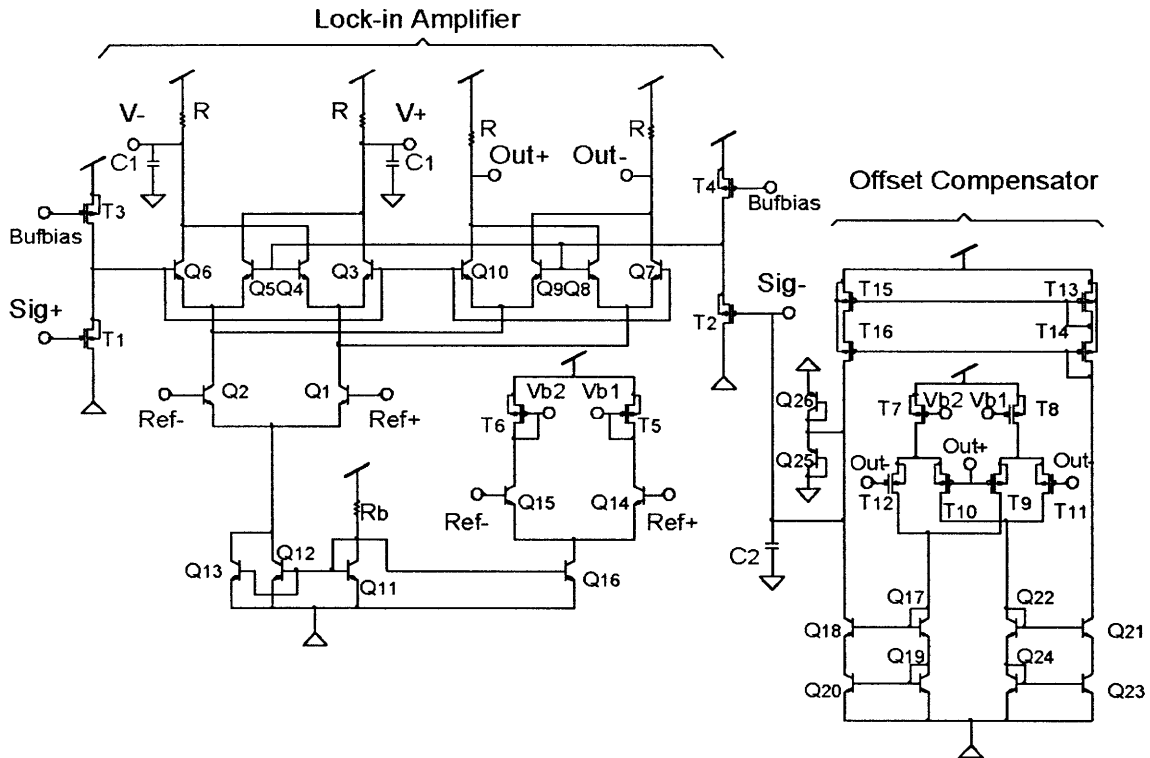
$$\text{Sig} = A_{V2}A_{V1}[ABV_{osref} \cos(\Delta\omega)t + V_{osref}^2V_{ossig} + \frac{1}{2}A^2V_{ossig}] \quad (2.12)$$

Here, even if  $V_{osref} = 0$ , the last term remains non-zero and the offset information is preserved. The feedback signal will have the necessary information about the input offset ( $V_{ossig}$ ), so the loop will be able to compensate for it even when  $V_{osref} = 0$ .

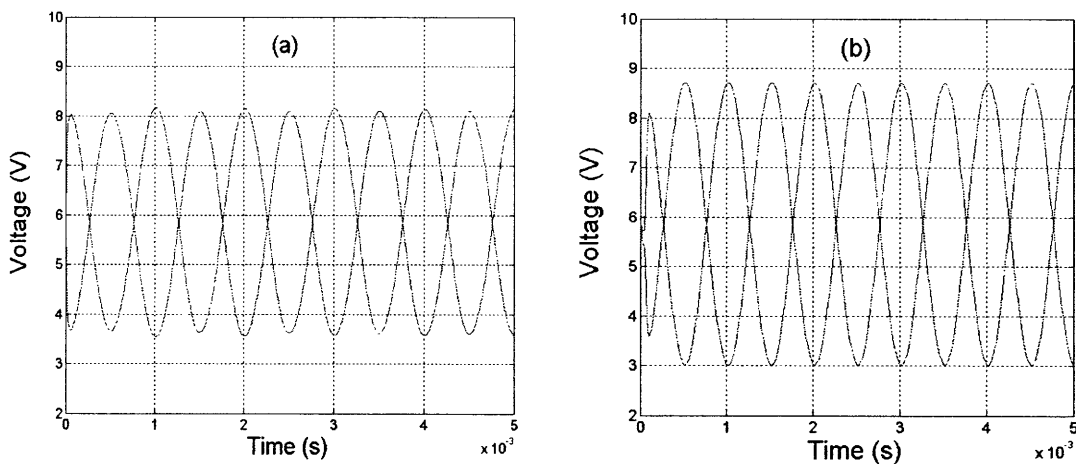
The preceding discussion suggests that we use a non-filtered version of demodulator output as part of our offset-compensating feedback loop. However, note that this output is also the ultimate output of the entire demodulator block. Moreover, it goes to some other succeeding blocks in the circuit like the force-feedback OTA and the back-end bandpass amplifier. Consequently, we definitely need to filter this output to eliminate noise and all the unwanted high-frequency components. The solution to this discrepancy is to use two forward-path Gilbert multipliers in parallel: the output of one of those is not filtered and is used in the offset-compensating feedback loop, while the output of the other one is lowpass filtered and forms the ultimate output of the demodulator block, going to the succeeding blocks.

Figure 2.13 shows the transistor level implementation of the final offset-compensated demodulator. Comparing with figure 2.11, we see that there are two Gilbert multiplier cells in parallel. They share the bottom emitter-coupled pair ( $Q_1$  and  $Q_2$ ). The output of the cell consisting of  $Q_1$ - $Q_6$  (i.e.  $V_+$  and  $V_-$ ) is lowpass filtered by  $C_1$  and forms the ultimate output of the demodulator block. The output of the cell consisting of  $Q_1$ ,  $Q_2$ , and  $Q_7$ - $Q_{10}$  (i.e.  $\text{Out}_+$  and  $\text{Out}_-$ ) is not lowpass filtered and goes to the offset compensator as part of the feedback loop, so here the offset compensator effectively multiplies  $\text{Out}_+$ - $\text{Out}_-$  by the Ref input. We will refer to these two parallel multiplier cells as the “Lock-in Amplifier”. Note that because now we have two multipliers, we have doubled the bias current by requiring two bias transistors ( $Q_{12}$  and  $Q_{13}$ ) instead of just one transistor.

Figure 2.14 shows the output responses of the offset-compensated demodulator of figure 2.13 to sinusoidal input signals. Again we use a test 501kHz sinusoidal signal as  $\text{Sig}_+$  and a 500kHz sinusoidal signal as Ref, resulting in a 501-500=1kHz sinusoid at the output. In figure 2.14(a), the DC offset of the Sig and Ref inputs are the same +100mV and -50mV, respectively. We see that the outputs ( $V_+$  and  $V_-$ ) have the same DC levels, the signal gain is relatively large, and the waveforms pretty much have the form of sinusoids; i.e. the non-linearity is negligible. This shows that the feedback loop functions properly even when the inputs become alternatively positive and negative. Figure 2.14(b) shows the same output response, except that here the DC offset of Sig and Ref are -50mV and 0, respectively. The waveforms again have the same DC level, as expected. Not shown in this figure, the feedback signal (Sig.) follows and locks on the DC offset of  $\text{Sig}_+$  (-50mV here) to nullify both the demodulator input and output offset, meaning the offset-compensating feedback loop is in effect even when  $V_{osref} = 0$ . Another way to observe this fact is to compare figure 2.14(b) with figure 2.12(b) (note that the horizontal scales are not the same). The signal gain has more than doubled here with the same conditions. The reason is, that the loop has compensated for the offset of the Sig input here, while in figure 2.12(b) the existence of input offset degraded the small-signal gain.



**Figure 2.13: Transistor level circuit of the final offset-compensated demodulator: consisting of Lock-in Amplifier and Offset Compensator blocks**



**Figure 2.14: Output signal waveforms of the final offset-compensated demodulator in figure 2.13, responding to sinusoidal input signals when (a) the Sig and Ref inputs have +100mV and -50mV DC offset, respectively, (b) the Sig and Ref inputs have -50mV and 0 DC offset, respectively.**

In summary, we have solved all the problems we faced in the previous demodulators regarding their offset compensation. The demodulator in figure 2.13 finally possesses the required input and output offset compensation property. It can nullify and cancel the DC offset in the entire demodulator block, regardless of their originating source (except for

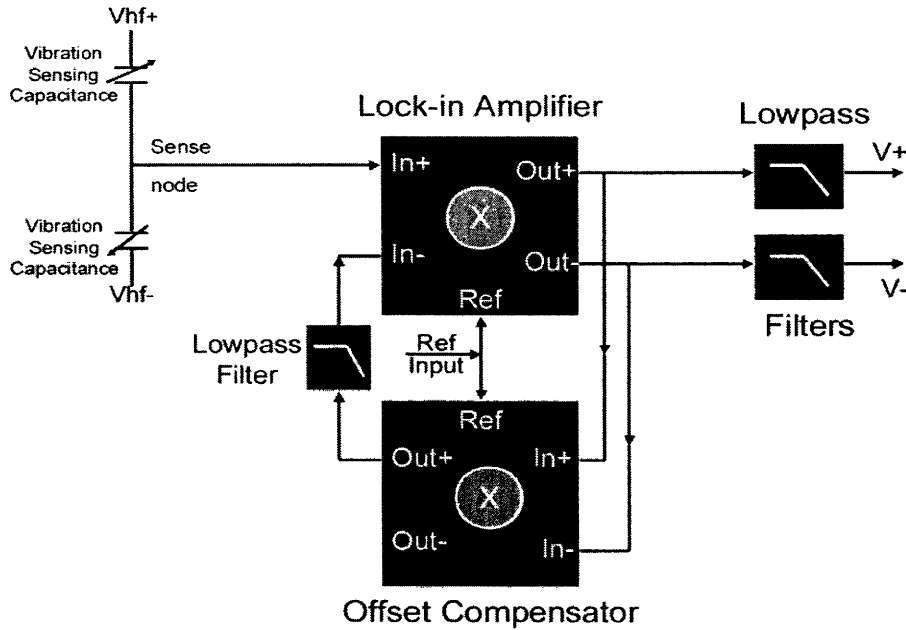


**Figure 2.15: A simple topological representation of the vibration sensor with the new offset-compensated demodulator (the force-feedback OTA and the back-end bandpass amplifier are not shown for simplicity)**

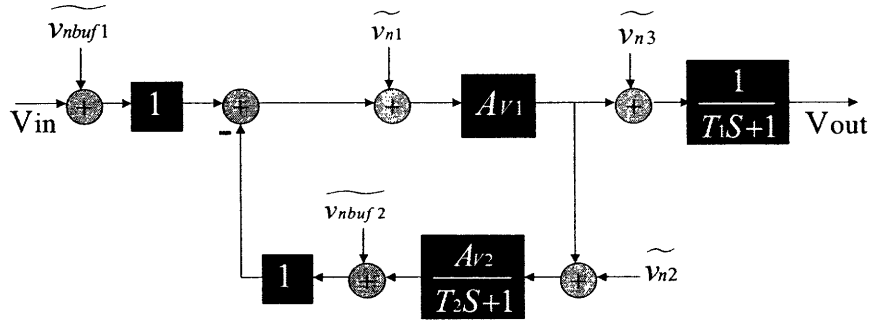
the offset that may be originated from the mismatch of  $Q_3$ - $Q_6$  or the two output resistors ( $R$ ) next to  $V_+$  and  $V_-$ , as these components are basically out of the compensating loop).

Figure 2.15 shows a simplified topological representation of the vibration sensor with the new offset-compensated demodulator. A single multiplier cell (lock-in amplifier) represents both parallel Gilbert multiplier cells in the forward path. As observed in this figure, the non-filtered output goes to the offset compensator, while the lowpass-filtered output forms the ultimate demodulator block's output (i.e.  $V_+$  and  $V_-$ ). Note that the force-feedback OTA and the back-end bandpass amplifier are not shown for simplicity.

### 2.2.1 SIGNAL AND NOISE ANALYSIS OF THE OFFSET-COMPENSATED DEMODULATOR BLOCK

Figure 2.16 shows the block diagram of the newly designed demodulator along with its various noise-generating sources. In this figure,  $A_{V1}$  denotes the gain of the forward-path Gilbert multipliers and  $\tilde{V}_{n1}$  is their input-referred noise.  $A_{V2}$  and  $\tilde{V}_{n2}$  represent the gain and input-referred noise of the feedback-path multiplier (offset compensator).  $T_1$  is the output lowpass filter time constant of  $C_1$  (which is out of the feedback loop) with  $\tilde{V}_{n3}$  denoting its noise.  $T_2$  is the feedback lowpass filter time constant of  $C_2$ , required for extracting the offset information.  $\tilde{V}_{nbuf1}$  and  $\tilde{V}_{nbuf2}$  are the input buffers input-referred noise sources.

Note that the values of both  $A_{V1}$  and  $A_{V2}$  actually depend on the multipliers second input (the Ref input:  $V_{ref}$ ). Repeating equations (2.5), (2.6), and (2.9) here for simplicity (and



**Figure 2.16: Block diagram of the offset-compensated demodulator with its various noise-generating sources**

considering that our block's main input is single-ended, rather than differential), we have:

$$A_{v1} = \frac{1}{2} \frac{R I_{amp}}{2 V_{TH}} \left( \tanh \left( \frac{V_{ref}}{2 V_{TH}} \right) \right) \approx \left( \frac{R I_{amp}}{8 V_{TH}^2} \right) V_{ref} \quad (2.13)$$

$$A_{v2} = R_T \sqrt{K_p I_{comp}} \left( \tanh \left( \frac{V_{ref}}{2 V_{TH}} \right) \right) \approx \frac{R_T \sqrt{K_p I_{comp}}}{2 V_{TH}} V_{ref} \quad (2.14)$$

$$K_p = \frac{1}{2} \mu_p C_{ox} \frac{W}{L}$$

We have designated the bias current of each forward-path Gilbert multiplier (lock-in amplifier) as  $I_{amp}$  (i.e.  $I_{CQ11} = I_{amp}$  in figure 2.13) and the bias current of the feedback multiplier (offset compensator) as  $I_{comp}$  (i.e.  $I_{Dr7} + I_{Dr8} = I_{comp}$  in figure 2.13).  $R_T$  denotes the output resistance of the offset compensator.

Now we shall analyze the gain and noise behavior of this block. The first step is to calculate the transfer function:

$$\frac{V_{out}}{V_{in}} = H(S) = \frac{A_{v1}}{1 + \frac{A_{v1} A_{v2}}{T_2 S + 1}} \times \frac{1}{T_1 S + 1} = \frac{A_{v1} (T_2 S + 1)}{(T_1 S + 1) (T_2 S + 1 + A_{v1} A_{v2})} =$$



$$\frac{A_{v1}(T_2S+1)}{T_1T_2S^2 + [T_2 + (1 + A_{v1}A_{v2})T_1]S + 1 + A_{v1}A_{v2}} = A_v \frac{T_2S+1}{\tau^2S^2 + \frac{\tau}{Q}S + 1} \quad (2.15)$$

$$A_v = \frac{A_{v1}}{1 + A_{v1}A_{v2}} \approx \frac{1}{A_{v2}} \quad (2.16)$$

$$\tau = \sqrt{\frac{T_1T_2}{1 + A_{v1}A_{v2}}} \quad (2.17)$$

$$Q = \frac{\sqrt{T_1T_2(1 + A_{v1}A_{v2})}}{T_2 + (1 + A_{v1}A_{v2})T_1} \quad (2.18)$$

The parameters are as follow:

$$T_1 = RC_1, \quad T_2 = R_7C_2, \quad R_T \approx (r_{oQ18}g_{mQ18}r_{oQ20}) \parallel (r_{oT16}g_{mT16}r_{oT15})$$

$$A_{v_{\max}} = \text{Maximum Gain} \approx A_{v1}$$

Equation (2.15) suggests that the new offset-compensated demodulator has basically the form of a bandpass filter with some gain. This is exactly the behavior we were looking for. The function we are expecting from the demodulator block is to filter out all the high-frequency (unwanted) noise and errors (refer to figure 2.3), as well as to compensate and nullify the DC (and other very low-frequency) components. The pass-band of this resulting bandpass filter should be coincident with the frequency range of input vibrations we wish to sense.

Figure 2.17(a) shows the root-locus plot of the feedback loop employed in the offset-compensated demodulator with its block diagram shown in figure 2.16. Note that the lowpass filter  $\frac{1}{T_1S+1}$  is essentially out of loop, so it does not show up in the root-locus.

Figure 2.17(b) shows the resulting pole-zero map of the block. The zero of the transfer function is at  $z = \frac{1}{T_2}$ , while the second pole is at  $p_2 = \frac{1}{T_1}$ .

The next step is to calculate each noise-generating source. However, we should emphasize one fact at this stage: the low-frequency noise (including flicker noise) of the lock-in amplifier and the input buffers (i.e. T<sub>1</sub>-T<sub>4</sub> in figure 2.13) won't be taken into our noise calculation. The reason is, as we previously discussed in detail and illustrated in figure 2.3, since we are employing a lock-in technique, this low-frequency noise will be multiplied by the high carrier frequency of the Ref input and then in later stages lowpass filtered and thus eliminated in the ultimate output of the block. However, it should be mentioned that flicker noise of the offset compensator matters and should be taken into account. It is obvious that the thermal noise of all parts should also be considered.

$$\overline{V_{nbuf1}^2} = \frac{8KT}{3g_{mT1}} \left[ 1 + \frac{g_{mT3}}{g_{mT1}} \right] \frac{V^2}{Hz}$$

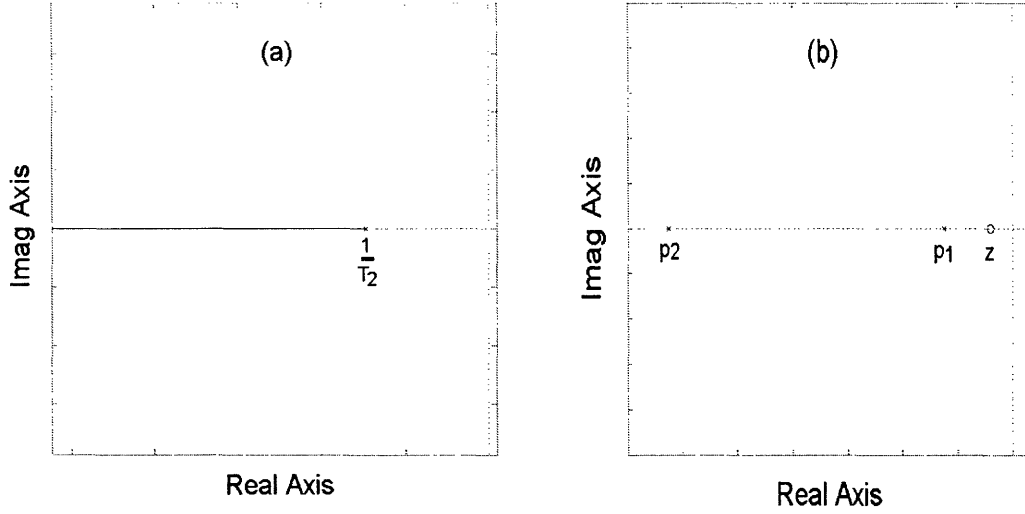


Figure 2.17: (a) Root-locus plot corresponding to the feedback loop of the offset-compensated demodulator (figure 2.16), (b) pole-zero map of this demodulator (not drawn to scale)

$$\begin{aligned} \widetilde{V}_{nbu\dot{f}^2} &= \frac{8KT}{3g_{mT2}} \left[ 1 + \frac{g_{mT4}}{g_{mT2}} \right] \frac{V^2}{Hz} \\ \widetilde{V}_{n1}^2 &= \frac{1}{A_{v1}^2} \left[ 2q(I_{CQ7} + I_{CQ8} + I_{CQ9} + I_{CQ10})R^2 + 4KT \times 4r_b \times g_{mQ7}^2 R^2 + 8KTR \right] = \\ &= \frac{1}{A_{v1}^2} \left[ 2qI_{amp}R^2 + 16KTr_b \left( \frac{I_{amp}}{4V_{TH}} \right)^2 R^2 + 8KTR \right] \frac{V^2}{Hz} \\ \widetilde{V}_{n3}^2 &= 2q(I_{CQ3} + I_{CQ4} + I_{CQ5} + I_{CQ6})R^2 + 4KT \times 4r_b \times g_{mQ3}^2 R^2 + 8KTR = \\ &= 2qI_{amp}R^2 + 16KTr_b \left( \frac{I_{amp}}{4V_{TH}} \right)^2 R^2 + 8KTR = A_{v1}^2 \widetilde{V}_{n1}^2 \frac{V^2}{Hz} \\ \widetilde{V}_{n2}^2 &= \frac{R_T^2}{A_{v2}^2} \left[ 4 \left( \frac{8KT \times g_{mT9}}{3} + \frac{K_f g_{mT9}^2}{W_{T9} L_{T9} C_{ox}^2 f} \right) + 8 \left( \frac{1}{2} \right)^2 (2qI_{CQ17} + 4KTr_b \times g_{mQ17}^2) \right] + \\ &= \frac{R_T^2}{A_{v2}^2} \left[ 4 \left( \frac{1}{2} \right)^2 \left( \frac{8KT \times g_{mT13}}{3} + \frac{K_f g_{mT13}^2}{W_{T13} L_{T13} C_{ox}^2 f} \right) \right] = \\ &= \frac{R_T^2}{A_{v2}^2} \left[ \frac{32KT}{3} g_{mT9} + \frac{4K_f g_{mT9}^2}{W_{T9} L_{T9} C_{ox}^2 f} + 2qI_{comp} + 8KTr_b \left( \frac{I_{comp}}{2V_{TH}} \right)^2 + \frac{8KT}{3} g_{mT13} + \frac{K_f g_{mT13}^2}{W_{T13} L_{T13} C_{ox}^2 f} \right] \frac{V^2}{Hz} \end{aligned}$$

In the process of calculating the input-referred noise of the Gilbert multipliers and also the offset compensator above, we noticed that the base shot-noise current sources of all the bipolar transistors in the circuit actually flow into certain low-impedance nodes that these sources happen to be all connected to. They do not flow into their corresponding base terminals. As the result, the equivalent collector noise current spectral density of all

the bipolar transistors turns out to be almost  $2qI_c$ , not  $2q\beta I_c$ . Another point to mention is that the gain from the noise-generating sources associated with two sets of cascode current mirrors in the offset compensator (i.e. T<sub>13</sub>-T<sub>16</sub> and Q<sub>17</sub>-Q<sub>24</sub> in figure 2.13) to the compensator's output is half. This is why we used a factor of  $\frac{1}{2}$  a couple of times while

determining the compensator's input-referred noise ( $\widetilde{V}_{n2}$ ) above. Lastly, because of the differential nature of the outputs of the circuit, the noises due to Q<sub>1</sub>, Q<sub>2</sub>, Q<sub>11</sub>-Q<sub>16</sub>, and T<sub>5</sub>-T<sub>8</sub> do not show up in the output of the block.

Now with the help of figure 2.16, we should obtain the transfer function from each noise-generating source to the block's ultimate output in order to evaluate the contribution of each noise source. The total noise will be the sum of the squares of each noise component.

$$\begin{aligned} \frac{V_{out}}{\widetilde{V}_{n1}} &= \frac{V_{out}}{V_{nbuf1}} = \frac{V_{out}}{V_{nbuf2}} = \frac{V_{out}}{V_{in}} = H(S) \\ \frac{V_{out}}{\widetilde{V}_{n2}} &= \frac{\frac{Av_1 Av_2}{T_2 S + 1}}{1 + \frac{Av_1 Av_2}{T_2 S + 1}} \times \frac{1}{T_1 S + 1} = \frac{Av_2}{T_2 S + 1} H(S) \\ \frac{V_{out}}{\widetilde{V}_{n3}} &= \frac{1}{T_1 S + 1} \\ \Rightarrow \widetilde{V}_{n-out}^2 &= |H(S)|^2 \left[ \widetilde{V}_{n1}^2 + \widetilde{V}_{nbuf1}^2 + \widetilde{V}_{nbuf2}^2 + \left| \frac{Av_2}{T_2 S + 1} \right|^2 \widetilde{V}_{n2}^2 \right] + \left| \frac{1}{T_1 S + 1} \right|^2 \widetilde{V}_{n3}^2 \quad \frac{V^2}{Hz} \quad (2.19) \end{aligned}$$

If we refer the total noise back to the input, by dividing the total output noise by the input-output transfer function (i.e. H(S)), the equivalent input-referred noise of the demodulator block will turn out to be:

$$\Rightarrow \widetilde{V}_{n-in}^2 = \widetilde{V}_{nAmp/Comp}^2 = \widetilde{V}_{n1}^2 + \widetilde{V}_{nbuf1}^2 + \widetilde{V}_{nbuf2}^2 + \left| \frac{Av_2}{T_2 S + 1} \right|^2 \widetilde{V}_{n2}^2 + \left| \frac{1}{(T_1 S + 1)H(S)} \right|^2 \widetilde{V}_{n3}^2 \quad \frac{V^2}{Hz} \quad (2.20)$$

Let's explore this total input noise spectral density further. First of all, we know that in the pass-band of our resulting bandpass amplifier  $|T_1 S + 1| = 1$  and  $|H(S)| = Av_1$ . On the other hand, earlier we obtained that  $\frac{\widetilde{V}_{n3}^2}{Av_1^2} = \widetilde{V}_{n1}^2$ . This means that the effective noise contribution of the output lowpass filter ( $\widetilde{V}_{n3}^2$ ) is almost the same as  $\widetilde{V}_{n1}^2$ . Next we observe that the lock-in amplifier (forward-path Gilbert multipliers) and input buffers noise ( $\widetilde{V}_{n1}^2 + \widetilde{V}_{nbuf1}^2 + \widetilde{V}_{nbuf2}^2$ ) have a direct contribution at the input, while the noise of the offset compensator ( $\widetilde{V}_{n2}^2$ ) is lowpass filtered. Figure 2.18 illustrates the noise spectral density of the contribution of each noise-generating source at the output, along with the total output noise. We should note that since the total noise is the sum of squares of all the noise components (not their linear sum), the total noise is very close to the largest

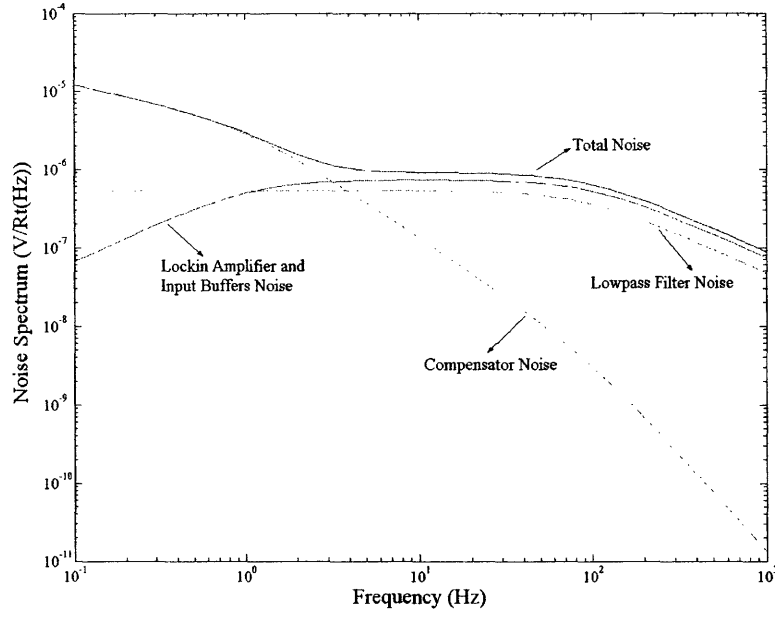


**Figure 2.18: Noise spectral density showing the contribution of each noise-generating source at the output of the offset-compensated demodulator, along with its total output noise.**

component. Figure 2.18 clearly shows that at very low frequencies the flicker noise of the offset compensator ( $\widetilde{V}_{n2}^2$ ) dominates while at higher frequencies the thermal noise of the lock-in amplifier ( $\widetilde{V}_{n1}^2$ ), the input buffers ( $\widetilde{V}_{nbuf1}^2 + \widetilde{V}_{nbuf2}^2$ ), and  $\widetilde{V}_{n3}^2$  become important.

Now it's the time to consider a practical case, analyzing the block numerically and verify it by simulated results. The input vibration frequency range we intend to sense will typically be between 1 and 100Hz. This means we want to discard vibrations with frequencies over 100Hz and at the same time we expect our demodulator to compensate and nullify the DC and low-frequency signals below 1Hz. We use the circuit shown in figure 2.13 with the following settings:

$$V_{dd} = 12V, V_{ss} = -4V, V_{ref} = 100mV, Buf_{bias} = 10V$$

$$R = 10k\Omega, R_b = 12.7k\Omega, C_1 = 160nF, C_2 = 1mF, r_b = 280\Omega$$

$$\Rightarrow I_{amp} = \frac{V_{dd} - V_{ss} - 0.7}{R_b} = \frac{12 + 4 - 0.7}{12.7k} = 1.2mA, I_{comp} = \frac{\left(\frac{W_{T8}}{LT8}\right)}{\left(\frac{W_{T5}}{LT5}\right)} I_{amp} = \frac{\left(\frac{8}{8}\right)}{\left(\frac{200}{3.2}\right)} I_{amp} = 19.2\mu A$$

$$C_{ox} = 1.136 \times 10^{-3} \frac{F}{m^2}, \mu_n C_{ox} = 73.6 \frac{\mu A}{V^2}, \mu_p C_{ox} = 29.4 \frac{\mu A}{V^2}, \frac{K_f}{C_{ox}} = 2 \times 10^{-23} \frac{FV^2}{s}$$

$$W_{T9} = 80\mu m, L_{T9} = 6.4\mu m, W_{T13} = L_{T13} = 8\mu m, R_T = 34M\Omega$$

$$\Rightarrow g_{mT1} = g_{mT2} = 6.13 \times 10^{-4} \frac{A}{V}, g_{mT3} = g_{mT4} = 6.22 \times 10^{-4} \frac{A}{V}, g_{mT9} = 4.37 \times 10^{-5} \frac{A}{V}, g_{mT13} = 1.38 \times 10^{-5} \frac{A}{V}$$

Now we obtain all the parameters of equation (2.15):

$$(2.13) \Rightarrow A_{v1} = 110.6 \frac{V}{V} = 40.9dB$$

$$(2.14) \Rightarrow A_{v2} = 1935 \frac{V}{V} = 65.7dB$$

$$T_1 = RC_1 = 1.6 \times 10^{-3} s, T_2 = R_T C_2 = 34 \times 10^3 s$$

$$(2.17) \Rightarrow \tau = 15.9 \times 10^{-3} s$$

$$(2.18) \Rightarrow Q = 0.1$$

From equation (2.15), we calculate the resulting poles and zero of the transfer function (figure 2.17(b)):

$$z = 2.94 \times 10^{-5} \frac{rad}{s} = 4.68 \times 10^{-6} Hz$$

$$p_1 = 6.29 \frac{rad}{s} = 1Hz$$

$$p_2 = 625 \frac{rad}{s} = 99.5Hz \approx 100Hz$$

Consequently, the pass-band is approximately between 1-100Hz, as we were aiming for.

Figure 2.19 shows the simulated gain response of the demodulator block. The maximum gain (that should be almost  $A_{v1}$ ) appears to be 41.4dB. Calculations had predicted 40.9dB. The -3dB pass-band seems to be between 1.1-115Hz. The conclusion is that the simulated results are in reasonably good agreement with our calculated results.

Now let's figure out the noise of the block. We should first calculate all the noise-generating sources:

$$\widetilde{V_{nbuf1}^2} = \widetilde{V_{nbuf2}^2} = 3.63 \times 10^{-17} \frac{V^2}{Hz}$$

$$\widetilde{V_{n1}^2} = 2.34 \times 10^{-17} \frac{V^2}{Hz}$$

$$\widetilde{V_{n3}^2} = 2.86 \times 10^{-13} \frac{V^2}{Hz}$$

$$\widetilde{V_{n2}^2} = \left( 2.93 \times 10^{-15} + \frac{9.73 \times 10^{-11}}{f} \right) \frac{V^2}{Hz}$$

The next task is to obtain the input-referred noise spectral density by using equation (2.20). To do so, we should remember that in the input vibration-sensing range of interest, the feedback lowpass filter (see figure 2.16) is essentially in effect, meaning that  $|T_2 S + 1| = |T_2 S| = 2\pi T_2 f$ .

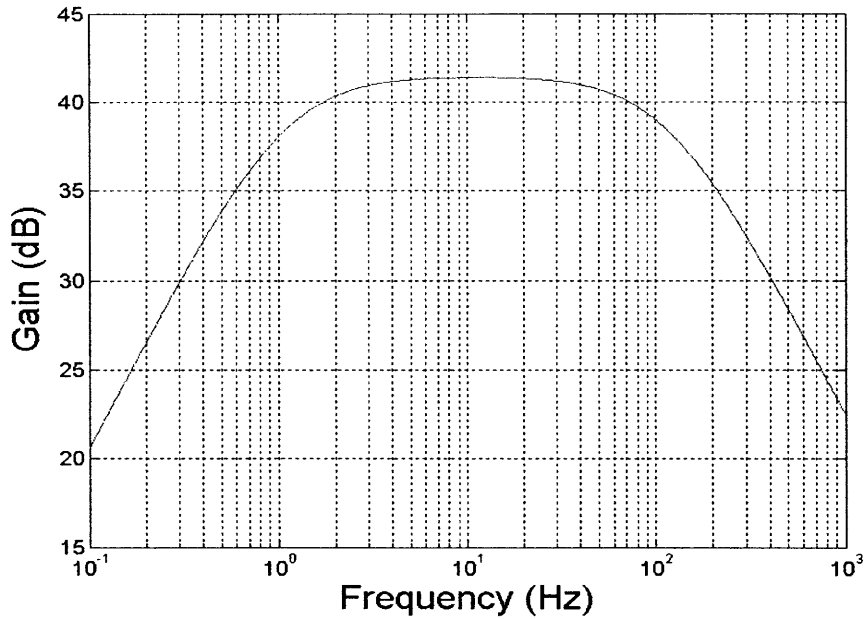


Figure 2.19: Simulated gain response of the offset-compensated demodulator (lock-in amplifier / offset compensator) block

$$(2.20) \Rightarrow \overline{V_{n-in}^2} = \overline{V_{nAmp/Comp}^2} = 1.19 \times 10^{-16} + \frac{8.20 \times 10^{-5}}{f^2} \left( 2.93 \times 10^{-15} + \frac{9.73 \times 10^{-11}}{f} \right) =$$

$$1.19 \times 10^{-16} + \frac{2.40 \times 10^{-19}}{f^2} + \frac{7.98 \times 10^{-15}}{f^3} \frac{V^2}{Hz}$$

And as we know, the input-referred noise RMS value is the square root of the integral of the noise spectral density over the vibration-sensing bandwidth.

$$\Rightarrow \text{Input-referred Noise RMS Value} = \left( \int_1^{100} \overline{V_{n-in}^2} df \right)^{\frac{1}{2}} = 125.6 nV_{rms}$$

Figure 2.20 shows the noise response of the offset-compensated demodulator. It is basically showing the simulated total input-referred noise RMS value of the block. The final value seems to be  $101.5 nV_{rms}$  -- close to our calculation.

Finally, table 2.1 compares the obtained theoretical and simulated results for the most important characteristics of the offset-compensated demodulator block. They seem to be in rather good agreement with each other.

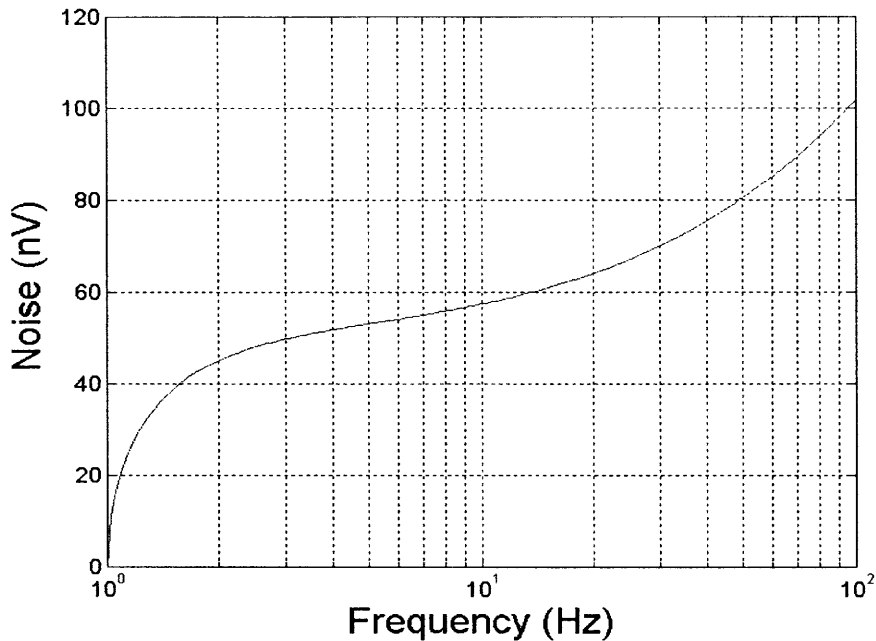


**Figure 2.20: Simulated total input-referred noise RMS value of the offset-compensated demodulator (lock-in amplifier / offset compensator) block**

	Theory	Simulation
Peak Gain (dB)	40.9	41.4
Input-referred noise RMS value (nV)	125.6	101.5

**Table 2.1: Comparison between the theoretical and simulated results for the peak gain and input noise of the offset-compensated demodulator (lock-in amplifier / offset compensator) block**

### 2.3 VIBRATION SENSOR PARASITICS INSENSITIVITY

One of the major drawbacks of present-day vibration sensor schemes (like the one shown in figure 2.4) is the degradation of the signal at its sense node in the presence of parasitics on this node. Since the vibration sensing capacitors are small (around 150fF in a typical vibration sensor) and thus comparable to typical parasitic capacitances that we may have on a chip, the existence of such parasitics will attenuate the signal level considerably. These parasitics may include the moving middle plate-to-substrate capacitance on a VLSI chip and the input capacitance of the succeeding block (i.e. demodulator).

Let's take another look at figure 2.1. At that stage, assuming the parasitic capacitance between the sense node and substrate ( $C_p$ ) was zero, we calculated the voltage at the sense node ( $V_x$ ) to be (equation (2.2)):

$$V_x = V_o \frac{2\Delta C}{2C_o} = V_o \frac{\Delta C}{C_o} \quad (2.21)$$

However, if  $C_p$  is not zero, equation (2.1) showed that this voltage is:

$$V_x = V_o \frac{2\Delta C}{C_T} = V_o \frac{2\Delta C}{2C_o + C_p} = V_o \frac{2\Delta C}{2C_o \left(1 + \frac{C_p}{2C_o}\right)} = V_o \frac{\Delta C}{C_o} \frac{1}{1 + \frac{C_p}{2C_o}} \quad (2.22)$$

Comparing equation (2.22) with equation (2.21) reveals that in the presence of parasitics the signal is attenuated by a factor equal to the ratio of the parasitic capacitance over total vibration sensing capacitance plus 1 (i.e.  $1 + \frac{C_p}{2C_o}$ ). Therefore, the presence of parasitics has a direct effect in reducing the sensitivity of our vibration sensor.

Figure 2.21 shows the output signal waveforms ( $V_+$  and  $V_-$ ) of the vibration sensor incorporating the new offset-compensated demodulator (discussed in section 2.2), with the topological block diagram shown in figure 2.15. The general characteristics of the test input signals are almost the same as the ones we used in section 2.2. Figure 2.21(a) shows the responses when there is no intentional parasitic capacitance between the sense node and substrate. In figure 2.21(b), this capacitance is chosen to be 3pF. In this case, with  $C_p = 3\text{pF}$  and  $C_o = 150\text{fF}$ , from equation (2.22) the signal attenuation factor is expected to be 11. This is almost seen in figures 2.21, as the signal amplitude in figure 2.21(b) is almost one-tenth the amplitude in figure 2.21(a).

One of the proposed solutions to solve this problem is to insert a shield layer underneath the sensor area, on top of the substrate [12]. This layer is actually a heavily doped active region. Then, we could bootstrap this shielding layer (meaning we unity buffer the sensor output node and drive this shield) to nullify the effect of the parasitics between the sense node and this layer. This method is useful to some extent, but it has its own special problems. First, due to resulting discrepancy in DC levels, this method produces an electrostatic force between the moving middle plate and the shielding layer that tends to pull the sensor free structure down to substrate. Second, the shielding layer cannot actually contain all the existing parasitic capacitances. There still remains a noticeable portion of parasitics, which are not bootstrapped and their signal degradation effects show up. Consequently, we need to develop an additional technique to further nullify this effect to be used in conjunction with the above technique.

The solution we are pursuing in this section is to insert a bandpass amplifier between the sensor output (sense node) and the demodulator to perform the first stage of electrical signal conditioning. This amplifier will be used in a closed-loop configuration. Its loop gain will be designed to be high, so the inherent properties of feedback will ensure that even the presence of large parasitics will not degrade the signal performance much.

Since we are using a lock-in technique, this amplifier should be centered around our carrier frequency. A careful investigation of figure 2.3 reveals that the second important advantage of such a scheme is that the amplifier increases the modulated signal level, while at the same time eliminates the low-frequency and out-of-band noise and errors even further. This will improve sensitivity.



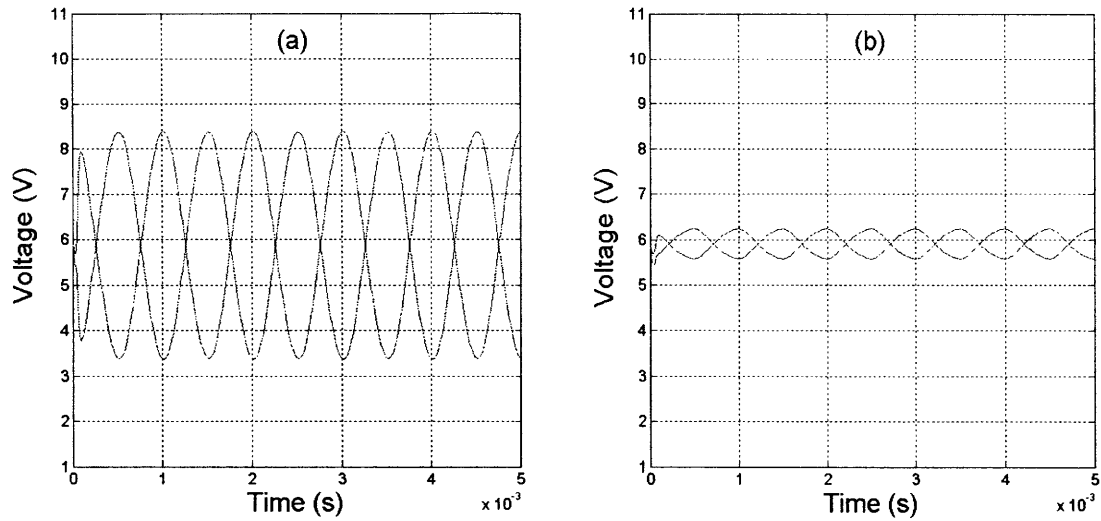


**Figure 2.21: Output signal waveforms of the vibration sensor incorporating the offset-compensated demodulator, with the topological block diagram of figure 2.15, responding to sinusoidal input signals when (a) the intentional parasitic capacitance between the sensor output node (sense node) and substrate is 0, (b) the intentional parasitic capacitance between the sensor output node and substrate is 3pF.**

Note that because from now on this bandpass amplifier is the front-end of the electronic conditioning circuits (not the demodulator block anymore), it will be the most crucial block in determining the noise level, which in turn sets the minimum detectable displacement. Consequently, the noise considerations should be addressed carefully in its analysis.

We should first explore and analyze our designed bandpass amplifier itself. Later, we will talk about its properties and characteristics when used in a feedback closed-loop configuration.

### 2.3.1 SIGNAL AND NOISE ANALYSIS OF THE FRONT-END BANDPASS AMPLIFIER

To generate a bandpass filter behavior, we again use the concepts of feedback. We utilize two lowpass filters: one in the forward path and the other in the feedback path of a feedback loop. As it will be shown later by the help of block diagrams, this combination results in a bandpass characteristic. Intuitively, the feedback-path's lowpass filter passes the low-frequency signals and subtracts it from the input, so they do not show up in the ultimate output. Meanwhile the forward-path's lowpass filter simply rejects all the high-frequency signals; therefore, they do not appear in the output either. Consequently, both the low-frequency and high-frequency signals are eliminated while the medium-frequency ones go through. This is exactly what we expect from a bandpass amplifier.

Figure 2.22 shows the transistor level circuit of the bandpass amplifier used as the front-end of our electronic circuitry. Its first stage is a primary input PMOS differential pair

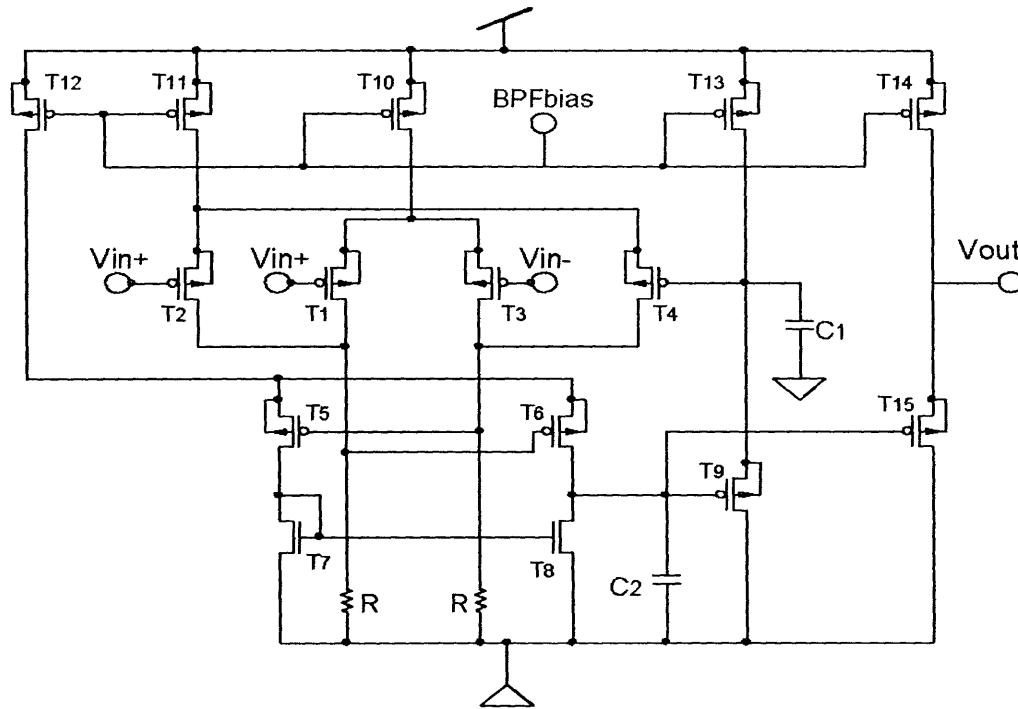


Figure 2.22: Transistor level circuit of the front-end bandpass amplifier

( $T_1$ ,  $T_3$ ) with resistive load ( $R$ ). Because the size of resistors in a chip is rather limited due to their area, the gain of this first stage is usually not high enough for our purposes. Thus, in order to increase our loop gain, we have to use a second gain stage (consisting of  $T_5$ - $T_8$ ). It also serves to convert our differential signal to a single-ended form. This increased loop gain is essential to giving us immunity against parasitics at the amplifier input (the same as the sense node) to substrate when the whole amplifier is used in a closed-loop configuration.  $C_2$  performs the required forward-path lowpass filtering, as mentioned above. The signal is then passed through a buffer ( $T_9$ ), lowpass filtered by  $C_1$  again and fed back to the negative terminal of a secondary input PMOS differential pair ( $T_2$ ,  $T_4$ ) to close the feedback loop. Therefore, the required feedback-path lowpass filtering is done by  $C_1$ . The secondary input pair shares the resistive load ( $R$ ) with the primary input pair.  $T_{15}$  is actually just a level-shifter (buffer) to adjust the amplifier's output DC level, which goes to the succeeding block (i.e. demodulator).  $T_{10}$ - $T_{14}$  are simply bias transistors to provide the bias current to the circuit. To be more specific,  $T_{10}$  biases the primary input pair ( $T_1$ ,  $T_3$ ),  $T_{11}$  biases the secondary input pair ( $T_2$ ,  $T_4$ ),  $T_{12}$  provides the bias current for the gain stage consisting of  $T_5$ - $T_8$ , and  $T_{13}$  and  $T_{14}$  are the bias transistors for the feedback buffer ( $T_9$ ) and output level-shifter ( $T_{15}$ ), respectively.

The reason we used a resistive load rather than a transistor active load is to lower the noise, which is a very important factor in this block. Generally a resistive-load amplifier exhibits less input-referred noise than an active-load amplifier with similar conditions like bias current. Remember that the gain of a resistive-load amplifier is proportional to  $R$ , while its associated noise voltage is proportional to  $\sqrt{R}$ . Hence, the larger the value of  $R$ , the less noise appears at the input due to resistors. However, the upper limit of the resistor value is set by its occupying area, as we previously mentioned.

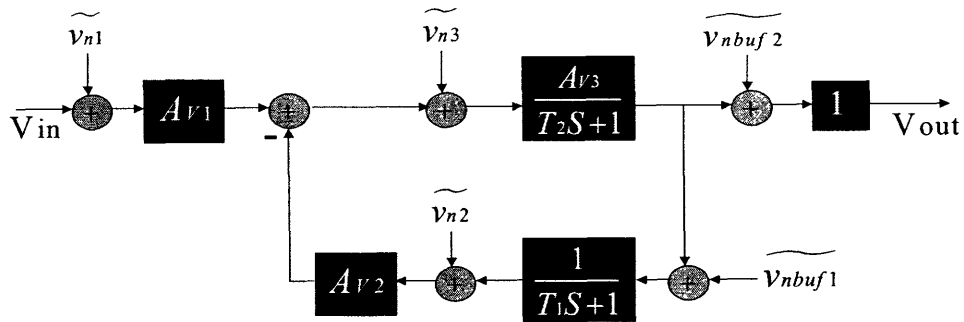


Figure 2.23: Block diagram of the front-end bandpass amplifier, along with its various noise-generating sources

Figure 2.23 shows the block diagram of the front-end bandpass amplifier, along with its various noise-generating sources. We clearly observe the two lowpass filters: one in the forward path and the second in the feedback path. In this figure,  $A_{V1}$  and  $A_{V2}$  are the gains of the primary and secondary input PMOS differential stages with their input-referred noise sources denoted as  $\widetilde{V}_{n1}$  and  $\widetilde{V}_{n2}$ , respectively.  $A_{V3}$  is the gain of the second stage, while  $\widetilde{V}_{n3}$  is its input-referred noise.  $T_2$  and  $T_1$  are the time constants associated with the forward-path and feedback-path lowpass filters, respectively.  $\widetilde{V}_{nbuf1}$  and  $\widetilde{V}_{nbuf2}$  are the input-referred noise sources of the feedback buffer and output level-shifter, respectively.

Before analyzing the gain and noise characteristics of this amplifier, let's first define the notations used in figure 2.23 based on the circuit parameters of figure 2.22.

$$A_{V1} = g_{mT1}R, \quad A_{V2} = g_{mT2}R, \quad A_{V3} = g_{mT5}R_T$$

$$T_1 = \frac{C_1}{g_{mT9}}, \quad T_2 = R_T C_2, \quad R_T = r_{oT6} \parallel r_{oT8}$$

$R_T$  denotes the resistance seen at the node that  $C_2$  is connected to, which is the same node that the gate terminals of  $T_9$  and  $T_{15}$  and the drains of  $T_6$  and  $T_8$  are connected to.

Now based on figure 2.23, we calculate the transfer function:

$$\frac{V_{out}}{V_{in}} = G(S) = \frac{A_{v1} \frac{A_{v3}}{T_2 S + 1}}{1 + \frac{A_{v2} A_{v3}}{(T_1 S + 1)(T_2 S + 1)}} = \frac{A_{v1} A_{v3} (T_1 S + 1)}{(T_1 S + 1)(T_2 S + 1) + A_{v2} A_{v3}} =$$

$$\frac{A_{v1} A_{v3} (T_1 S + 1)}{T_1 T_2 S^2 + (T_1 + T_2) S + (1 + A_{v2} A_{v3})} = A_v \frac{T_1 S + 1}{\tau^2 S^2 + \frac{\tau}{Q} S + 1} \quad (2.23)$$

$$A_v = \frac{A_{v1} A_{v3}}{1 + A_{v2} A_{v3}} = \frac{A_{v1}}{A_{v2}} = \frac{g_{mT1}}{g_{mT2}} \quad (2.24)$$

$$\tau = \sqrt{\frac{T_1 T_2}{1 + A_{v2} A_{v3}}} \quad (2.25)$$

$$Q = \frac{\sqrt{T_1 T_2 (1 + A_{v2} A_{v3})}}{T_1 + T_2} \quad (2.26)$$

$$A_{v \max} = \text{Maximum Gain} = A_{v1} A_{v3}$$

Equation (2.23) is in the form of a bandpass filter with some gain. Therefore, as we had promised before, by analyzing the block diagrams we showed that the combination of two lowpass filters, one in the forward path and the other in the feedback path can result in a bandpass characteristic.

Figure 2.24(a) shows the root-locus plot of the feedback loop described in figure 2.23. Note that the two poles approach each other and then depart from the real axis. Figure 2.24(b) shows the pole-zero map of this block. In this figure,  $p_1$  and  $p_2$  are the two resulting poles, while  $z = \frac{1}{T_1}$  is the transfer function zero, which is basically the pole of the feedback path.

The next step is to calculate each noise-generating source. Again we should emphasize that the low-frequency noise (including flicker noise) of this block does not matter and won't show up in our noise calculation. The reason is again the employment of lock-in technique, illustrated in figures 2.2 and 2.3. As we saw, this low-frequency noise will be multiplied by the high carrier frequency later in the demodulator block and then lowpass filtered and thus eliminated in the ultimate output of the vibration sensor.

$$\widetilde{V}_{n1}^2 = 2 \times \frac{8KT}{3g_{mT1}} = \frac{16KT}{3g_{mT1}} \frac{V^2}{Hz}$$

$$\widetilde{V}_{n2}^2 = 2 \times \frac{8KT}{3g_{mT2}} = \frac{16KT}{3g_{mT2}} \frac{V^2}{Hz}$$

$$\widetilde{V}_{n3}^2 = 2 \times 4KTR + 2 \times \frac{8KT}{3g_{mT5}} + 2 \times \frac{8KTg_{mT7}}{3g_{mT5}^2} = 8KTR + \frac{16KT}{3g_{mT5}} \left[ 1 + \frac{g_{mT7}}{g_{mT5}} \right] \frac{V^2}{Hz}$$

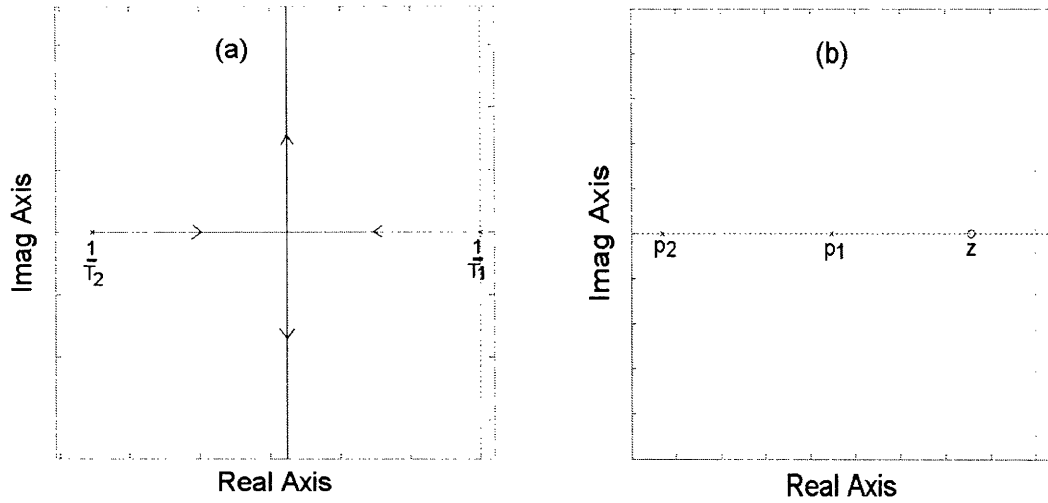


Figure 2.24: (a) Root-locus plot corresponding to the feedback loop of the front-end bandpass amplifier (figure 2.23), (b) pole-zero map of this amplifier (not drawn to scale)

$$\widetilde{V_{nbuf1}^2} = \frac{8KT}{3g_{mT9}} \left[ 1 + \frac{g_{mT13}}{g_{mT9}} \right] \frac{V^2}{Hz}$$

$$\widetilde{V_{nbuf2}^2} = \frac{8KT}{3g_{mT15}} \left[ 1 + \frac{g_{mT14}}{g_{mT15}} \right] \frac{V^2}{Hz}$$

Note that because of the symmetry, as long as the Common-Mode Rejection Ratio (CMRR) of the amplifier is high, we can ignore the noises due to  $T_{10}$ - $T_{12}$ .

Now with the help of figure 2.23, we obtain the transfer function from each noise-generating source to the block's output in order to evaluate the contribution of each noise source. The total noise will be the sum of the squares of each noise component.

$$\frac{V_{out}}{\widetilde{V_{n1}}} = \frac{V_{out}}{V_{in}} = G(S)$$

$$\frac{V_{out}}{\widetilde{V_{n2}}} = \frac{\frac{A_{V2}A_{V3}}{T_2S+1}}{1 + \frac{A_{V2}A_{V3}}{(T_1S+1)(T_2S+1)}} = \frac{A_{V2}}{A_{V1}} G(S)$$

$$\frac{V_{out}}{\widetilde{V_{n3}}} = \frac{\frac{A_{V3}}{T_2S+1}}{1 + \frac{A_{V2}A_{V3}}{(T_1S+1)(T_2S+1)}} = \frac{1}{A_{V1}} G(S)$$

$$\frac{V_{out}}{\widetilde{V}_{nbuf1}} = \frac{\frac{Av_2 Av_3}{(T_1 S + 1)(T_2 S + 1)}}{1 + \frac{Av_2 Av_3}{(T_1 S + 1)(T_2 S + 1)}} = \frac{Av_2}{Av_1} \frac{1}{T_1 S + 1} G(S)$$

$$\frac{V_{out}}{\widetilde{V}_{nbuf2}} = 1$$

$$\Rightarrow \widetilde{V}_{n-out}^2 = |G(S)|^2 \left[ \widetilde{V}_{n1}^2 + \left(\frac{Av_2}{Av_1}\right)^2 \widetilde{V}_{n2}^2 + \left(\frac{1}{Av_1}\right)^2 \widetilde{V}_{n3}^2 + \left(\frac{Av_2}{Av_1}\right)^2 \left|\frac{1}{T_1 S + 1}\right|^2 \widetilde{V}_{nbuf1}^2 \right] + \widetilde{V}_{nbuf2}^2 \frac{V^2}{Hz} \quad (2.27)$$

If we refer the total noise back to the input, by dividing the total output noise by the input-output transfer function (i.e.  $G(S)$ ), the equivalent input-referred noise of the bandpass amplifier block will turn out to be:

$$\Rightarrow \widetilde{V}_{n-in}^2 = \widetilde{V}_{nbuf1}^2 = \widetilde{V}_{n1}^2 + \left(\frac{Av_2}{Av_1}\right)^2 \widetilde{V}_{n2}^2 + \left(\frac{1}{Av_1}\right)^2 \widetilde{V}_{n3}^2 + \left(\frac{Av_2}{Av_1}\right)^2 \left|\frac{1}{T_1 S + 1}\right|^2 \widetilde{V}_{nbuf1}^2 + \left|\frac{1}{G(S)}\right|^2 \widetilde{V}_{nbuf2}^2 \frac{V^2}{Hz} \quad (2.28)$$

Let's discuss this input-referred noise a bit more. First, we know that in the vibration sensing frequency range of interest  $|G(S)| \approx Av_{max} = Av_1 Av_3$  that is much larger than one. Therefore,  $\widetilde{V}_{nbuf2}^2$  can be ignored in the calculations. On the other hand, in this sensing range (located inside the pass-band of the bandpass amplifier), the feedback-path's lowpass filter is active, so  $|T_1 S + 1| \gg 1$ . Consequently, though  $\widetilde{V}_{nbuf1}^2$  is lowpass filtered, its effect can be neglected. Considering that  $Av_1$  is usually equal to  $Av_2$ , we conclude that the input PMOS transistors noise ( $\widetilde{V}_{n1}^2 + \widetilde{V}_{n2}^2$ ) appears directly at the input. The noise of the second gain stage ( $\widetilde{V}_{n3}^2$ ) is divided by the gain of the input stage ( $Av_1$ ) when it's referred back to the input, as expected. However, as  $Av_1$  is not usually that high because we used a resistive load, the effect of  $\widetilde{V}_{n3}^2$  may turn out to be significant. Figure 2.25 illustrates the noise spectral density of the contribution of each noise-generating source at the output of the bandpass amplifier, along with the total output noise. Again as we expect, the total noise is very close to the largest component. This figure clearly shows that the dominant noise source is the thermal noise of input transistors ( $\widetilde{V}_{n1}^2 + \widetilde{V}_{n2}^2$ ) and to some extent the second stage noise ( $\widetilde{V}_{n3}^2$ ). As confirmed again by the figure and according to what we previously mentioned, the noise contributions of the feedback buffer and the output level-shifter (called buffer #1 and buffer #2 in figure 2.25) are negligible.

Now let's reconsider the numerical example of section 2.2.1 and try to extend it to analyze our new bandpass amplifier block. Let's assume that the vibration sensing range of interest is still 100Hz around our carrier frequency chosen to be 500kHz here. This means that the pass-band of our bandpass amplifier should include 500kHz and its neighborhood. To do so, we use the circuit shown in figure 2.22 with the following settings:

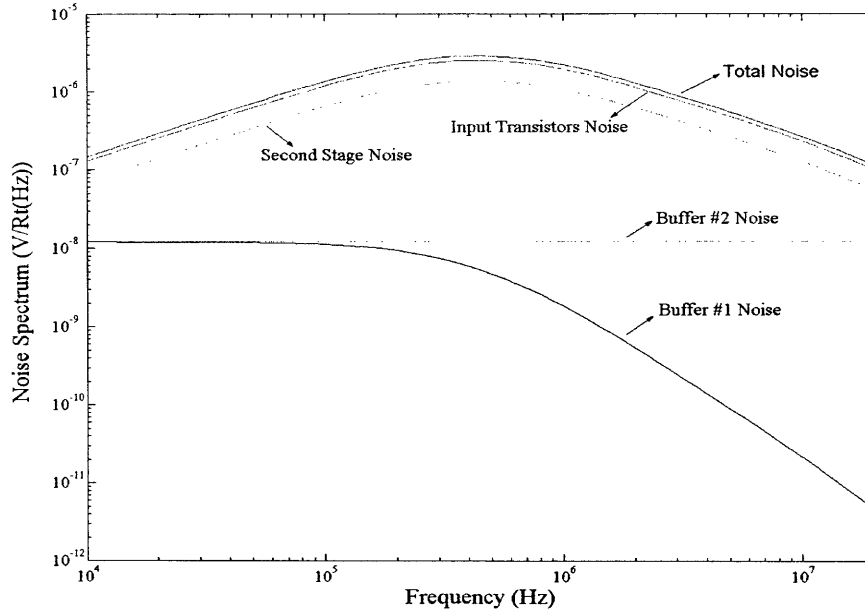


Figure 2.25: Noise spectral density showing the contribution of each noise-generating source at the output of the front-end bandpass amplifier, along with its total output noise.

$$V_{dd} = 12V, V_{ss} = -4V, BPF_{bias} = 10V$$

$$R = 15k\Omega, C_1 = 33nF, C_2 = 100fF$$

$$\Rightarrow g_{mT1} = g_{mT2} = 3.14 \times 10^{-4} \frac{A}{V}, g_{mT5} = 1.41 \times 10^{-4} \frac{A}{V}, g_{mT7} = 2.41 \times 10^{-4} \frac{A}{V}, g_{mT9} = g_{mT15} = 1.87 \times 10^{-4} \frac{A}{V},$$

$$g_{mT13} = g_{mT14} = 2.94 \times 10^{-4} \frac{A}{V}, R_T = 362.3k\Omega$$

Now we obtain all the parameters of equation (2.23):

$$A_{V1} = A_{V2} = g_{mT1}R = 4.71 \frac{V}{V} = 13.5dB, A_{V3} = g_{mT5}R_T = 51.1 \frac{V}{V} = 34.2dB$$

$$T_1 = \frac{C_1}{g_{mT9}} = 1.76 \times 10^{-4}s, T_2 = R_T C_2 = 3.62 \times 10^{-8}s$$

$$(2.25) \Rightarrow \tau = 1.62 \times 10^{-7}s$$

$$(2.26) \Rightarrow Q = 0.22$$

From equation (2.23), the resulting transfer function poles and zero are calculated to be (figure 2.24(b)):

$$z = 5680 \frac{rad}{s} = 905Hz$$

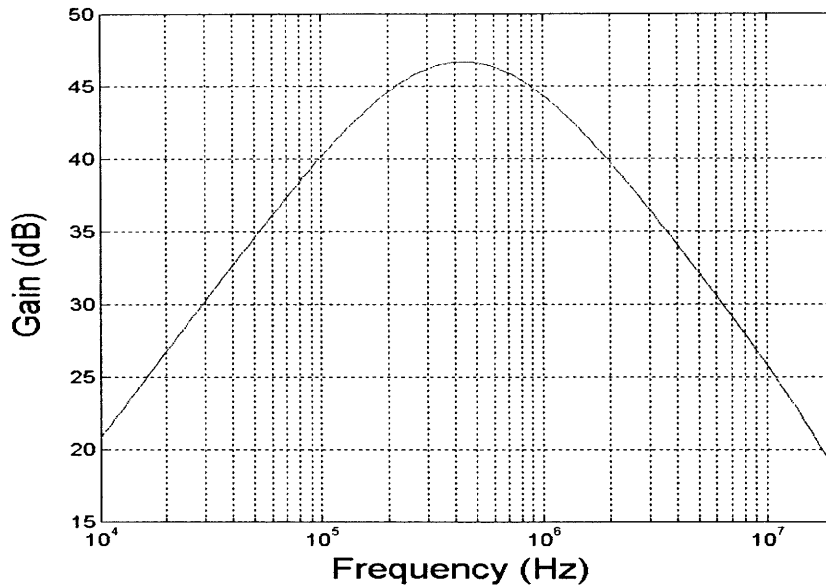


Figure 2.26: Simulated gain response of the front-end bandpass amplifier block

$$p_1 = \left| -\frac{1}{2\tau Q} + \frac{1}{\tau} \sqrt{\frac{1}{4Q^2} - 1} \right| = 1.43 \times 10^6 \frac{rad}{s} = 227.6 kHz$$

$$p_2 = \left| -\frac{1}{2\tau Q} - \frac{1}{\tau} \sqrt{\frac{1}{4Q^2} - 1} \right| = 26.63 \times 10^6 \frac{rad}{s} = 4.2 MHz$$

Therefore, the pass-band contains the 500kHz neighborhood. Note that in case we wish to use a different carrier frequency instead of 500kHz, we can simply change the pass-band of the bandpass amplifier by choosing new values for  $C_1$  and  $C_2$ .

Figure 2.26 shows the simulated gain response of the front-end bandpass amplifier block. The maximum gain appears to be 46.7dB, which happens near the desired 500kHz. Theory had predicted it to be  $A_{V_{max}} = A_{V_1}A_{V_3} = 47.7dB$ , which is close. The -3dB pass-band looks to be between 170kHz-1.13MHz. The observed discrepancy between the calculated and simulated values of the pass-band upper bound originates from the fact that  $C_2=100fF$  is on the order of the parasitic capacitances. Looking at figure 2.22, the actual value of  $C_2$  is larger due to the parasitic capacitances of  $T_6$ ,  $T_8$ ,  $T_9$ , and  $T_{15}$ , which causes our obtained upper limit to be less than expectation. However, because this new pass-band does still include the carrier frequency neighborhood (i.e. 500kHz), our specification is fulfilled. Our upper bound was initially designed to be intentionally high because of this fact.

It's time to figure out the noise of the block. We should first calculate all the noise-generating sources:



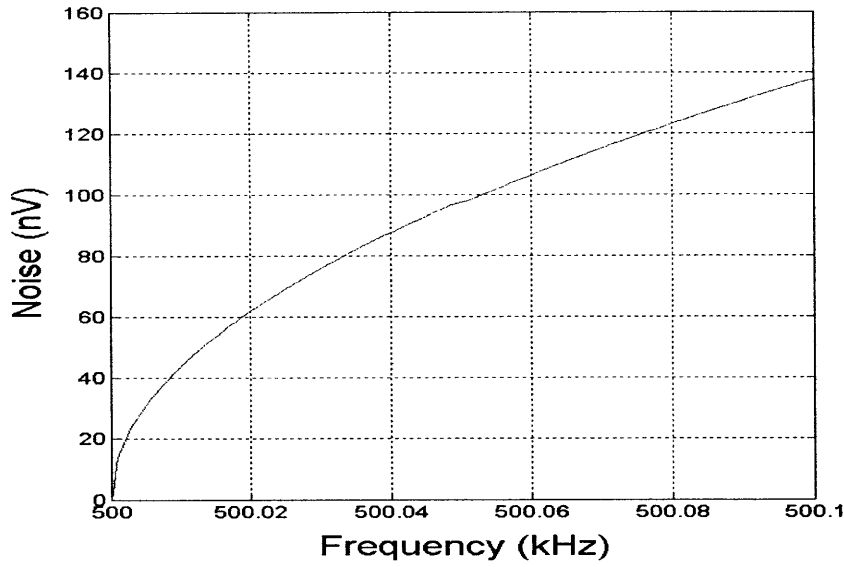


Figure 2.27: Simulated total input-referred noise RMS value of the front-end bandpass amplifier block

$$\widetilde{V_{n1}^2} = \widetilde{V_{n2}^2} = 7.03 \times 10^{-17} \frac{V^2}{Hz}$$

$$\widetilde{V_{n3}^2} = 9.21 \times 10^{-16} \frac{V^2}{Hz}$$

$$\widetilde{V_{nbuf1}^2} = \widetilde{V_{nbuf2}^2} = 1.52 \times 10^{-16} \frac{V^2}{Hz}$$

The next task is to obtain the input-referred noise spectral density by using equation (2.28), neglecting  $\widetilde{V_{nbuf1}^2}$  and  $\widetilde{V_{nbuf2}^2}$ , as mentioned previously.

$$(2.28) \Rightarrow \widetilde{V_{n-in}^2} = \widetilde{V_{nBPA}^2} = 1.82 \times 10^{-16} \frac{V^2}{Hz}$$

The input-referred noise RMS value is the square root of the integral of the noise spectral density over the vibration-sensing bandwidth, which is 100Hz centered on the carrier frequency ( $f_c$ ).

$$\Rightarrow \text{Input-referred Noise RMS Value} = \left( \int_{f_c-1}^{f_c+1} \widetilde{V_{n-in}^2} df \right)^{\frac{1}{2}} = 134.2nV_{rms}$$

Figure 2.27 shows the simulated total input-referred noise RMS value of this block. The final value appears to be  $137.8nV_{rms}$  -- close to theory.

And finally we conclude this section with table 2.2 that compares the obtained theoretical and simulated results for the most important characteristics of the front-end bandpass amplifier block. They are in good agreement with each other.

	Theory	Simulation
Peak Gain (dB)	47.7	46.7
Input-referred noise RMS value (nV)	134.2	137.8

**Table 2.2: Comparison between the theoretical and simulated results for the peak gain and input noise of the front-end bandpass amplifier block**

## 2.4 SIGNAL AND NOISE ANALYSIS OF THE WHOLE NEWLY DESIGNED VIBRATION SENSOR

It's now time to close a feedback loop around the bandpass amplifier discussed in section 2.3.1. The reason we use such a loop is to prevent signal degradation in the presence of parasitics on the sensor output (sense node).

Figure 2.28 shows the topological block representation of the whole improved vibration sensor. It features a couple of newly designed characteristics mentioned earlier, including insensitivity to parasitics at its sense node and automatic offset compensation. The bandpass amplifier at the left is used in a closed-loop configuration. As it will be shown shortly, the nature of its feedback topology makes it inherently insensitive to parasitics. Furthermore, because we are using a lock-in technique, a lock-in amplifier is necessary to extract the baseband input vibration signal (refer to section 2.1.1). Also, the offset compensator serves to automatically nullify the DC offset that might exist in the demodulator block. This figure is basically an improved version of figure 2.15. Note that again the force-feedback OTA and the back-end bandpass amplifier (see section 2.1.2) are not shown for simplicity, as they have not been subject to any change in the course of this thesis.

In order to analyze the whole vibration sensor, we simplify and clarify figure 2.28 and show the result in figure 2.29. Here,  $C_{s1}$  and  $C_{s2}$  are the two vibration sensing capacitances.  $C_p$  represents the parasitic capacitance between the sense node and substrate.  $C_f$  is the feedback capacitor used to close the loop. The two input signals have been renamed to  $V_{in+}$  and  $V_{in-}$ . For our analysis to be more general, we have also included  $R_{adp}$  in figure 2.29 to represent the adaptive element that establishes a DC path from the sense node to ground (refer to section 2.1.2). For all practical purposes, this element can be assumed to be off for signal frequencies (meaning  $R_{adp}$  is extremely large). As the detailed analysis of the lock-in amplifier / offset compensator block (i.e. the offset-compensated demodulator) has been previously done (in section 2.2.1), we simply represent this block by a box in figure 2.29 and concentrate on the analysis of the closed-loop bandpass amplifier.

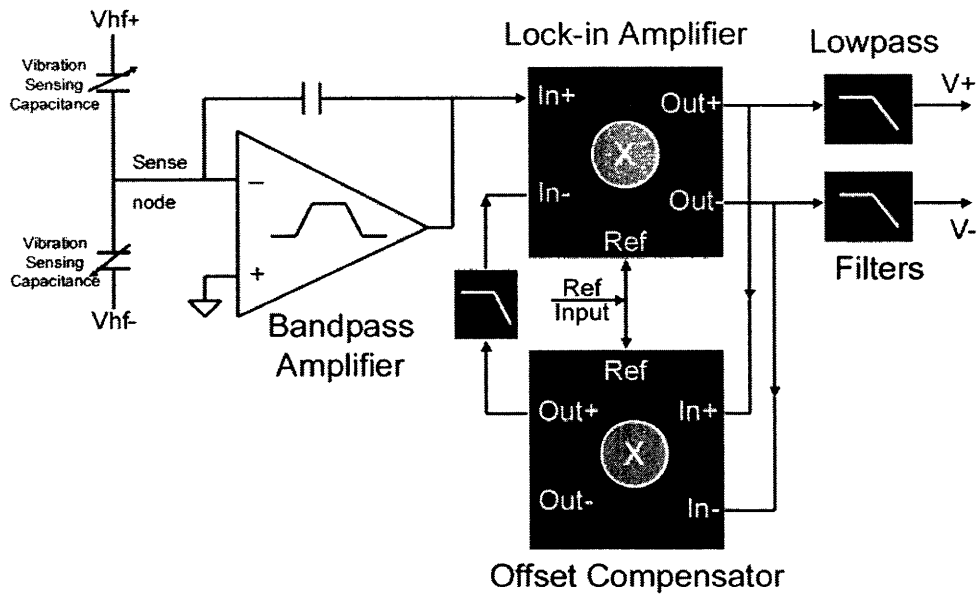


Figure 2.28: A topological block representation of the whole vibration sensor with new features, including insensitivity to parasitics and automatic offset compensation (the force-feedback OTA and the back-end bandpass amplifier are not shown for simplicity)

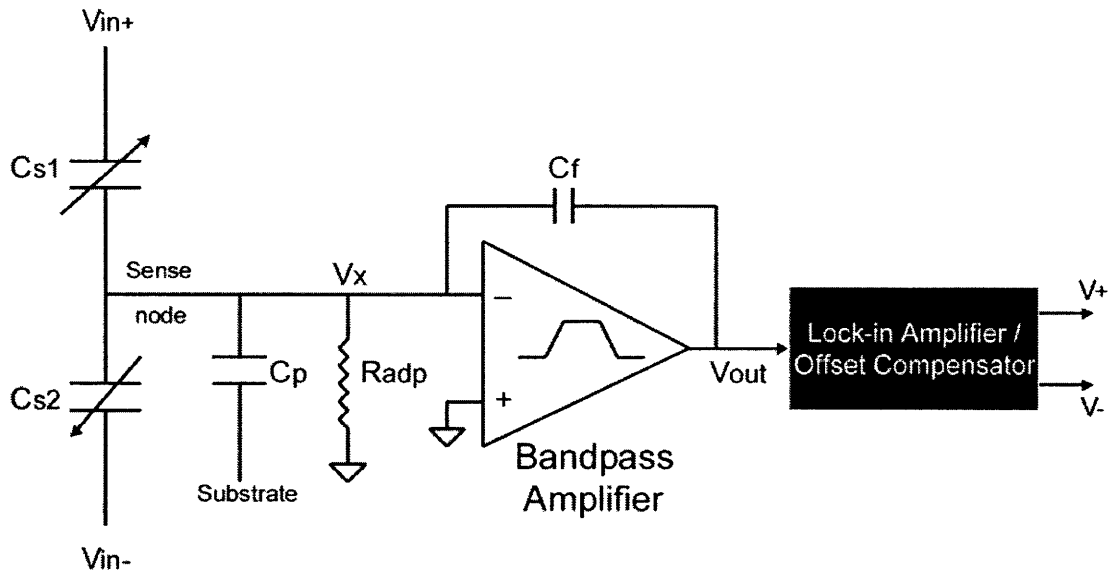
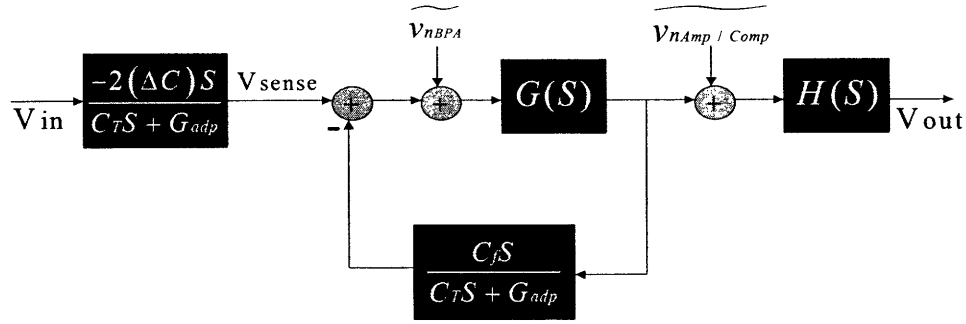


Figure 2.29: A more clarified topological block representation of the whole vibration sensor of figure 2.28, used to analyze the closed-loop bandpass amplifier

Let's first find the voltage signal at the sense node ( $V_x$ ). If we break the loop at the negative terminal of the bandpass amplifier, by superposition we can write (remember that substrate is usually connected to the most negative power supply of the circuit):



**Figure 2.30: Block diagram of the whole vibration sensor with its various noise-generating sources**

$$\Rightarrow V_x = V_{in} \frac{C_{s1}S}{C_T S + G_{adp}} - V_{in} \frac{C_{s2}S}{C_T S + G_{adp}} + V_{out} \frac{C_f S}{C_T S + G_{adp}} \quad (2.29)$$

The following notations have been used:

$$C_{s1} = C_o + \Delta C$$

$$C_{s2} = C_o - \Delta C$$

$$C_T = C_{s1} + C_{s2} + C_p + C_f = 2C_o + C_p + C_f$$

$$G_{adp} = \frac{1}{R_{adp}}$$

Therefore,  $V_x$  is simplified to be:

$$(2.29) \Rightarrow V_x = V_{in} \frac{(C_{s1} - C_{s2})S}{C_T S + G_{adp}} + V_{out} \frac{C_f S}{C_T S + G_{adp}} = V_{in} \frac{2(\Delta C)S}{C_T S + G_{adp}} + V_{out} \frac{C_f S}{C_T S + G_{adp}} \quad (2.30)$$

Based on equation (2.30) with some minor simplifications, we form the block diagram of the whole vibration sensor, shown in figure 2.30. In this figure,  $G(S)$  is the transfer function of the front-end bandpass amplifier (equation (2.23)), while  $\widetilde{V}_{nBPA}$  is its equivalent input-referred noise (equation (2.28)).  $H(S)$  represents the transfer function of the offset-compensated demodulator (lock-in amplifier / offset compensator) block (equation (2.15)) with its input-referred noise (equation (2.20)) denoted as  $\widetilde{V}_{nAmp / Comp}$ .  $C_T$  represents the total capacitances connected to the sense node, as mentioned before. Also the voltage at the sense node ( $V_x$ ) has been renamed to  $V_{sense}$  in this figure. Lastly,  $V_{out}$  in figure 2.30 is actually the final output of the whole vibration sensor, i.e.  $V_+ - V_-$  in figures 2.28 or 2.29.

Now based on figure 2.30, we obtain the input-output transfer function:

$$\frac{V_{out}}{V_{in}} = -\frac{2(\Delta C)S}{C_T S + G_{adp}} \times \frac{G(S)}{1 + G(S) \frac{C_f S}{C_T S + G_{adp}}} \times H(S) = -\frac{2(\Delta C)S \times G(S)}{[C_T + G(S)C_f]S + G_{adp}} H(S) \quad (2.31)$$

Remember that in section 2.3.1 we designed  $|G(S)|$  (the gain of the front-end bandpass amplifier) to be much larger than one in the vibration frequency range of interest. Therefore, we can approximate:

$$(2.31) \Rightarrow \frac{V_{out}}{V_{in}} \approx -\frac{2(\Delta C)S \times G(S)}{C_f S \times G(S)} H(S) = -\frac{2(\Delta C)}{C_f} H(S) \quad (2.32)$$

The conclusion is that no matter of the size of our parasitic capacitance ( $C_p$ ), as long as the loop gain, which is proportional to  $|G(S)|$ , is much larger than one (to be more specific as long as  $|G(S)| \gg \frac{C_T}{C_f}$ ), our signal gain remains almost fixed at  $-\frac{2(\Delta C)}{C_f} H(S)$ .

In other words, the existence of parasitic capacitance between the sense node and substrate ( $C_p$ ) might have the effect of reducing our loop gain, but as long as this loop gain still remains much larger than one, the effect of  $C_p$  on the signal gain is negligible. Now it becomes clear why we previously said that if the gain of our bandpass amplifier is high enough, feedback prevents the attenuation of our signal level in the presence of parasitics. Furthermore, although as we mentioned before  $G_{adp}$  is extremely small, the above discussion is independent of the value of  $G_{adp}$ .

Another point to notice is that equation (2.32) suggests that the signal gain from the primary input to the input of the offset-compensated demodulator block is now  $\frac{-2(\Delta C)}{C_f}$ .

Looking back to equations (2.1) or (2.22), this gain was previously  $\frac{2(\Delta C)}{C_T}$ . This means that the absolute gain is now larger than before by a factor of  $\frac{C_T}{C_f}$ . Recall that

$$C_T = 2C_o + C_p + C_f.$$

Having utilized this new feedback scheme, figure 2.31 clearly illustrates the immunity of our new circuit against parasitics. It shows the output signal waveforms (i.e.  $V_+$  and  $V_-$ ) of the whole vibration sensor of figure 2.28, which incorporates the new closed-loop front-end bandpass amplifier, along with the offset-compensated demodulator. The general characteristics of the test input signals are the same as the ones used to generate the waveforms of the figure 2.21 in section 2.3. Figure 2.31(a) shows the response with no intentional parasitic capacitance between the sense node and substrate. In figure 2.31(b), this capacitance is chosen to be 3pF. As we can clearly see in these figures, the amplitude difference is too small to observe. The signal gain is almost identical. Investigating these waveforms even more carefully reveals that the signal amplitude in

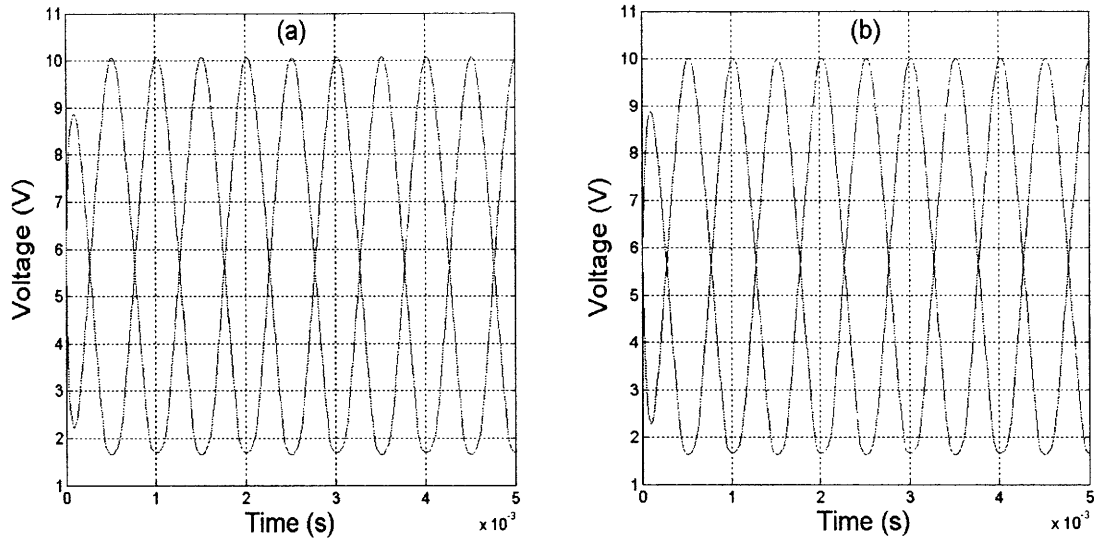


**Figure 2.31: Output signal waveforms of the whole vibration sensor of figure 2.28 that incorporates the new closed-loop front-end bandpass amplifier, along with the offset-compensated demodulator, responding to sinusoidal input signals when (a) the intentional parasitic capacitance between the sensor output node (sense node) and substrate is 0, (b) the intentional parasitic capacitance between the sensor output node and substrate is 3pF.**

figure 2.31(b) is just 1% smaller than the signal amplitude of figure 2.31(a), despite the fact that we chose a huge value for our parasitic capacitance (i.e. 3pF). Compare this tiny attenuation with the one in figure 2.21 where our signal level had decreased with a factor of almost 10! This shows the advantage of our new scheme. Furthermore, comparing the signal amplitude in figure 2.31(a) with the one in figure 2.21(a) shows that our signal gain is higher here. However, the most important characteristic of this gain, as we just pointed out, is its insensitivity to parasitics.

Before we move on to calculate the noise of the block, let's also obtain the transfer function from  $V_{sense}$  to  $V_{out}$ , based on figure 2.30.

$$\frac{V_{out}}{V_{sense}} = \frac{G(S)}{1 + G(S) \frac{C_f S}{C_T S + G_{adp}}} \times H(S) \approx \frac{C_T S + G_{adp}}{C_f S} H(S) \quad (2.33)$$

The approximation has again originated from the fact that  $|G(S)|$  is much larger than one. Now considering that  $G_{adp}$  is very small, we can simplify this transfer function even more.

$$(2.33) \Rightarrow \frac{V_{out}}{V_{sense}} \approx \frac{C_T S}{C_f S} H(S) = \frac{C_T}{C_f} H(S) = \left(1 + \frac{2C_o + C_p}{C_f}\right) H(S) = K(S) \quad (2.34)$$

An important note is that unlike  $\frac{V_{out}}{V_{in}}$ ,  $\frac{V_{out}}{V_{sense}}$  is not independent of  $C_p$ . The larger this parasitic capacitance is, the greater the gain from  $V_{sense}$  to  $V_{out}$  will be. Note that  $K(S)$  is just a new name we have given to  $\frac{C_T}{C_f}H(S)$  in equation (2.34).

Using figure 2.30, we can obtain the transfer function from each noise-generating source to the vibration sensor output in order to evaluate the contribution of each noise source. The total noise will be the sum of the squares of each noise component.

$$\begin{aligned} \frac{V_{out}}{\widetilde{V}_{NBPA}} &= \frac{V_{out}}{V_{sense}} = \frac{C_T}{C_f} H(S) = K(S) \\ \frac{V_{out}}{\widetilde{V}_{NAmp / Comp}} &= H(S) \\ \Rightarrow \widetilde{V}_{n-out}^2 &= |K(S)|^2 \widetilde{V}_{NBPA}^2 + |H(S)|^2 \widetilde{V}_{NAmp / Comp}^2 = |K(S)|^2 \left[ \widetilde{V}_{NBPA}^2 + \left( \frac{C_f}{C_T} \right)^2 \widetilde{V}_{NAmp / Comp}^2 \right] \frac{V^2}{Hz} \quad (2.35) \end{aligned}$$

Here, we will refer this output noise back to the sense node ( $V_{sense}$ ), rather than the input ( $V_{in}$ ). The reason is, that the referred-back noise to the sense node is the one that dictates the minimum electrical signal we can detect on our sensor output (which is the same as the sense node). In other words, input vibrations cause the middle plate of capacitors to move and develop a tiny signal at the sense node. The ultimate quantity of interest for us is the sensor's sensitivity, which is the minimum detectable vibration (or equivalently displacement). We will compute this parameter later based on the total sensor's noise referred back to the sense node. However, for the moment we shall first calculate  $\widetilde{V}_{nsense}^2$  itself by dividing the total sensor's output noise (equation (2.35)) by the transfer function from the sense node to the output (i.e.  $K(S)$ ).

$$\Rightarrow \widetilde{V}_{nsense}^2 = \widetilde{V}_{NBPA}^2 + \left( \frac{C_f}{C_T} \right)^2 \widetilde{V}_{NAmp / Comp}^2 = \widetilde{V}_{NBPA}^2 + \left( \frac{C_f}{2C_o + C_p + C_f} \right)^2 \widetilde{V}_{NAmp / Comp}^2 \frac{V^2}{Hz} \quad (2.36)$$

As we expected from intuition and as equation (2.36) proves, the input-referred noise of the front-end bandpass amplifier ( $\widetilde{V}_{NBPA}^2$ ) appears directly at the sense node while the input-referred noise of the offset-compensated demodulator (lock-in amplifier / offset compensator) block ( $\widetilde{V}_{NAmp / Comp}^2$ ) is attenuated by the closed-loop gain from the sense node to the output of the bandpass amplifier (i.e.  $\frac{C_T}{C_f}$ ), so it has less effect. Consequently, the dominant noise source of the vibration sensor is the noise of the front-end bandpass amplifier. We should also pay attention to the fact that the voltage noise of the adaptive element is multiplied by  $\left| \frac{G_{adp}}{C_T S + G_{adp}} \right|^2$  and appears at the sense node. Since  $G_{adp}$  is extremely small, we ignore the noise contribution of the adaptive element.

It's time to reconsider the numerical analysis of a typical vibration sensor and continue the examples of section 2.2.1 and 2.3.1. Let's keep the input vibration sensing range of interest to be 1-100Hz. We use the circuit of figure 2.28 or its equivalent in figure 2.29.  $C_o$  is chosen to be 150fF, which is a typical number for the vibration sensing capacitances in a present-day vibration sensor. On the other hand, we know (see equation (2.32)) that the signal gain depends on the actual mismatch ( $\Delta C$ ) between the vibration sensing capacitor pair. Therefore, in order to have a typical set of numbers, we presumably choose a 10% mismatch, meaning  $\frac{\Delta C}{C_o} = 0.1$  or  $\Delta C = 15\text{fF}$ .  $C_f$  should be picked to be as

small as possible to maximize the gain (equation (2.32)). However, the minimum reliable value for a capacitor on a VLSI chip might be on the order of 50fF, as smaller ones would be comparable to the typical parasitic capacitances that might be found on the chip. Thus,  $C_f$  is selected to be 50fF.  $C_p$  is mainly due to the input capacitance of the bandpass amplifier. As seen in figure 2.22, the negative input terminal of this amplifier goes to the gate terminal of a PMOS transistor ( $T_3$  in figure 2.22). Consequently, the parasitic capacitance consists of the gate-to-source and gate-to-bulk capacitances of this input transistor. The width and length of this transistor are  $W = 80\mu\text{m}$  and  $L = 3.2\mu\text{m}$ , respectively. With the help of this information and the values for  $C_{gs0}$  and  $C_{gb0}$ , these two capacitances are calculated below:

$$C_{gs} = \frac{2}{3}WLC_{ox} + WC_{gs0} = \frac{2}{3}(80 \times 10^{-6})(3.2 \times 10^{-6})(1.136 \times 10^{-3}) + (80 \times 10^{-6})(2.03 \times 10^{-10}) = 210.1\text{fF}$$

$$C_{gb} = \left(\frac{1-\kappa_p}{3}\right)WLC_{ox} + LC_{gb0} = \left(\frac{1-0.815}{3}\right)(80 \times 10^{-6})(3.2 \times 10^{-6})(1.136 \times 10^{-3}) + (3.2 \times 10^{-6})(1 \times 10^{-11}) = 18.0\text{fF}$$

$$\Rightarrow C_p = C_{gs} + C_{gb} = 210.1 + 18.0 = 228.1\text{fF}$$

As we mentioned before,  $R_{adp}$  is implemented by a PMOS transistor configured as an adaptive element. In all the small signal calculations performed here, its value is assumed to be very high.

In summary, the following values will be used in our numerical analysis:

$$C_o = 150\text{fF}, \Delta C = 15\text{fF}, C_f = 50\text{fF}, C_p = 228.1\text{fF}, C_T = 578.1\text{fF}, G_{adp} \approx 0$$

Before we calculate the total gain of the vibration sensor, let's recall from table 2.1 that the peak gain of the offset-compensated demodulator ( $|H(S)|$ ) is 40.9dB. Equation (2.32) then gives us the total gain of the sensor.

$$(2.32) \Rightarrow \left| \frac{V_{out}}{V_{in}} \right| = \frac{2 \times 15\text{fF}}{50\text{fF}} \times (40.9\text{dB}) = 66.4 \frac{V}{V} = 36.4\text{dB}$$

Equation (2.32) also reveals that the general shape of the input-output transfer function of the whole sensor is the same as the transfer function of the offset-compensated demodulator block ( $H(S)$ ). Therefore, as discussed in section 2.2.1 and particularly in



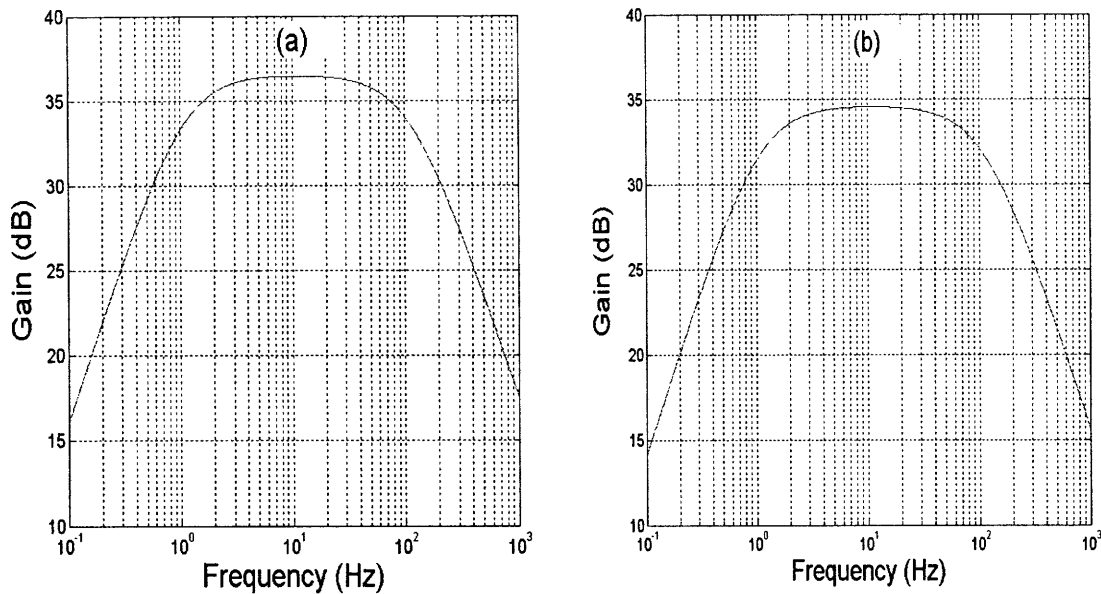


**Figure 2.32: (a) Simulated gain response of the whole vibration sensor of figure 2.28, (b) the same response with an intentional parasitic capacitance of 3pF between the sensor output node (sense node) and substrate**

equation (2.15), it should possess the characteristics of a bandpass amplifier (like the one in figure 2.19) with a pass-band of 1-100Hz and a peak gain of 36.4dB (obtained here).

Figure 2.32(a) shows the simulated gain response of the whole vibration sensor. The maximum gain appears to be 36.5dB -- very close to the theory. The  $-3\text{dB}$  pass-band seems to be almost between 1.1-115Hz, the same as the simulated pass-band of  $H(S)$  in section 2.2.1. Remember that the operation range of the front-end bandpass amplifier is around carrier frequency, while the range of interest for the offset-compensated demodulator is baseband.

Figure 2.32(b) shows the same gain response, but in this case we have added an intentional parasitic capacitance of 3pF between the sense node and substrate. In other words,  $C_p$  is now 3.228pF. We can see that gain has dropped by less than 2dB. Hence, like the transient responses of figure 2.31, the frequency response of figure 2.32(b) also clearly shows the insensitivity of the gain against parasitics.

Now with the help of equation (2.36), we should obtain the spectral density of the noise of the vibration sensor, referred back to the sense node. Fortunately,  $\widehat{V_{NBPA}}^2$  and  $\widehat{V_{NAmp/Comp}}^2$  have been both previously calculated in sections 2.3.1 and 2.2.1, respectively.

$$(2.36) \Rightarrow \widehat{V_{nsense}}^2 = 1.82 \times 10^{-16} + \left( \frac{50}{578.1} \right)^2 \left( 1.19 \times 10^{-16} + \frac{2.40 \times 10^{-19}}{f^2} + \frac{7.98 \times 10^{-15}}{f^3} \right) =$$

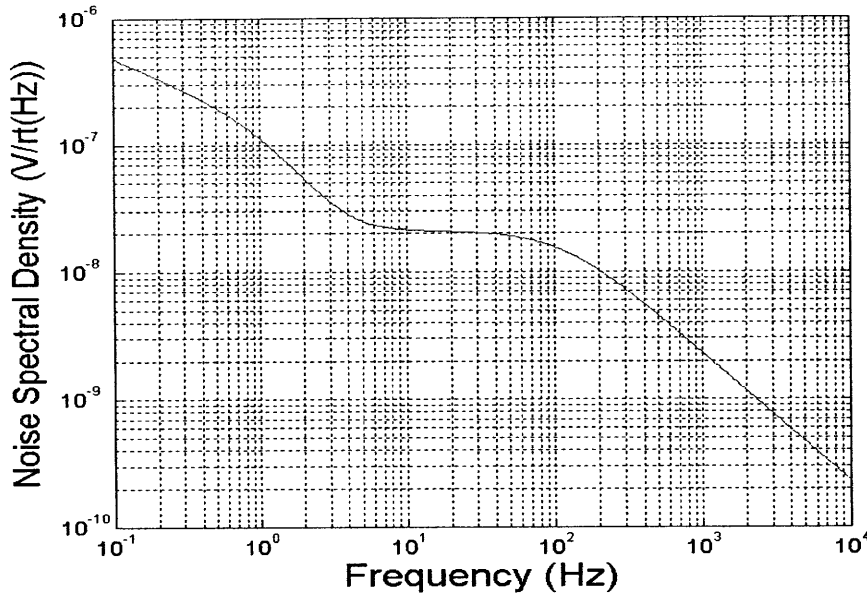


Figure 2.33: Simulated total noise spectral density of the whole vibration sensor, referred back to the sense node

$$1.83 \times 10^{-16} + \frac{1.80 \times 10^{-21}}{f^2} + \frac{5.97 \times 10^{-17}}{f^3} \frac{V^2}{Hz}$$

Figure 2.33 shows the simulated noise spectral density of the whole vibration sensor, when referred back to the sense node. Note that the above equation represents the square of this quantity only in the vibration-sensing range of interest, which is 1-100Hz.

And as before, the vibration sensor noise RMS value referred back to the sense node is the square root of the integral of the noise spectral density (that is figure 2.33 with its vertical axis squared) over the vibration-sensing bandwidth (1-100Hz).

$$\Rightarrow \text{Sense-node-referred Total Noise RMS Value} = \overline{V_{nsenseRMS}} = \left( \int_1^{100} \overline{V_{nsense}^2} df \right)^{\frac{1}{2}} = 134.7nV_{rms}$$

Figure 2.34 shows the simulated total noise RMS value of the whole vibration sensor, when referred back to the sense node. The final value of 128.8nV<sub>rms</sub> is close to our calculation.

Table 2.3 compares the obtained theoretical and simulated results for the most important characteristics of the whole vibration sensor. They include the peak gain of the sensor and also the total noise of the sensor, referred back to the sense node. The results seem to be in good agreement with each other.

As we pointed out earlier, the ultimate quantity of interest to us is the minimum displacement we can detect by our vibration sensor. Input vibrations cause this

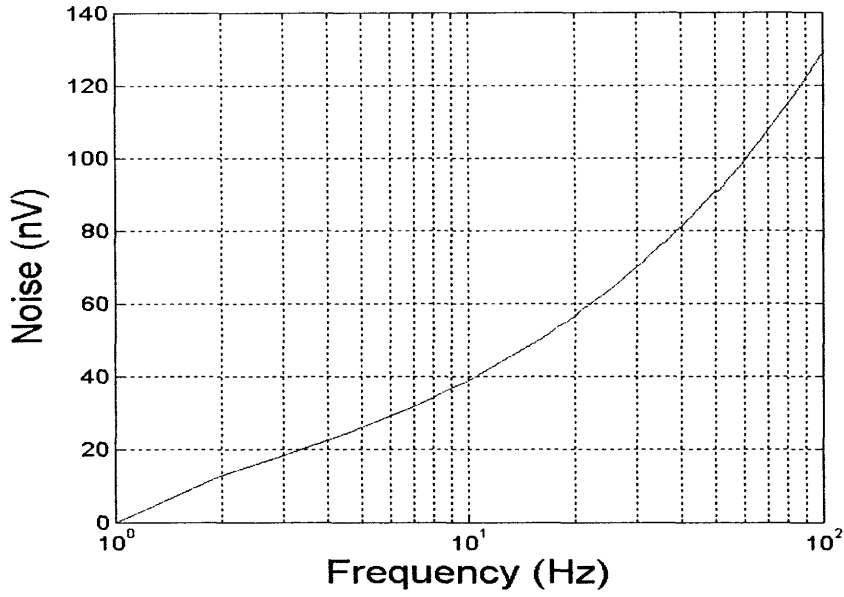


Figure 2.34: Simulated total noise RMS value of the whole vibration sensor, referred back to the sense node

	Theory	Simulation
Peak Gain (dB)	36.4	36.5
Sense-node-referred noise RMS value (nV)	134.7	128.8

Table 2.3: Comparison between the theoretical and simulated results for the peak gain and the sense-node noise of the whole vibration sensor

displacement in the moving middle plate of the sensing capacitors. Naturally, the less displacement we can detect, the more sensitive our vibration sensor will be. Although we obtained the total electrical noise of the sensor referred back to the sense node ( $\widetilde{V}_{nsenseRMS}$ ) above (which gives us the minimum detectable electrical signal at the sense node), we need to express this quantity in terms of a more practical characteristic: minimum detectable displacement. In other words, we should find the minimum detectable displacement corresponding to our electrical noise.

To establish a relationship between these two important parameters, we should refer back to figure 2.30 once more. Let's first find the minimum detectable capacitor mismatch ( $\Delta C_{\min}$ ) between the vibration sensing capacitors. Basically, we wish to find that  $\Delta C$  which produces the same signal power at the sense node as the noise power. This is the definition of the minimum detectable quantity of a certain parameter. With the help of figure 2.30, we equate the signal level and noise level at the sense node. If we name the RMS value of our high (carrier) frequency input signals to be  $V_o$  (figure 2.29), we have:

$$V_o \frac{2(\Delta C_{\min})}{C_T} = \widetilde{V}_{nsenseRMS} \Rightarrow \Delta C_{\min} = \frac{C_T}{2} \frac{\widetilde{V}_{nsenseRMS}}{V_o} \quad (2.37)$$

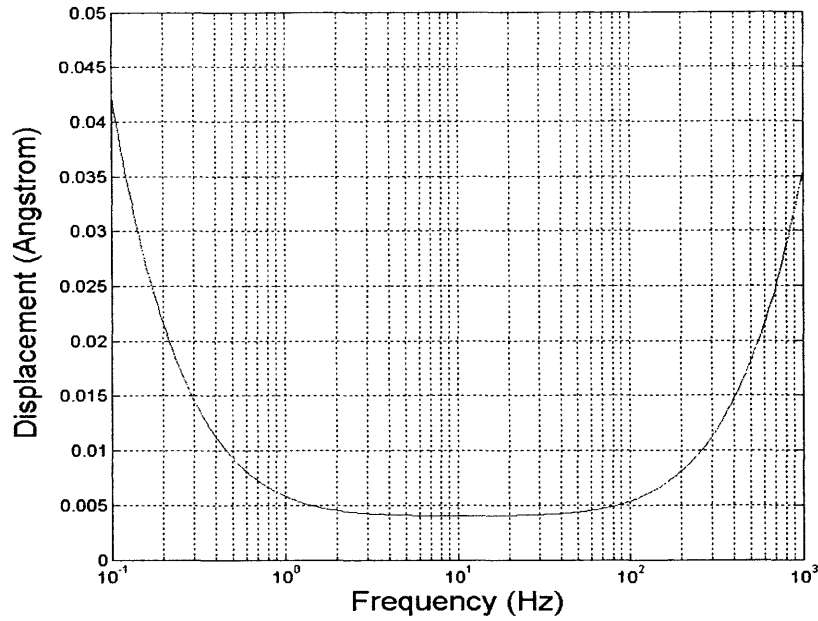


Figure 2.35: “Minimum detectable displacement” frequency response of the whole vibration sensor

Now we can obtain the minimum detectable displacement ( $\Delta x_{\min}$ ) we were looking for. Recall that  $x_o$  represents the distance between the plates of the vibration sensing capacitors (i.e.  $C_{s1}$  and  $C_{s2}$  in figure 2.29) in equilibrium (no input vibration). Equation (2.3) suggests that:

$$(2.3) \Rightarrow \Delta C_{\min} = \frac{C_o}{x_o} \Delta x_{\min} \Rightarrow \Delta x_{\min} = \frac{x_o}{C_o} \Delta C_{\min} \quad (2.38)$$

Now combining equations (2.37) and (2.38), we can write:

$$(2.37), (2.38) \Rightarrow \Delta x_{\min} = \frac{x_o}{C_o} \left( \frac{C_T}{2} \frac{\widetilde{V}_{nsenseRMS}}{V_o} \right) = x_o \left( \frac{C_T}{2C_o} \right) \left( \frac{\widetilde{V}_{nsenseRMS}}{V_o} \right) \quad (2.39)$$

It is important to notice that the minimum detectable displacement ( $\Delta x_{\min}$ ) is proportional to  $C_T$ , which includes the parasitic capacitance ( $C_p$ ). In other words, although parasitics have negligible effect on the signal gain of the vibration sensor (as discussed previously in great detail), they reduce the sensitivity.

Let’s numerically compute the minimum detectable displacement using the values we had in our earlier example. As a reminder, the related parameters were:

$$\widetilde{V}_{nsenseRMS} = 134.7nV, C_o = 150fF, C_T = 578.1fF$$

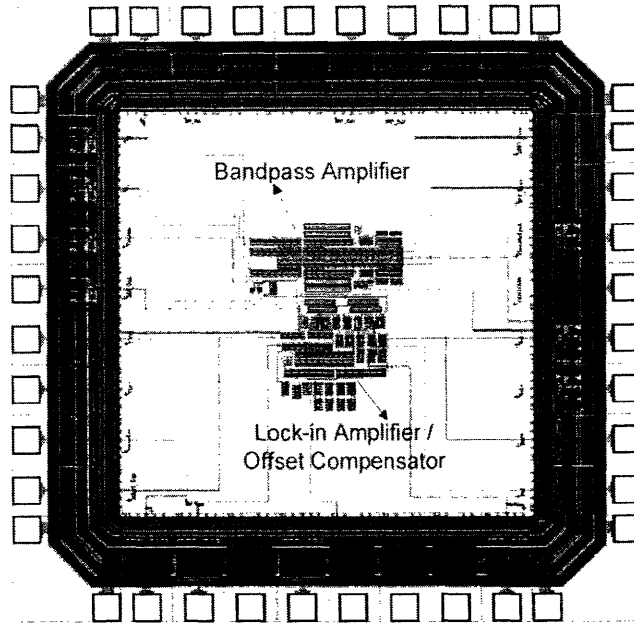


Figure 2.36: Layout of the VLSI fabricated vibration sensor

$V_o$  will be assumed to be  $1V_{\text{rms}}$  and  $x_o$  to be  $1\ \mu\text{m}$ , which can be both typical numbers in a vibration sensor. Therefore, the minimum detectable displacement is calculated to be:

$$(2.39) \Rightarrow \Delta x_{\min} = (1 \times 10^{-6}) \left( \frac{578.1}{2 \times 150} \right) \left( \frac{134.7 \times 10^{-9}}{1} \right) = 2.6 \times 10^{-13} \text{ m} = 2.6 \times 10^{-3} \text{ \AA}$$

Hence, our vibration sensor should be able to sense sub-0.01-angstrom displacements. Figure 2.35 shows the minimum detectable displacement frequency response of the whole vibration sensor. As it was designed to be, the minimum region of this plot is located in the vibration sensing range of interest (i.e. 1-100Hz). This minimum value seems to be almost  $4 \times 10^{-3} \text{ \AA}$ , reasonably close to the theory. As we depart from the vibration sensing range, the minimum detectable displacement rises because the signal gain drops (see figure 2.32(a)). Thus, the best performance of our vibration sensor is in the frequency range of 1-100Hz.

## 2.5 FABRICATION OF THE VIBRATION SENSOR

The foregoing ultra-low-noise vibration sensor with new features like insensitivity to parasitics and automatic offset compensation was fully designed and VLSI fabricated by the MOSIS fabrication service. We used the AMI\_ABN process with 1.5-micron feature size. This n-well CMOS process has two metal layers, two poly layers, and an NPN option.

Figure 2.36 shows the layout of the VLSI fabricated chip, along with its pads. The different building blocks of the vibration sensor are shown in the figure (for a topological block representation of the sensor, refer to figure 2.28). Moreover, the force-feedback OTA and the back-end bandpass amplifier (see section 2.1.2) have been also included in the layout, though they are not explicitly marked in figure 2.36.

## 2.6 EXPERIMENTAL RESULTS OF THE VIBRATION SENSOR

In order to experimentally evaluate our design, the fabricated vibration sensor was carefully tested and characterized. The features we were particularly interested in, were: the sensor's total noise and thus the minimum detectable displacement, its capability to automatically compensate for its offset, and its immunity against the parasitics on its sense node. We present the obtained experimental results below.

### 2.6.1 THE OFFSET-COMPENSATED DEMODULATOR

At first, we focus on the offset-compensated demodulator (lock-in amplifier / offset compensator) block. Figure 2.37(a) shows the experimental output waveforms of this block (with the circuit shown in figure 2.13), responding to sinusoidal input signals. A test 500.05kHz sinusoidal signal as Sig<sub>+</sub> and a 500kHz sinusoid as Ref were used, resulting in a  $500.05 - 500 = 0.05\text{kHz} = 50\text{Hz}$  sinusoid at the output. The DC offset of the Sig and Ref inputs are +100mV and -50mV, respectively. We see that the outputs have almost the same DC level and the non-linearity is small, similar to the simulated response shown in figure 2.14(a). To prove the efficiency of our offset-compensating mechanism, we deactivate our offset-compensating feedback loop by grounding the feedback signal (Sig<sub>-</sub> in figure 2.13), test the circuit, and show the output response of the circuit in figure 2.37(b). Like the simulated results of figure 2.8(b), the experimental outputs do not possess the same DC content anymore and it is easy to observe some non-linearity in them. Furthermore, the signal gain seems to be smaller by a factor of almost 3 compared to figure 2.37(a), where the offset-compensating loop is active.

The slight difference in DC levels that are still observed in the output waveforms of figure 2.37(a) originates from the mismatch of the two output resistors (R) next to V<sub>+</sub> and V<sub>-</sub> in figure 2.13. Although every effort was made in the layout to match the relative value of these resistors (like placing them close to each other, maintaining the same orientation, and similar surrounding circuitry), a minor mismatch seems to exist. As we pointed out in section 2.2, since these components are basically out of the compensating loop, their resulting offset is not nullified. However, all the other offset caused by any other device mismatches in the circuit or the non-zero DC level of circuit inputs has been nullified. Note that in figure 2.37(a), the output port with smaller resistance has both the higher DC level and lower signal gain, as expected.

The other parameter of interest to us is the gain of the offset-compensated demodulator. Figure 2.38 shows the experimental gain response of this block. It has the characteristic of a bandpass filter, as we expected from our analysis and the simulated response of

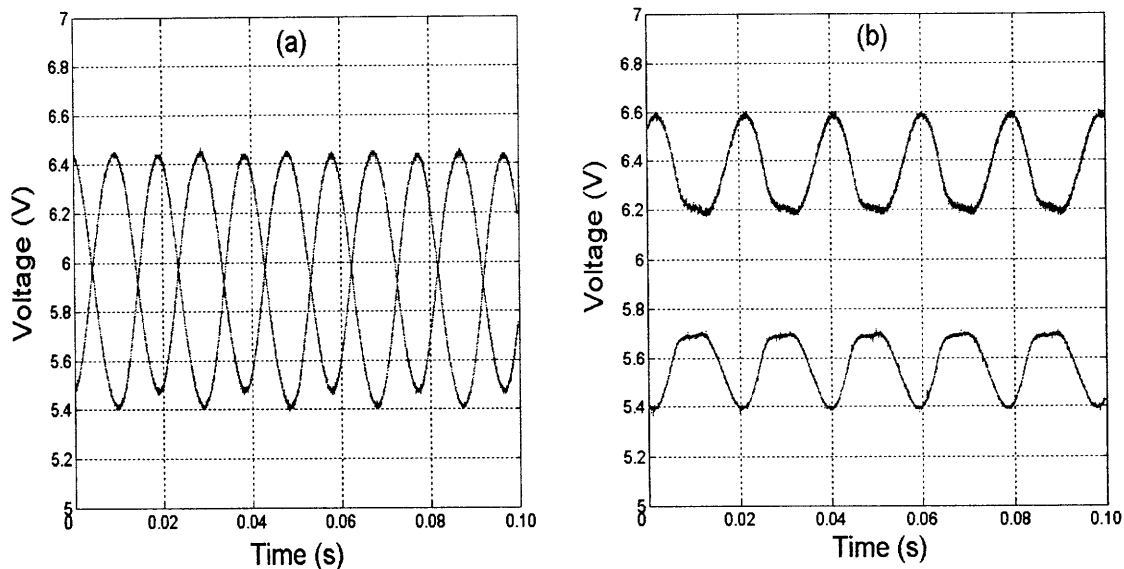


**Figure 2.37: Experimental output signal waveforms of the offset-compensated demodulator of figure 2.13, responding to sinusoidal input signals when (a) the offset-compensating mechanism is active, (b) the offset-compensating mechanism is not active.**

figure 2.19 in section 2.2.1. Our experimental peak gain is almost 32.7dB, not very close to our calculated and simulated values. The first reason is, let's recall from equation (2.15) in section 2.2.1 that the peak gain of the offset-compensated demodulator is almost  $A_{V1}$ .  $A_{V1}$  denotes the gain of the forward-path Gilbert multipliers in this block, which was calculated in equation (2.13). However, remember that this equation was itself derived from the more general Gilbert-multiplier gain equation of (2.5), with the assumption that the inputs are much smaller than the thermal voltage ( $V_{TH}$ ). If this is not practically the case, then the effective gain drops. Here in figure 2.38, since we used a test 100mV peak sinusoid signal as  $Sig_+$  ( $V_{sig}$ ), further investigation of equations (2.5) and (2.13) reveals

that the effective gain should be smaller by a factor of  $\frac{\left(\frac{V_{sig}}{2V_{TH}}\right)}{\tanh\left(\frac{V_{sig}}{2V_{TH}}\right)} \approx 2 \approx 6\text{dB}$ , in the

worst case. Accounting for this fact, our experimental gain is now just 2.2dB smaller than the theory. The second cause of the observed gain discrepancy might be the emitter resistance of the bipolar transistors that are practically employed in the Gilbert multiplier cells. We assumed this resistance to be zero everywhere in our calculation and simulation. However, even a few ohms of emitter resistance can result in a couple of dB loss in the demodulator gain.

Figure 2.38 also suggests that the  $-3\text{dB}$  pass-band of the offset-compensated demodulator is between 0.8-50Hz. As we previously showed in section 2.2.1, the upper bound is set by the absolute values of the on-chip output resistors and the off-chip output capacitors in the offset-compensated demodulator circuit (i.e.  $R$  and  $C_1$ , respectively in figure 2.13), not their relative value. The absolute values can have a few tens of percent of tolerance.

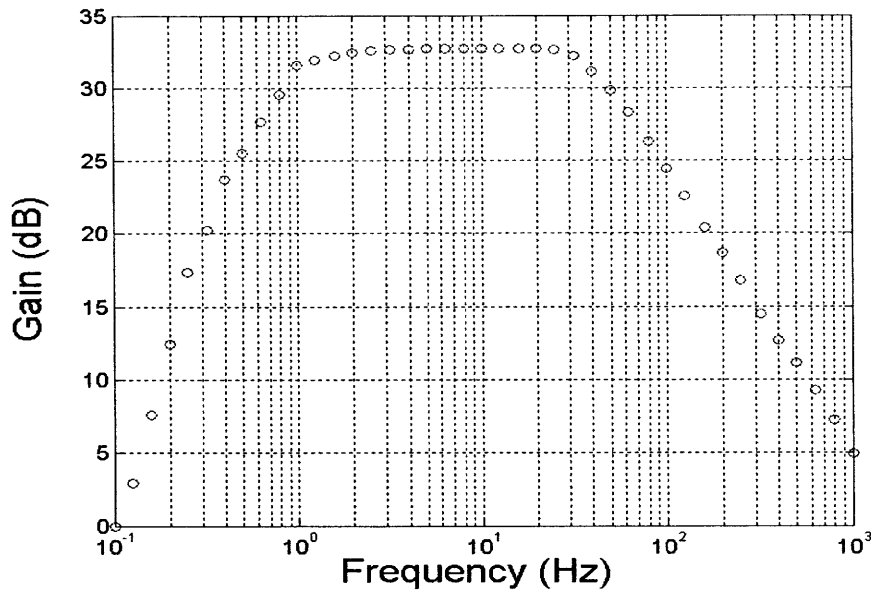


Figure 2.38: Experimental gain response of the offset-compensated demodulator (lock-in amplifier / offset compensator) block

This could be the explanation of our small upper bound value. However, it is easy to modify this bound to match the desired 100Hz simply by using a smaller value for the off-chip output capacitor pair.

## 2.6.2 VIBRATION SENSOR PARASITICS INSENSITIVITY

The next block to test is the front-end bandpass amplifier. Figure 2.39 shows the experimental gain response of this block. Naturally, it has the form of a bandpass filter with some gain, as we expected from our analysis and the simulated response of figure 2.26 in section 2.3.1. The experimental peak gain is almost 35.6dB, less than our calculated and simulated results. The reason is that unlike the demodulator gain, the gain of this amplifier depends on the output resistances of certain transistors. Generally, the transistor output resistance varies considerably in different IC fabrication runs and is not a reliable and exactly predictable quantity. It seems that this resistance is practically less than expectation in our fabrication, resulting in a lower open-loop gain for the bandpass amplifier. The second observed property of the response of figure 2.39 is its gain peaking. It means that the quality factor ( $Q$ ) is more than what we designed for. This peaking seems to be almost 3.5dB, which shows that the amplifier's feedback loop has still a good degree of stability. This increased  $Q$  might be, as we pointed out in section 2.3.1, due to the fact that  $C_2$  (in figure 2.22) is on the order of the parasitic capacitances of transistors  $T_6$ ,  $T_8$ ,  $T_9$ , and  $T_{15}$ . Thus, its actual value becomes larger that results in a higher value for  $T_2$  (the forward-path lowpass filter time constant of the amplifier). Looking back to equation (2.26) and considering that  $T_1$  is much larger than  $T_2$ , then  $Q \propto \sqrt{T_2}$ . Thus, a higher value for  $T_2$  results in a larger  $Q$ . However, we should keep in mind that since this front-end bandpass amplifier will be ultimately used in a closed-loop configuration, as long as the loop gain remains greater than one, we don't really care



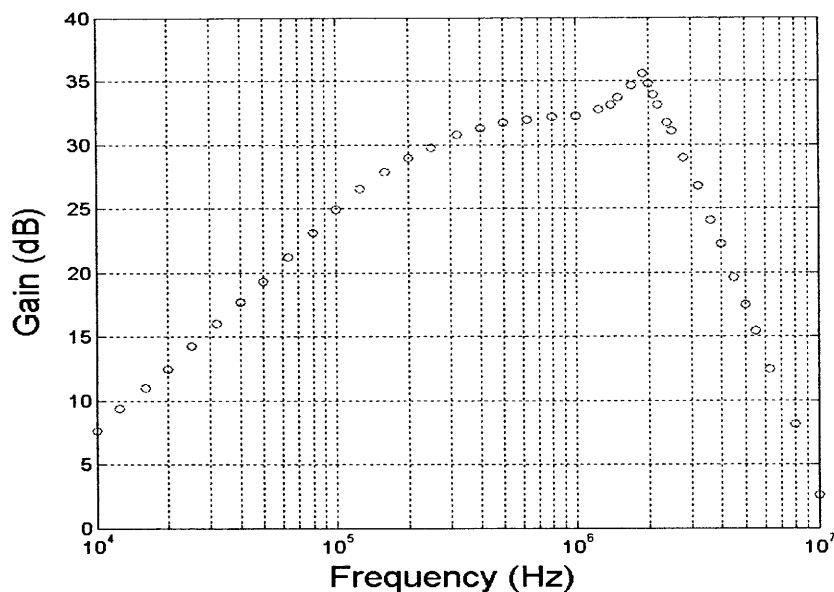


Figure 2.39: Experimental gain response of the front-end bandpass amplifier block

about the exact value of the open-loop gain or its quality factor.

Figure 2.39 also suggests that the  $-3\text{dB}$  pass-band of the amplifier is almost between  $200\text{kHz}$ - $2.8\text{MHz}$ . The higher upper bound value compared to simulation (figure 2.26) is due to the larger  $Q$  that we just discussed to have in the circuit. However, since this range still includes the carrier frequency neighborhood (i.e.  $500\text{kHz}$ ), the bandpass amplifier performance is fine.

Let's now use the front-end bandpass amplifier in a closed-loop configuration and experimentally examine the immunity of our vibration sensor against parasitics. Figure 2.40 shows the experimental output signal waveforms of the whole vibration sensor of figure 2.28, responding to sinusoidal input signals. In figure 2.40(a), there is no intentional parasitic capacitance between the sense node and substrate, but in figure 2.40(b) we have intentionally placed a parasitic capacitance of  $150\text{fF}$  between these two nodes (due to the specific pin configuration of our fabricated chip,  $150\text{fF}$  is the maximum value of an intentional parasitic capacitance we may arrange to place there). This value is in the same order of the typical parasitics that actually exist between the sense node and substrate. Like figure 2.31, to understand the parasitics insensitivity, we should compare the signals amplitude of figure 2.40(a) with figure 2.40(b). This reveals that the gain has only dropped by less than  $10\%$  in the presence of typical parasitics on the sense node.

After that, figure 2.41(a) shows the experimental gain response of the whole vibration sensor (meaning the gain from  $V_{in}$  to  $V_{+}-V_{-}$  in figure 2.29). It has the characteristics of a bandpass filter, as expected from equation (2.32) and the simulated response of figure 2.32(a). The peak gain appears to be  $35.8\text{dB}$ . Due to our chip pins limitations, the experimental configuration of figure 2.41(a) is not exactly the same as the simulated configuration of figure 2.32(a). If they were the same, the peak gain of figure 2.41(a)

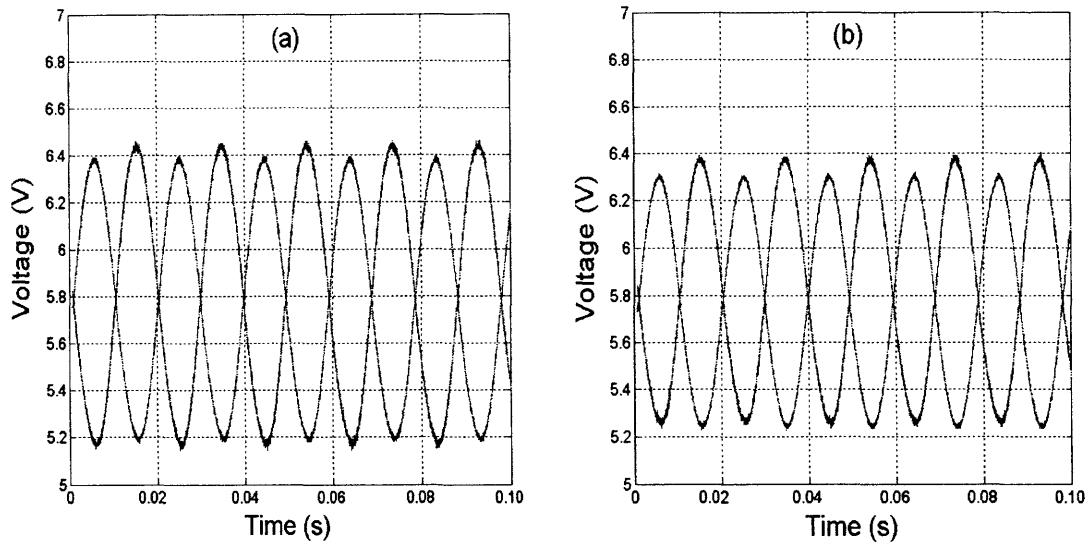


**Figure 2.40: Experimental output signal waveforms of the whole vibration sensor of figure 2.28, responding to sinusoidal input signals when (a) the intentional parasitic capacitance between the sense node and substrate is 0, (b) the intentional parasitic capacitance between the sense node and substrate is 150fF.**

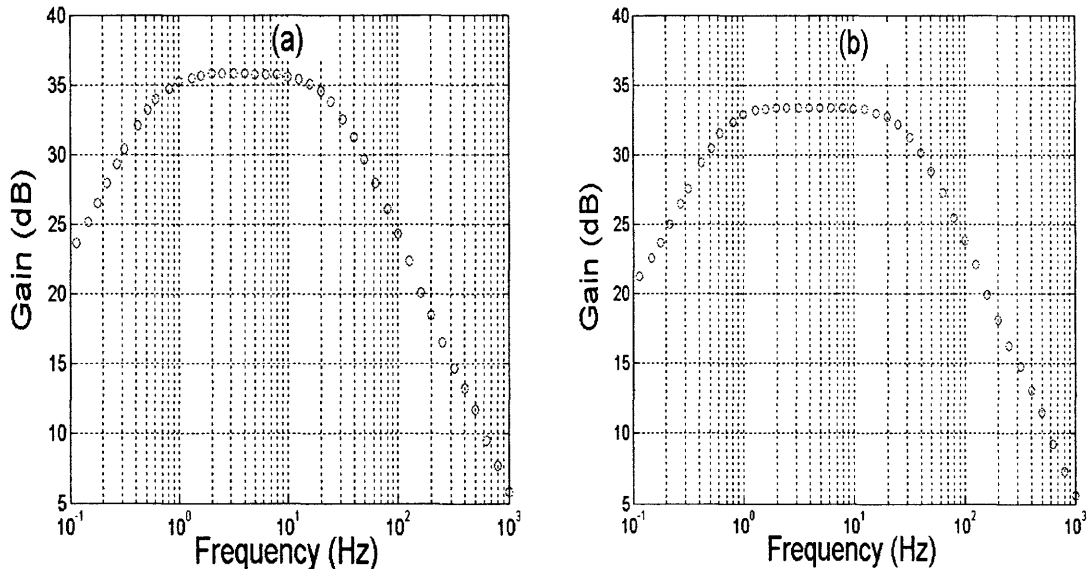


**Figure 2.41: (a) Experimental gain response of the whole vibration sensor of figure 2.28, (b) the same response with an intentional parasitic capacitance of 150fF between the sense node and substrate**

would be less than simulation mainly because of the less experimental gain of the demodulator block (refer to section 2.6.1). Note that the  $-3\text{dB}$  pass-band of the whole sensor seems to be between 0.5-30Hz, again due to the pass-band of our demodulator block (refer to figure 2.38) discussed in section 2.6.1. Note that as we said earlier, it is easy to make this pass-band coincide with the desired 1-100Hz range just by making minor modifications to the values of the off-chip capacitors.

Figure 2.41(b) shows the same response of figure 2.41(a), but with an intentional parasitic capacitance of 150fF placed between the sense node and substrate. We can observe that the general form of the response is similar, just the peak gain has dropped by almost 2.5dB. Consequently, this figure is a second confirmation of the parasitics insensitivity of our whole vibration sensor, which we previously illustrated in figure 2.40(b).

### 2.6.3 VIBRATION SENSOR TOTAL NOISE

Finally, it is time to experimentally evaluate the noise performance of our fabricated vibration sensor. Figure 2.42 shows the experimental noise spectral density of the whole vibration sensor, referred back to the sense node. In other words, this plot is basically the noise spectral density of the ultimate sensor's outputs (i.e.  $V_+-V_-$  in figure 2.28 or 2.29) measured by the "signal analyzer" instrument, divided by the gain from the sense node to these outputs (that, let's remember, is different from the gain shown in figure 2.41(a)). Further investigation shows that the experimental noise plot of figure 2.42 is close to the simulated noise plot of figure 2.33. We can clearly observe the cut-off effect of the output lowpass filter at frequencies around and above 100Hz. The large 60Hz component that is observed in figure 2.42 is due to the utility power line frequency and is not definitely originated from our vibration sensor.

Figure 2.43 shows the noise RMS value of the whole vibration sensor, again when referred back to the sense node. This plot is basically the square root of the integral of the noise spectral density of figure 2.42 (but with its vertical axis squared) from 0.1Hz to 100Hz of interest. The total noise RMS value appears to be almost 201nV. This value is a bit higher than the theoretical value and the simulated result (shown in figure 2.34). There are two reasons for the observed discrepancy. First, let's recall from equation (2.34) that the gain from the sense node ( $V_{sense}$ ) to the sensor's output ( $V_{out}$ ) is  $K(S) = \frac{C_T}{C_f} H(S)$

where  $H(S)$  represents the gain of the offset-compensated demodulator block,  $C_f$  is the feedback capacitance, and  $C_T$  is the total capacitances connected to the sense node (refer to figure 2.29), which includes the vibration sensing capacitors ( $2C_o$ ), feedback capacitor ( $C_f$ ), and any parasitic capacitance between the sense node and substrate ( $C_p$ ). We have designed the values for  $C_o$  and  $C_f$  and we have measured the gain of our demodulator, i.e.  $H(S)$  (figure 2.38). However, a reliable experiment to measure the actual value of the parasitic capacitance  $C_p$  on the chip is difficult to execute. Given a fixed measured value for the sensor total output noise RMS value (that is  $61 \mu V$ , not shown here), the worst case for the sense-node-referred noise RMS value is when we assume  $C_p$  to be zero that results in a minimum gain from the sense node to the output. This is how we quoted the result of figure 2.43. However, in practice because there certainly exists some parasitic capacitances from the sense node to substrate, the effective noise RMS value is less than figure 2.43. The second reason is, that our integration frequency range in both the noise calculation and simulation was 1-100Hz, whereas it is 0.1-100Hz here in figure 2.43. This increases the noise RMS value. In reality, we are not allowed to constrain our noise calculation integration range. The noise spectral density should be integrated up to infinite frequencies to yield a true and accurate noise RMS value. However, even

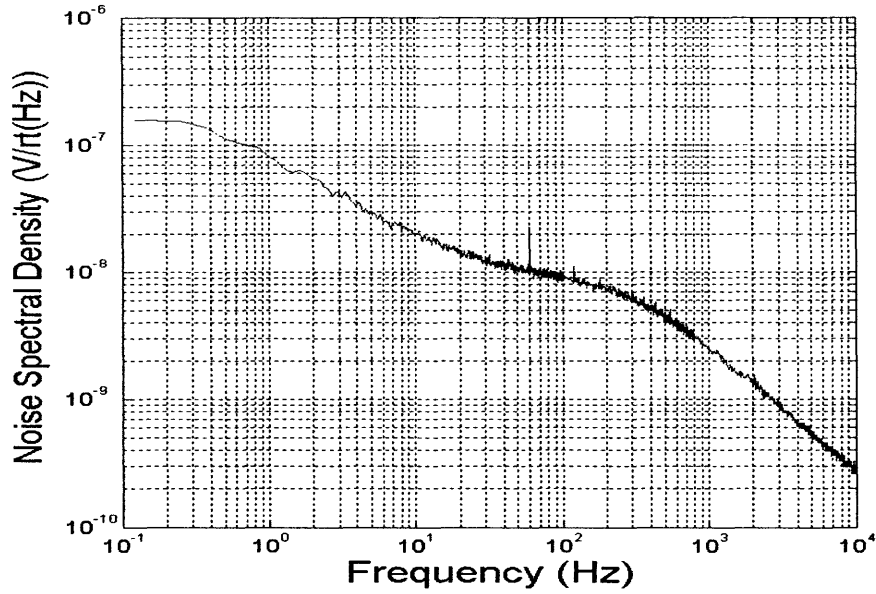


Figure 2.42: Experimental total noise spectral density of the whole vibration sensor, referred back to the sense node

performing such an infinite integration in our circuit turns out to increase the sensor noise RMS value of figure 2.43 by 54%, not orders of magnitude. The reason lies in our sensor design. Since we have placed a lowpass filter in the sensor's output to limit our vibration-sensing range to 100Hz, most of the higher-frequency noise is eliminated.

On the other hand, remember that the ultimate quantity of interest to us is the minimum detectable displacement ( $\Delta x_{\min}$ ) of our vibration sensor. From equation (2.39), we should obtain this quantity based on the experimental sense-node-referred noise RMS value ( $\widetilde{V}_{nsenseRMS}$ ) shown in figure 2.43. Fortunately, as we will demonstrate it shortly, the value of  $\Delta x_{\min}$  will turn out to be independent of our parasitic capacitance ( $C_p$ ) as long as we know the experimental sensor output noise RMS value. Thus, we will be able to reliably obtain the minimum detectable displacement.

Let's first repeat equation (2.39) here, for simplicity.

$$(2.39) \Rightarrow \Delta x_{\min} = x_o \left( \frac{C_T}{2C_o} \right) \left( \frac{\widetilde{V}_{nsenseRMS}}{V_o} \right) \quad (2.40)$$

$\widetilde{V}_{nsenseRMS}$  is equal to the sensor output noise RMS value  $\widetilde{V}_{n-outRMS}$  (that we measure) divided by the signal gain from the sense node to the output (that is  $K(S) = \frac{C_T}{C_f} H(S)$  from equation 2.34). Thus, we get:

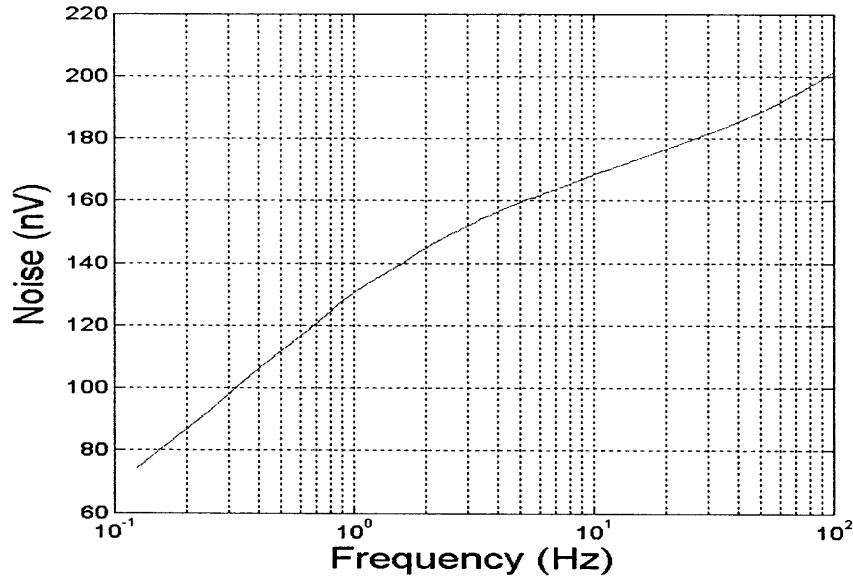


Figure 2.43: Experimental total noise RMS value of the whole vibration sensor, referred back to the sense node

$$(2.40) \Rightarrow \Delta x_{\min} = x_o \left( \frac{C_T}{2C_o} \right) \left( \frac{\widetilde{V_{n\text{senseRMS}}}}{V_o} \right) = \left( \frac{x_o}{V_o} \right) \left( \frac{C_T}{2C_o} \right) \left( \frac{\widetilde{V_{n\text{-ouRMS}}}}{K(S)} \right) = \left( \frac{x_o}{V_o} \right) \left( \frac{C_T}{2C_o} \right) \left( \frac{\widetilde{V_{n\text{-ouRMS}}}}{\frac{C_T}{C_f} H(S)} \right) =$$

$$\left( \frac{x_o}{V_o} \right) \left( \frac{C_f}{2C_o} \right) \left( \frac{\widetilde{V_{n\text{-ouRMS}}}}{H(S)} \right) \quad (2.41)$$

As equation (2.41) suggests, with a given  $\widetilde{V_{n\text{-ouRMS}}}$ , the minimum detectable displacement does not depend on the exact value of  $C_p$ . Considering the following experimentally measured values and settings for the parameters of equation (2.41), we can write:

$$\widetilde{V_{n\text{-ouRMS}}} = 61 \mu V_{rms}, \quad |H(S)| = 32.7 \text{ dB} = 43.2, \quad C_o = 150 \text{ fF}, \quad C_f = 50 \text{ fF}, \quad x_o = 1 \mu\text{m}, \quad V_o = 1 V_{rms}$$

$$(2.41) \Rightarrow \Delta x_{\min} = 2.35 \times 10^{-13} \text{ m} = 2.35 \times 10^{-3} \text{ \AA}$$

This value is close to the theoretical value obtained in section 2.4 and the simulated result of figure 2.35. It shows that we have succeeded in fabricating a vibration sensor that should sense  $2.35 \times 10^{-3}$  angstrom of displacement in its vibration-sensing range.

### 3. REFERENCES

- [1] O. Landolt, A. Mitros, and C. Koch, "Visual sensor with resolution enhancement by mechanical vibrations," December 2000.
- [2] C. Koch and R. Sarpeshkar, "Fusing vestibular and visual sensors on a chip," Proposal submitted to DARPA, August 1998.
- [3] R. Sarpeshkar, "Novel silicon photoreceptors," Proposal submitted to ONR's Young Investigator Program, October 2000.
- [4] Lecture Notes of "Biologically Inspired Electronics (6.973)," by professor Rahul Sarpeshkar, Massachusetts Institute of Technology, Fall 2000.
- [5] J. Bernstein, R. Miller, W. Kelley, and P. Ward, "Low-noise MEMS vibration sensor for geophysical applications," *Journal of Microelectromechanical Systems*, vol. 8, no. 4, pp. 433-438, December 1999.
- [6] T. Delbruck and C. A. Mead, "Analog VLSI phototransduction by continuous-time, adaptive, logarithmic photoreceptor circuits," Caltech Computation and Neural Systems Memo No. 30, February 14, 1995.
- [7] J. Kramer, R. Sarpeshkar, and C. Koch, "Pulse-based analog VLSI velocity sensors," *IEEE Transactions on Circuits and Systems-II*, vol. 44, no. 2, pp. 86-101, February 1997.
- [8] R. Sarpeshkar, J. Kramer, G. Indiveri, and C. Koch, "Analog VLSI architectures for motion processing: From fundamental limits to system applications," *Invited Paper, Proceedings of the IEEE*, vol. 84, no. 7, pp. 969-987, July 1996.
- [9] P. R. Gray and R. G. Meyer, *Analysis and Design of Analog Integrated Circuits*, 3<sup>rd</sup> ed. John Wiley & Sons, New York, 1993.
- [10] D. A. Johns and K. Martin, *Analog Integrated Circuit Design*, John Wiley & Sons, New York, 1997.
- [11] G. T. A. Kovacs, *Micromachined Transducers Sourcebook*, WCB/McGraw-Hill, New York, 1998.
- [12] Lecture Notes of "Capacitive position sense circuits," by professor Bernhard E. Boser, University of California at Berkeley, 1996.
- [13] B.E. Boser, "Capacitive electronic interfaces for integrated sensors," Transducers '97 short courses, 1997.

[14] B.E. Boser and R.T. Howe, "Surface micromachined accelerometers," *IEEE Journal of Solid-state Circuits*, vol. 31, no. 3, pp. 366-375, March 1996.